universität wien

MASTERARBEIT / MASTER'S THESIS

Titel der Masterarbeit / Title of the Master's Thesis

„Paleoseismoloy of the Seyring Fault in the Vienna Basin"

verfasst von / submitted by

Lisa Oppenauer, BSc

angestrebter akademischer Grad / in partial fulfilment of the requirements for the degree of

Master of Science (MSc)

Wien, 2022 / Vienna 2022

Studienkennzahl lt. Studienblatt / degree programme code as it appears on the student record sheet:	A 066 815
Studienrichtung lt. Studienblatt / degree programme as it appears on the student record sheet:	Masterstudium Erdwissenschaften UG 2002
Betreut von / Supervisor:	Dr. Kurt Decker

Contents

Acknowledgments

First and foremost, I want to thank my supervisor Kurt Decker for his continuous support and encouragement. His immense knowledge helped me throughout all the time of the field work, the research and writing of this thesis. Thanks for giving me the opportunity to undertake this study and your constant guidance.

Special thanks also goes to Michael Weissl for his immense help not only in the field, but also with the interpretation of the trenching results, geophysical measurements and the interpretation of periglacial processes.

Support was given by WienEnergie in the frame of the research project GeoTief EXPLORE 3D (WienEnergie order no. 610005270 as of 04.03.2019; project no. FA 536 035 of the University of Vienna) and is gratefully acknowledged.

My sincere thanks also goes to Adrián Flores-Oroszco and Matthias Steiner (Research Division Geophysics at the Department of Geodesy and Geoinformation of the Technical University of Vienna) for conducting and providing results of the geophysical measurements.

Special appreciation goes to Christopher Kollmann who helped me a lot at the trench site and for his advice on writing this thesis. Thanks for the continued support and for constantly encouraging me to push through and finish my studies.

Many thanks goes to my friends and colleagues Mario Theyer, Sophia Swaton, Andreas Hochwarter and Asma Nasir, for their time and help during fieldwork and data processing. Without their combined contribution working at the trench site would not have been half as fun.

Abstract

The Vienna Basin is characterized by moderate historical and instrumental seismicity. Quaternary basin subsidence and active faulting in the Austrian part of the Vienna Basin is indicated by geomorphological features like fault scarps and the offset of Quaternary terraces of the Danube. Studies show, that faults in the Vienna Basin can produce earthquakes with a maximum magnitude of M_{max}= 6.0-6.8 and geological data suggest slip rates of 1-2mm/yr for the main strike-slip fault system. Studies on normal faults that formed at releasing bends of the strike-slip system like the Aderklaa-Bockfließ Fault (ABF) and the Markgrafneusiedl Fault (MF) also show Quaternary activity with a maximum slip rate for the ABF of 0.05 mm/a for the last 200 kyr and for the MF 0.02 to 0.05 mm/a.

This study adds data from a splay fault of the Seyring Fault System (SFS) which is one of the normal faults compensating extension at releasing fault bends of the Vienna Basin Transfer Fault (VBTF). The SFS is an approximately SW-NE striking normal fault, delimiting the Gänserndorf Terrace in the west, from the Terrace west of Seyring. The Pleistocene Gänserndorf Terrace in the central Vienna Basin, formed by the fluvial plain of the Danube, is dissected into several parts by the Aderklaa-Bockfließ Fault and the Markgrafneusiedl Fault. The Terrace deposits represent glacial- and interglacial periods.

Seismic profiles, electrical resistivity tomography (ERT) data and borehole data were used to locate a segment of the SFS 3.4 km NNE of the city limits of Vienna. From the Borehole data, ERT and seismic profiles an offset in the Quaternary sediments of about 15 m could be observed. Further evidence for Quaternary deformation was derived from trenching of the Seyring Fault segment. Here, several normal faults at a depth of approximately 2 meters below the surface could be observed terminating at three event horizons and off-setting a succession of gravel, sand and loess. A clear Quaternary offset, the maximum slip rate and the magnitude of the earthquakes could be derived from the observations in the trench. Furthermore, the deformation history for six events and a time stratigraphic framework could be constructed with ^{14}C ages derived from gastropod samples. These six events observed in the trench took place in a time period between 31.96 kyr and 14.88 kyr cal BP producing several displacements of the sand and loess layers and three colluvial wedges with a maximum offset by a single event of about 0.4 m which is indicative of an earthquake with a magnitude of M=6.4. The smaller colluvial wedges and offsets are estimated to be produced by earthquakes with magnitudes between M=4 and M=5.5.

Zusammenfassung

Das Wiener Becken ist charakterisiert durch seine historische sowie instrumentelle moderat seismische Aktivität. Absenkung Quartärer Becken und aktive Störungen im österreichischen Teil des Wiener Beckens sind durch, unter anderem, geomorphologische Merkmale wie Geländestufen (Geländekanten) und den Versatz von Quartären Terrassen der Donau, bewiesen. Studien aus dem Wiener Becken zeigen außerdem, dass Störungen Erdbeben mit Magnituden bis zu M_{max}= 6,0-6,8 produzieren können. Geologische Daten deuten auf eine tektonische Absenkungsrate von 1-2 mm/a für die Haupt-Blattverschiebung hin. Des Weiteren zeigen Studien an Abschiebungen, welche sich am releasing bend des Blattverschiebungs-Systems bilden, wie der Aderklaa-Bockfließ Störung (ABF) und an der Markgrafneusiedl Störung (MF) quartäre Versätze von 0,05 mm/a innerhalb der letzten 200.000 Jahren an der ABF, und 0,02 bis 0,05 mm/Jahr an der MF.

Diese Studie liefert Daten von einer abzweigenden Störung, des Seyringer Störungs-Systems (SFS), welche eine der Störungen ist, die die Extension der Wiener Becken Transfer Störung (VBTF) kompensieren. Das SFS ist eine SW – NO streichende Störung, welche die Gänserndorfer Terrasse im Westen von der Terrasse westlich von Seyring abgrenzt. Die Pleistozäne Gänserndorfer Terrasse im zentralen Wiener Becken, welche durch die Flussebene der Donau geformt wurde, ist durch die Aderklaa-Bockfließ Störung und die Markgrafneusiedl Störung in mehrere Abschnitte geteilt. Die Terrassen-Sedimente repräsentieren die glazialen- und interglazialen Abschnitte.

Seismische Profile, Geoelektrik (ERT) Daten und Bohrloch Daten wurden zur Lokalisierung des Abschnitts des SFS, 3,4 km NNE der Stadtgrenze von Wien, eingesetzt. Aus den Bohrkernauswertungen, den ERT Daten und seismischen Profilen konnte ein Versatz der quartären Sedimente von ungefähr 15 m festgestellt werden. Des Weiteren konnte ein quartärer Versatz an dem SFS durch einen Schurf identifiziert werden. Es konnten mehrere Abschiebungen in einer Tiefe von ungefähr 2 m unter der Geländeoberkante identifiziert werden, welche an drei Event Horizonten enden und eine Abfolge von Kies, Sand und Löss versetzen. Ein eindeutiger quartärer Versatz, die maximale Absenkungsrate und die Magnitude der Erdbeben konnten von den Beobachtungen im Trench abgeleitet werden. Außerdem konnte die Deformations-Geschichte für sechs Events und ein Zeit-stratigraphischer Rahmen mithilfe von ^{14}C Altern aus Fragmenten von Schnecken Proben rekonstruiert werden. Diese sechs Events welche im Trench sichtbar waren, fanden in einer Zeitspanne zwischen 31,96 ta und 14,88 ta vor heute statt und produzierten mehrere Versätze in den Sand- und Lösslagen sowie drei Kolluvialkeile mit einem maximalen Versatz durch ein einzelnes Beben von 0,4 m welches durch ein Erdbeben der Magnitude M=6,4 entstanden ist. Die kleineren Kolluvialkeile und Versätze welche im Trench beobachtet wurden, können Erdbeben von einer Magnitude zwischen M=4 und M=5,5 produzieren.

1 Introduction

In the past decades, the Vienna Basin has been well studied by the ÖMV using subsurface seismic and borehole drillings for evaluations of gas and oil occurrences. Also, active tectonics has been studied thoroughly by using, in addition to the aforementioned methods, shallow geophysical sounding, geomorphological analyses and trenching surveys (Decker et al. 2005, Weissl et al. 2017, Hintersberger et al. 2018).

For active faults, evidence of Quaternary deformation can be obtained from trenching across fault segments to expose faults offsetting Pleistocene and Holocene sediments. Trenching, in addition, can reveal proofs of surface breaking paleoearthquakes such as colluvial wedges, faults terminating upwards in event horizons, liquefaction features, or soft sediment deformations (Pantosti and Yeats 1993, Michetti et al. 2005). Together with age data of the deformed sediments, the mentioned features constrain the timing of events, earthquake recurrence rates and the magnitude range of prehistoric earthquakes.

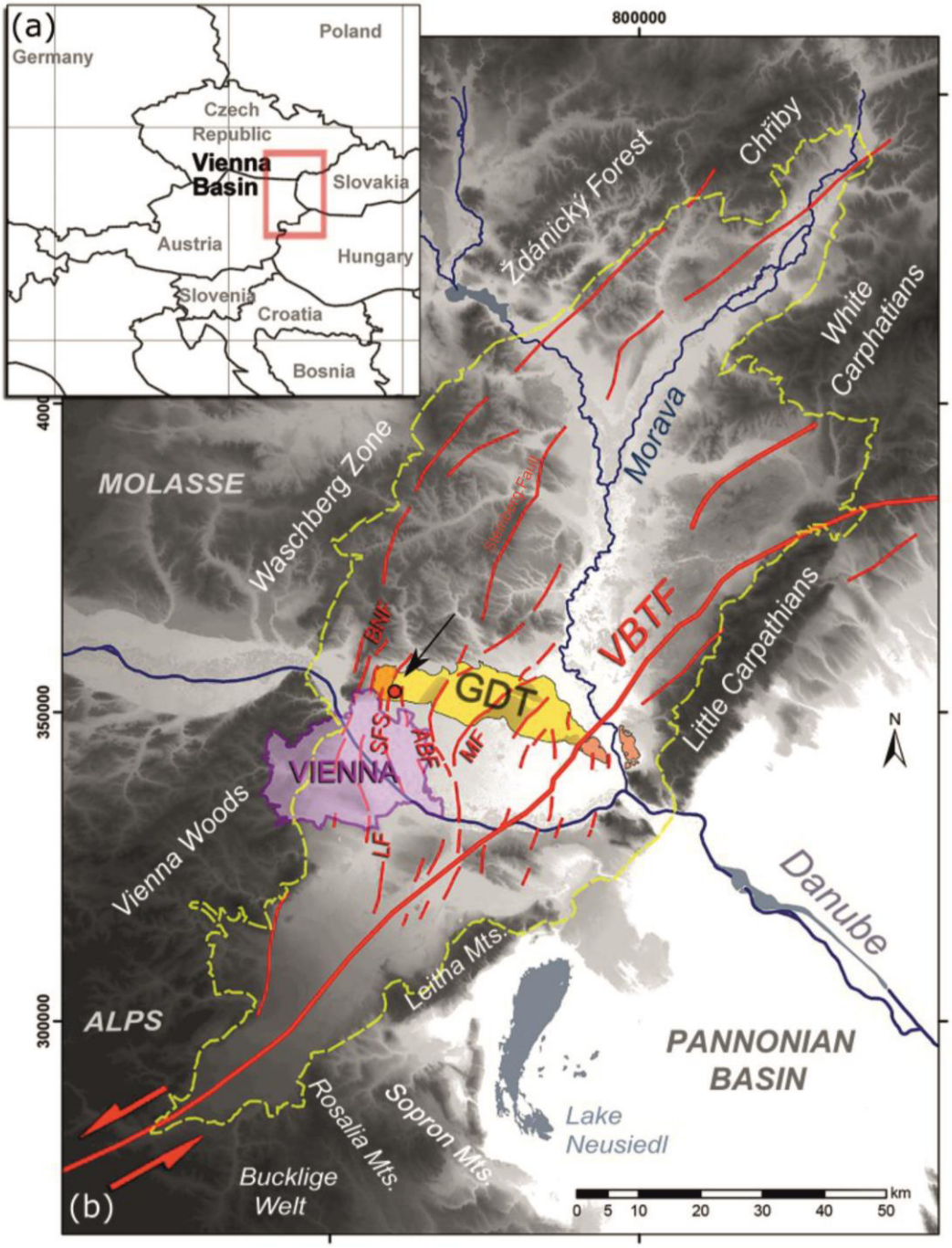

Fig. 1: a) insert of geographical overview of the Vienna Basin. b) Geographical and geological overview of the Vienna Basin (dashed yellow line) with Vienna Basin Transfer Fault (VBTF) (bold red line) and Gänserndorf Terrace (GDT). MF: Markgrafneusiedl Fault; ABF: Aderklaa-Bockfließ Fault; SFS: Seyring Fault System; BNF: Bisamberg-Nussdorf Fault; LF: Leopoldsdorf Fault and Steinberg Fault; black arrow indicating trenching location of SFS (GER01); after Weissl et al. 2017.

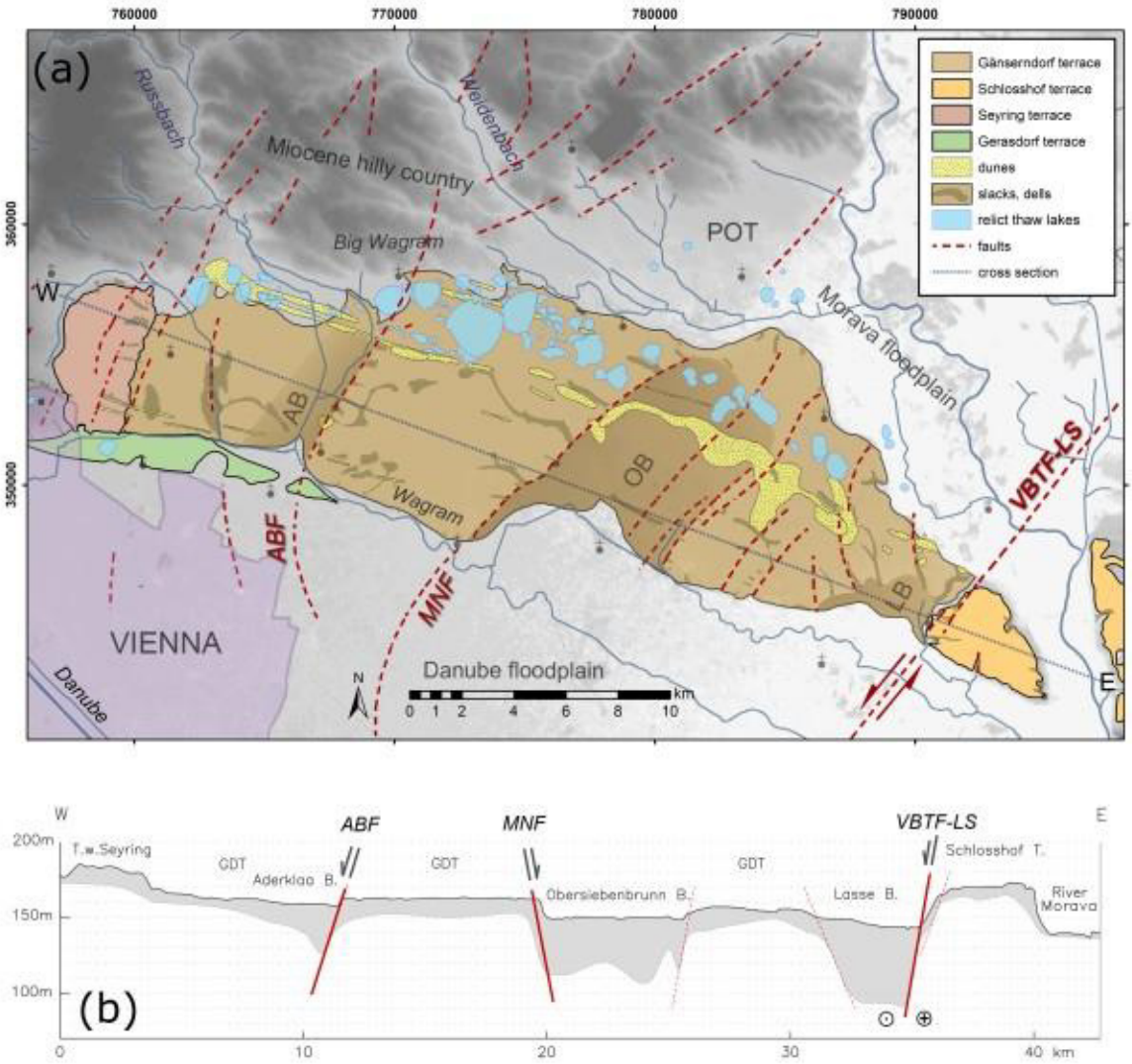

Fig. 2: (a) DEM of Gänserndorf Terrace (GDT) with SFS: Seyring Fault System; AB: Aderklaa-Bockfließ Fault; MNF: Markgrafneusiedl Fault; OB: Obersiebenbrunn Basin; LB: Lassee Basin; VTBTF: Vienna Basin Transfer Fault; (b) cross-section of the VBTF and thickness of Quaternary deposits with faults; after Weissl et al. 2017.

In this study, a part of the Seyring Fault System (SFS) is investigated 3.4 km NNE of the city limits of Vienna (coordinates of trench GER01: x-value approximately 759920 and y-value approximately 352530) (Fig. 3, Table A. 1). The Miocene tectonic processes of the SFS, as well as the influence of the glacial periods on the geomorphological development of the study area are presented. The Seyring Fault segment of this study was analyzed by geophysical measurements, borehole evaluations and trenching (GER01). Furthermore, a time stratigraphic framework for faulted sediments was developed using ^{14}C-dating from gastropod fragments on the lithological sequence.

The SFS belongs to a series of faults branching off from the Vienna Basin Transfer Fault (VBTF) which dissects the Gänserndorf Terrace (GDT) into several parts (Fig. 2). The Vienna Basin is a region of moderate seismicity indicated by historical and instrumental recordings observed along the VBTF. Examples include the 1906 Dobra Voda earthquake (M=5.7) and the ~ AD 350 Carnuntum (M=6) earthquake (Kandler 1989, Decker et al. 2006). The Marchfeld area and the branch faults of the VBTF seemed to be seismically inactive in historical times (Hintersberger et al. 2018). However, studies of the Markgrafneusiedl Fault (MF) and the Aderklaa-Bockfließ Fault (ABF), two faults dissecting the Marchfeld, revealed significant Quaternary vertical offsets. A maximum slip rate for the ABF is estimated with 0.05 mm/a for the last 200 kyr and for the MF 0.02 to 0.05 mm/a (Weissl et al. 2017, Hintersberger et al. 2018). Such faults can produce earthquakes with a magnitude of up to about M=7 (Hintersberger et al. 2018). Recurrence intervals of strong earthquakes were shown to be in the range of ten thousand years (Hintersberger et al., 2018).

The aim of this study is to locate the Seyring Fault and derive information of the Quaternary deposits and their deformation history. This is important to understand the regional seismic activity as historical and instrumental earthquake data is not complete or does not show earthquakes with low magnitudes, and does not cover times long enough to assess earthquakes wit recurrence intervals of thousands or ten thousands of years (Nasir et al. 2013). Considering the possibly high maximum magnitudes of potential future earthquakes, and the closeness of the area to the city of Vienna, those earthquakes can cause enormous hazards and the study of such faults is of economic and social importance.

2 Geographic Overview

The Seyring Fault System (SFS) is a NE – SW striking normal splay fault that branches off from the Vienna Basin Transfer Fault (VBTF) located in the northern Vienna Basin. The study area where the Seyring Fault segment is analyzed, is located approximately 2 km north of Gerasdorf (Lower Austria) and 3.4 km NNE of the city limits of Vienna (Fig. 3). The area of the trenching survey for this study lies within the Marchfeld area, more precisely on the southern margin of the Gänserndorf Terrace, an area which is heavily influenced by the last glacial periods and which belongs to the alluvial plain of the paleo Danube (Fink 1955) (Fig. 1).

The Neogene Vienna Basin in its rhomb -shape extends over 200 km at its maximum length and over 50 km in width. It is oriented NNE-SSW, situated between Gloggnitz in Lower Austria at its southwestern tip and Uherské Hradiště in the Czech Republic at its northeastern margin (Wessely 2006). The topographically western margin of the basin is formed by the hills of the Waschberg- and Flysch Units and the Northern Calcareous Alps. The eastern margin is shaped by the Little Carpathians, which are the westernmost part of the Western Carpathians, the Hainburg mountains and the Leithagebirge (Kröll et. al. 1993, Wessely 2006). The Austrian border separates the Vienna basin into a bigger Austrian part and a smaller Slovak and Czech part. The Danube on the other hand separates the Vienna basin in a northern and southern part (Wessely 2006).

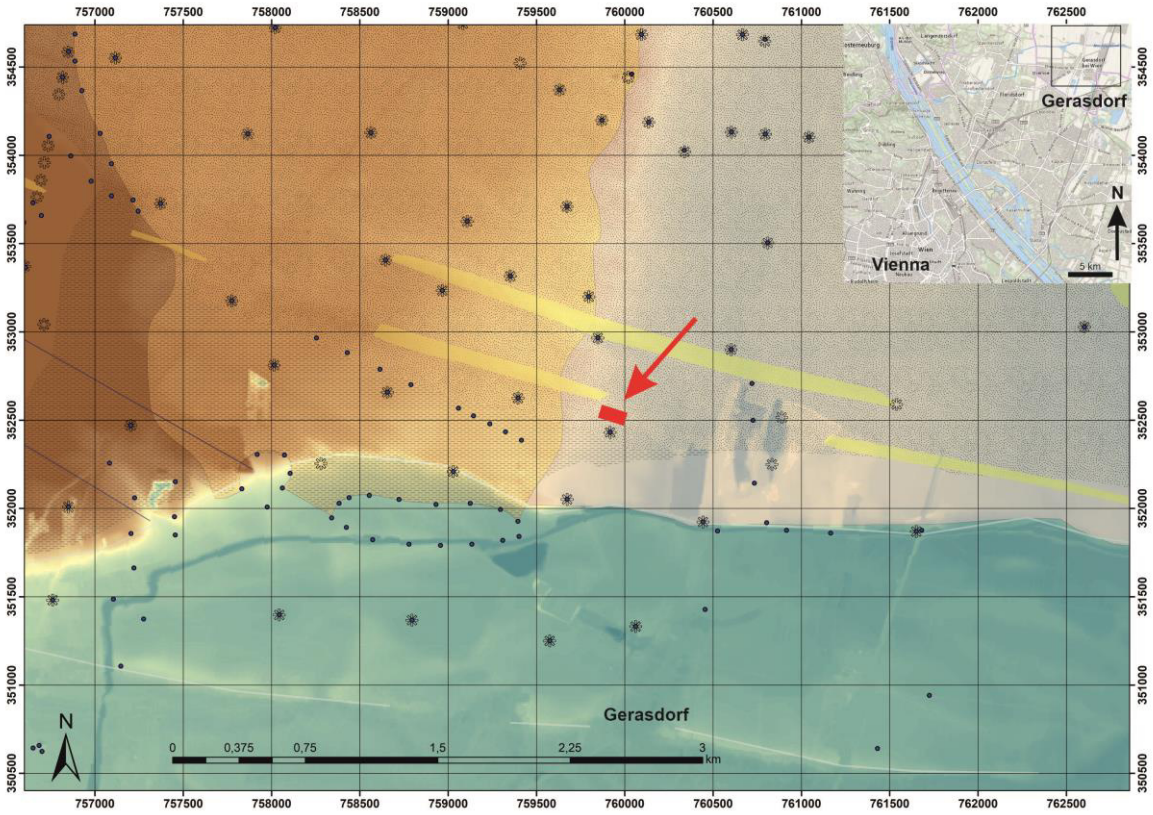

Fig. 3: Digital Terrain Model and geographic overview of trenching location. Red arrow indicating trenching location of the Seyring Fault segment. Blue circles indicating blast holes; black crossed circles indicating boreholes from the ÖMV drillings collected in the HADES database. Orange signature indicating Terrace West of Seyring (TWS); light pink signature indicating Gänserndorf Terrace (GDT); yellow signature indicating dunes on the TWS and the GDT.

3 Tectonic setting of the Vienna Basin Transfer Fault (VBTF)

3.1 Miocene tectonics and stratigraphy

The Vienna basin is mainly filled with Neogene to Quaternary fine-grained clastic sediments and gravel (Wessely 2006, Fink and Majdan 1954). The lower Miocene (Ottnangian-Karpatian, ca. 18-16 Ma) comprises of a piggyback basin succession with limnic-fluviatile and brackish sediments deposited in the central Vienna basin area. The succession starts with mostly fluviatile sandstone and mudstone of the Bockfließ-Formation (Hölzel et al. 2010). The Gänserndorf-Formation formed, locally with an unconformity, on top of the Bockfließ-Formation as lacustrine-terrestrial sediments (Harzhauser et al. 2020) followed by the 200 m thick sandstone-, pelite- and conglomerate-rich Aderklaa-Formation. These sediments can be as thick as 1500 m (Hölzel et al. 2010, Strauss et al. 2006).

At the Karpatian-Badenian boundary and the early Badenian, braided river deposits, consisting of conglomerates with medium to coarse gravel, formed the Rothneusiedl-Formation. The formation consists of polymict sediments with limestones, dolostones and crystalline components (Harzhauser et al. 2020).

On top lies the lower Badenian Mannsdorf-Formation which represents an open marine environment and partly upper bathyal conditions. The middle Badenian cycle starts with coarse siliciclastic sediments of the Auersthal-Formation, overlain by the sand of the Matzen-Formation and the pelites of the Baden-Formation, indicating open marine conditions in the Vienna Basin. In the upper Badenian, the 1000 m thick Rabensburg Formation ends the middle Miocene succession of shallow-marine deposits (Harzhauser et al. 2020).

In the Late (Upper) Miocene the “Beds of Leobersdorf” formed in the central Vienna basin. These are marginal deposits consisting of (marly) sand and gravel (Harzhauser et al. 2004).

The lower Pannonian sedimentary succession in the central Vienna Basin starts with 12-20 m thick sand and gravel and 20-50 m thick marl layers of the Hollabrunn-Mistelbach-Formation, which are deposits from a fluvial system that entered the Vienna Basin near Mistelbach (Harzhauser et al. 2003). Those deposits represent the Bzenec-Formation and are followed by 50-100 m thick marl and sand (“Schiefriger Mergel”).

In the Middle Pannonian the Inzersdorf Tegel followed, consisting of blue-green marls and clays. The Middle Pannonian Čáry Formation comprises of a series of lignits. It is overlain by the Upper Pannonian Gbely-Formation with 100 m thick units of terrestrial- fluviatile marl, clay and silt with sporadic freshwater limestone of the “Blaue Serie” and the “Gelbe Serie” (Grill 1968, Harzhauser et al. 2004). In the southern Vienna Basin, the Pannonian sedimentation terminates with the fluvial Rohrbach Conglomerate, a limestone and dolomite

gravel with sand and silt (Harzhauser et al. 2004). The thickness of the gravel deposits, which are unconformable underlain by miocene deposits, amounts to some 10 m (van Husen and Reitner 2011).

In the Marchfeld area, NE of Vienna, fluvial gravels formed Pleistocene terraces such as the Gänserndorf-Terrace (GDT). The gravel of the Gänserndorf Terrace are glacially overprinted, typically show cryoturbation and reach up to 10-15 m. The youngest gravels in the Danube valley of the Vienna Basin, which yield ages from the Young Pleistocene, formed the Prater Terrace. The Prater Terrace gravels are therefore not glacial overprinted (Grill 1968).

On top of the Pleistocene gravels of the Danube, silt and clay (2-3 m thickness) deposited followed by loess of a few tens of cm to m in thickness. According to Pecsi and Richter (1996) for a sediment to be defined as loess it must be a homogenous, porous, unstratified, weakly diagenized, calcareous sediment that is light yellow in color due to distribution of iron hydroxides. The grain size of a typical loess is between 0.0063 and 0.063 mm (silt) but consists mainly of coarse silt (0.02 -0.063 mm) (Haase et al. 2007, Smalley 1995). Wind-blown sands (“Flugsand”) from former river banks of the Danube formed dunes which especially shaped the morphology of the Marchfeld significantly (Grill, 1968). The dunes could reach up to 4 m of height and were dated to the Last Glacial Maximum (LGM; MIS 2) and the Late Würm to Early Holocene, respectively. During the Holocene, sand movement reactivated several times (Fink, 1955). Following the “Flugsand”, 0.5 – 1 m of recent soil (Tschernosem) were deposited (Fink and Majdan 1954).

The Vienna Basin Transfer system is an approximately 380 km long active sinistral strike-slip fault extending from the Mur-Mürz fault in the Eastern Alps to the Western Carpathians (Hinsch and Decker 2011, Decker et al. 2005, Beidinger and Decker 2010, Salcher et al. 2012). The fault system developed during the lateral extrusion of an Alpine-Carpathian crustal wedge in the Middle Miocene between two left-stepping segments of the sinistral transfer system. The fault system separates the eastern parts of the Alpine-Carpathian thrust unit into a stable block which overlies the European foreland from a NE-ward moving wedge which lies E of the fault (“Styria-West Carpathian wedge”) (Beidinger and Decker 2010, Decker and Peresson 2005, Royden, 1985).

The development of the Vienna Basin starts in the early Middle Miocene after the deposition of an Early Miocene piggy-back basin (wedge-top basin) on top of the Alpine-Carpathian fold-thrust belt (Decker and Peresson 1998, Hölzel et al. 2010, Peresson and Decker 1997). The Vienna Basin proceeded to develop into a pull-apart basin between the two sinistral NE-SW striking left-stepping transfer fault segments of the Mur-Mürz- and the Schrattenberg-Bulhary-Fault in the SW and NE of the pull-apart, respectively (Wessely 1993). Middle to late Miocene faulting formed a 150 km long and in maximum 40 km wide thin-skinned rhombic pull-apart basin (Royden 1985, Decker and Peresson 1998, Hölzel et al. 2010). The total Miocene to present fault offset is estimated with about 33 km (Linzer et al. 2002) indicating an average Miocene slip rate between 3.3 and 5 mm/a

(Decker et al. 2005). Rapid subsidence of the Vienna basin was caused by listric normal faults such as the Leopoldsdorf- and Steinberg-Faults that are linked to the overstepping sinistral strike-slip faults in the NE and SW of the basin.

In the late Miocene and Pliocene, extrusion of the Styria-West Carpathian wedge, sinistral faulting and pull-apart subsidence stopped due to the fundamental change of the regional stress field from N(NW)-S(SE)-directed to E-W-directed compression (Decker and Peresson 1997, Decker and Peresson 2005).

3.2 Active tectonics of the VBTF

3.2.1 Quaternary Basins

Quaternary faulting in the central Vienna Basin reactivating Miocene structures is shown by several Pleistocene basins overlying the Middle to Late Miocene pull-apart succession (Decker et al. 2005, Hinsch et al. 2005). Along the SE boundary fault of the southern Vienna Basin, the Mitterndorf Basin formed as a pull-apart basin due to the reactivation of the underlying Miocene negative flower structure of the strike-slip system. This Pleistocene pull apart basin shows alluvial gravel up to a thickness of 140 m. The fault zone which delimits the Mitterndorf Basin extends in the NE to another Pleistocene basin (Lassee Basin) with a thickness of up to 100 m of Quaternary alluvial gravel (Beidinger and Decker 2011). Negative flower structures underlie these Basins as shown in seismic data from the ÖMV Austria (Decker and Peresson 1998, Hinsch et al. 2005a, b).

From the Vienna Basin strike-slip system several N- to NNE-striking normal faults branch off. In the Marchfeld area, those faults tilted and dissected the Pleistocene river terraces and formed in the hanging wall Quaternary basins such as the Aderklaa- and Obersiebenbrunn Basins (Beidinger et al. 2011). Pleistocene coarse gravel and sand deposits in the Aderklaa Basin reach a maximum height of up to 35 m. In the southern part of the basin the river deposits of the paleo Danube reach heights up to 20 m whereas in the northern part only gravel from the Gänserndorf Terrace was deposited (Grill 1968). The Aderklaa and Obersiebenbrunn Basins underlie the Holocene flood-plain of the Danube and the Gänserndorf Terrace (Decker and Peresson 2005, Hinsch and Decker 2011, Wessely 1993, Chwatal et al. 2005).

3.2.2 Pleistocene terraces and their offset

The terraces in the Vienna Basin are formed by the alluvial plane of the Danube due to river incisions (van Husen et al. 2011a). Danube sediments were deposited in the Vienna Basin representing glacial- and interglacial periods (Fink 1955). North of the Danube three Pleistocene terrace units have been identified: The Gänserndorf Terrace (GDT), the Schlosshof Terrace (SHT) and the Terrace West of Seyring (TWS) (Weissl et al. 2017). The

terraces of interest in this study are the Gänserndorf Terrace and the Terrace West of Seyring.

The dissected Gänserndorf terrace is situated in the northern part of the Marchfeld which is located NE of Vienna and represents the “Hochterrasse”. It is situated between the Großer Wagram in the north, the Danube in the south, the Bisamberg in the west and the river March in the east. The Gänserndorf Terrace is delimited to the south by the Holocene flood plain of the Danube, in the west by the Terrace West of Seyring (TWS) in the east by the Lassee Basin (Beidinger et al. 2011). The GDT formed during the Riss glacial and is tectonically offset by Pleistocene normal faults at Aderklaa, Siebenbrunn (ABF) and Lassee (VBTF) (Decker et al. 2005, Fink and Majdan 1954). South of the terrace riser of the GDT, the Prater Terrace is located (late Würm). These terrace sediments are reworked in the early Holocene (van Husen et al. 2011a).

The highest and oldest Quaternary deposits can be found in the west of the Marchfeld in the Terrace West of Seyring (TWS) and in the Schlosshof – Terrace in the east of the Marchfeld. Based on their altitude above the Danube, these terraces were attribute to the Mindel glacial period (Fink and Majdan 1954). Dunes can be found on top of the Gänserndorf terrace as well as on the Prater Terrace (Fig. 3). These dunes consist of late Pleistocene to Holocene wind-blown sands (“Flugsand”) (Sebe et. al. 2015).

The Gänserndorf – Terrace consists of fluvial gravel and sand that is topped by aeolian loess or clay of the Würm glacial (Schnabel 2002). The gravel of the Gänserndorf Terrace is glacially overprinted and typically show cryoturbation. These permafrost features are typically visible down to depths of approximately 3 m under the top of the gravel and prove that, after the formation of the Gänserndorf Terrace, a typical interglacial Pleistocene soil formed and the top of the terrace was overprinted by periglacial processes in the next glacial period. Beneath lie undisturbed, coarse fluviatile and cross-bedded gravels. The total thickness of the fluvial deposits of the Gänserndorf Terrace reach up to 10 to 15 m (Grill 1968). The uppermost fluvial gravels of the northern part of the Gänserndorf Terrace are mostly overlain by colluvial or sometimes aeolian transported loess. In the central part of the terrace system, fluvial gravels are solely topped with so-called elder wind-blown sand. In the south, at the border of the Gänserndorf Terrace, to the Kleinen Wagram the top layer is covered with loess (Randlöss) (Fink 1955). The wind-blown sands in the Gänserndorf Terrace can reach a thickness of up to several meters (Fink and Majdan 1954). These wind-blown sediments can form morphological dunes, which were mapped NE of Vienna especially between Strasshof and Markhof (Grill 1968, Grill et al. 1954). The Loess succession on top of the GDT is dated to 17,3±1,9 kyr to 14,2±1,4 kyr by OSL (quartz) and IRSL (feldspar) dating (Weissl et al. 2017).

The Gänserndorf Terrace represents the middle Pleistocene “Hochterasse” in the Vienna basin north of the Danube and it is assumed to be formed in the MIS 6 (Riss glaciation) (van Husen et al. 2011). Isochron burial ages as well as pIRIR225 luminescence ages suggest a depositional age of the Gänserndorf Terrace ranging from 220±30 kyr to 260±30 kyr

(Braumann et al. 2019). A single, younger, age of 120±10 kyr comes from cryoturbated sand on the terrace top. These data corroborate older IRSL datings of the GDT ranging from 192±21 kyr to 255±29 (Weissl et al. 2017).

East of the line Gerasdorf-Seyring, the Gänserndorf Terrace is offset by Pleistocene normal faults of the Seyring Fault System that delimits the Quaternary Aderklaa Basin to the west. In the Aderklaa Basin the top of the GDT lies below the level of the Prater Terrace, locally causing onlaps of younger gravels of the Prater Terrace (Würmian) on the GDT (van Husen et al. 2011). Such onlaps are proved by cryoturbated terrace gravels of the Gänserndorf Terrace underlying Würmian gravels that are not cryoturbated (van Husen, pers. comm.). East of the line Deutsch Wagram-Helma-Bockfließ the top of the GDT is higher than the younger Prater Terrace again (Fink and Majdan 1954). This is due to NNE-SSW striking faults of the Aderklaa fault system (Fink 1955).

At the western margin of the middle segment of the GDT, the NW-dipping ABF forms a well-defined fault scarp with heights up to 5 m. At the eastern margin the middle terrace segment is offset by the SE-dipping Markgrafneusiedl fault which forms an up to 17 m high fault scarp and displaces the Middle Pleistocene gravels which can reach up to 15 m in thickness (Fig. 2b). The displacement of Middle Pleistocene gravels due to normal faulting is verified by gravels from the Late Pleistocene (Würm) terrace locally overlying the Middle Pleistocene deposits (Grill 1968, Weissl et al. 2017).

West of the GDT the Terrace West of Seyring as the next higher terrace unit is located. The Quaternary basis of the TWS lies around 167 m and is therefore lower than the basis of the Arsenal Terrace. This leads to a Quaternary thickness of about 8 to 10 m. The gravels of the TWS are underlain by Middle Pannonian sand and Middle Pannonian clay marl and sands in the NW and N, respectively (Grill 1968).

3.2.3 Seismicity and paleoseismological overview

Quaternary basin subsidence and active faulting in the Austrian part of the Vienna Basin is indicated among other things by geomorphological features like offset of Quaternary terraces of the Danube and moderate seismicity, which can produce earthquakes with a maximum magnitude of M_{max}= 6.0-6.8 (Decker and Hinsch 2005, Hinsch and Decker 2011).

Most earthquakes in Lower Austria occur in the Vienna Basin, with earthquakes of moderate seismicity produced by the Vienna Basin transform system (Decker et al. 2005). In the 20th century more than 360 earthquakes could be recorded in this area. Historic records show numerous earthquakes in lower Austria which were documented since the year 1000 (Hammerl and Lenhardt 2013). Recorded earthquakes in the Eastern Alps, West Carpathians, Hungary and Austria from 1600 to 2004 are documented in the ACORN catalogue (ACORN 2004). The historical documentation, however, is limited by witnesses of earthquakes, the intensity of the earthquake and therefore their observability. This leads

to an incomplete documentation of historic earthquakes (Nasir et al. 2013). Also, the accuracy of especially the earlier reports, are sometimes questionable and imprecise.

The earliest reported earthquake in the Vienna Basin occurred in 1283 in Wiener Neustadt (Hammerl and Lenhardt 2013). In 1768 another earthquake occurred in Wiener Neustadt which is well documented. Numerous sources describe damages on houses, collapsed chimneys, etc. as a result of the earthquake in Wiener Neustadt. In Vienna, which lies 45 km north of Wiener Neustadt, reports of collapsed chimneys were also documented (Nagel 1768).

At the beginning of the 20th century seismographs were installed in Europe to document seismic activity (Hammerl and Lenhardt 2013). Therefore, in 1906 the Dobrá Voda earthquake at the northern part of the Vienna Basin Transfer Fault in Slovakia could be recorded with an intensity I_0=9 - 8, respectively (Nasir et al. 2020).

If no written documentation of earthquakes is available, historic earthquakes can also be observed by excavations of ancient settlements that show typical damage of seismic events. In the fourth century A.D. an earthquake in Carnuntum, which is situated 40 km east of Vienna, with an intensity I_0=9 damaged masonry structures throughout the roman settlement. This earthquake was most likely triggered by the Lassee-segment of the Vienna Basin strike-slip fault system (Kandler 1989, Decker et al. 2006, Hintersberger 2019).

Although the Vienna Basin Transfer Fault (VTBF) shows moderate historical seismicity, the area of the Gänserndorf Terrace and surroundings show no historical or instrumentally documented earthquake records (Hintersberger et. al. 2018).

If there is no evidence of Pleistocene faulting in written or instrumental records, or if there is no clear geomorphological evidence at the surface, trenching along a fault segment can bring evidence of surface-breaking earthquakes (Pantosti et al. 1993). However, trench investigations along a fault segment may not always show all faulting events which occurred. In the investigated area of the Marchfeld, the Markgrafneusiedl Fault (MF) as well as the Aderklaa-Bockfließ Fault (ABF) seemed to be inactive faults as inferred from historical and instrumental earthquake records. However, three trenches across the MF fault showed evidence of five to six surface-breaking earthquakes and quasi-periodic or clustered Quaternary faulting during the last 120 kyr. The magnitude of the earthquakes is estimated to range between 6.2 +/- 0.5 and 6.8 +/- 0.4 (Hintersberger et. al. 2018). Trenching at the ABF did not reveal a fault plane due to cryoturbation, however, ERT measurements indicate an offset in the Quaternary deposits of about 10 m (Weissl et al. 2017).

4 Methods and Materials

4.1 Borehole evaluation

Between 1954 and 1989 the ÖMV drilled large numbers of boreholes to evaluate gas and oil occurrences in varying depths in the Vienna Basin. This data includes numerous, about 10 m deep, blastholes for reflection seismic as well as few hundred-meter-deep boreholes to investigate the structure of Pannonian sediments (so-called CF-drillings). The data derived from ÖMV drillings were collected in the HADES database of Lower Austria and was a foundation for this study. Also, there are several borehole datasets from 2018 available in this area from the company Kovanda GmbH resident in Gerasdorf. Therefore, thirty-nine borehole data provided by OMV AG and from Kovanda GmbH, operated by Geobohr GmbH were used to investigate the lithological sequence and the base of Quaternary gravel in the area of interest near Gerasdorf, especially along the Salzstraße (Fig. 4).

Fig. 4: Location of cross-sections G1 to G4 (black lines); trenching location in yellow; blue circles indicating blast holes; black crossed circles indicating boreholes from the ÖMV drillings collected in the HADES database and violet crossed circles indicating boreholes from KOVANDA GmbH.

The ÖMV boreholes in the HADES database are up to 200 m deep and show a sequence of top soil in the first tens of centimeters followed by a few meters to ten meters of Quaternary silt and loess, fine to coarse grained sand and fine to middle grained gravel of the Gänserndorf Terrace on top of a succession of silt, clay-marlstone and clay with intermediate sand and gravel from the upper Miocene (Fig. 5). The latter are attributed to the “Pontian” stage in the drilling reports.

The blast holes from 1964 and 1969 are up to 22 meters deep and show approximately 1 m of top soil followed by up to 13 m of gravel and sand, over four to eight meters of marl (blauer and bunter Mergel) (Fig. 16). However, the accuracy and reliability of these datasets are questionable due to the inaccurate lithological records in depth and lithological content.

The boreholes provided by Kovanda GmbH on the other side are very reliable in terms of documentation and the recording of the lithological sequence. The boreholes are five and 16 meters deep. In the first ten centimeters they show top soil followed by sand and gravel of 12 meters over grey to brown sandy silt (Fig. 5).

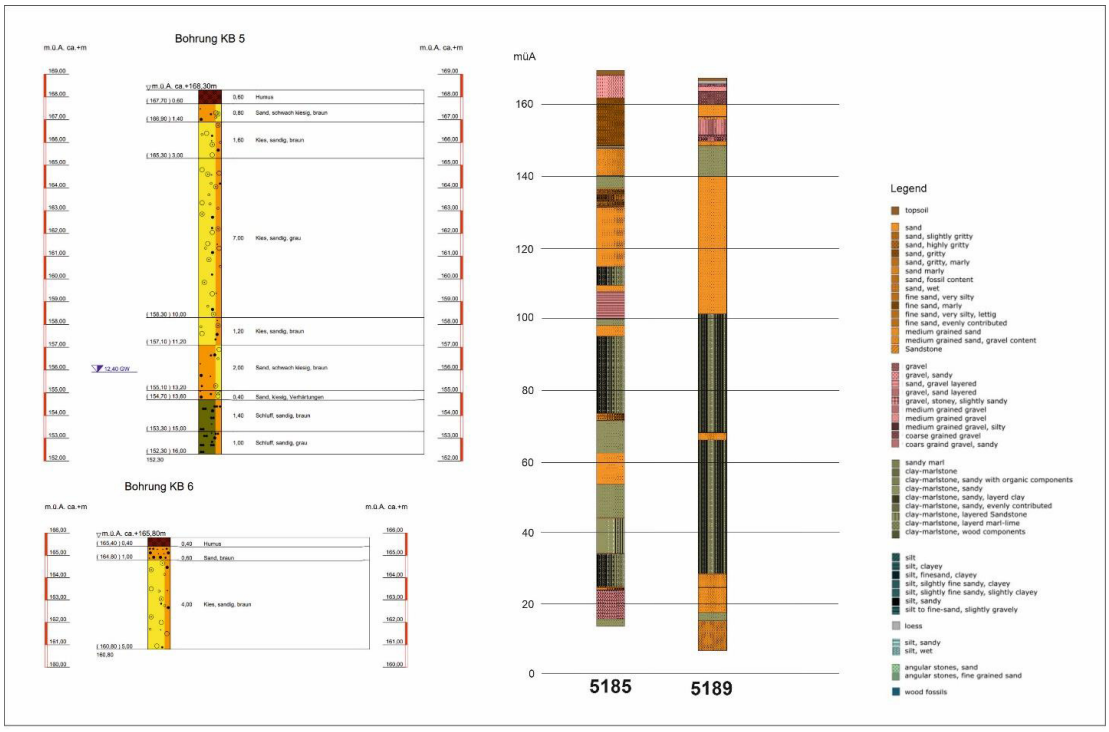

Fig. 5: Boreholes next to trenching location; KB 5, KB 6, 5185 and 5189.

Four profiles were constructed (G1 to G4). One cross-section (G1) is exactly along the Salzstraße, striking east – west (Fig. 13, Fig. 14, Fig. 15, Fig. 16). G1 was constructed from nine boreholes data and from seismic and ERT data and has a length of 3400m. The other cross sections are located north and south of cross section G1. Cross sections G2 and G3 have a length of 2400m. In cross section G4 the borehole data form OMV AG were evaluated over a length of 3000m (Fig. 16).

4.2 Geophysical methods

4.2.1 Electrical resistivity tomography (ERT) and reflection seismic

Electrical resistivity tomography measurements are obtained by injecting a current through electrodes into the ground. The resulting difference in voltage at two potential electrodes is then measured and an apparent resistivity value can be calculated. In order to get the true subsurface resistivity, the measured apparent resistivity values are inverted. Most common arrays for 2-D imaging are the Wenner, dipole-dipole, Wenner-Schlumberger, pole-pole and pole dipole methods. The measured value is then plotted on a log-log graph and can be interpreted. The resistivity value is different for different types of soil materials and rocks. Sedimentary rocks normally have a lower resistivity value then igneous and metamorphic rocks. This is due to their more porous properties and usually they have a higher water content. Also, clayey soil has lower resistivity values than sandy soil. (Loke 1999, Everett 2013, chapter 4).

To obtain a seismic 2D profile of the near surface structures, seismic waves are induced into the earth. The seismic waves are reflected at the boundary where rock properties change. Depending on the strata the waves reflect back at different velocities to the geophones (receiver). The geophones collect these data and out of the travel time data, seismic velocities and layer depths can be calculated (Everett 2013, chapter 6, McCalpin 2009, chapter 2A.3).

4.2.2 ERT measurements and 2D seismic north of Gerasdorf

To locate the fault in question more precisely in the area of Gerasdorf, north of Vienna, in July 2020, five electrical resistivity tomography (ERT) measurements were processed. Four high-resolution profiles with a length of 200 m and an electrode spacing of 3 m (GDP 101, GDP 102, GDP 103, GDP 105) and a regional profile with a length of 2.17 km were measured along the Salzstraße north of Gerasdorf, overlapping the four shorter profile segments, in east west direction (Fig. 6, Fig. 17, Fig. 18). The electrode spacing was set to 3 m and each segment had 72 electrodes. These measurements were operated and processed by the Research Division Geophysics at the Department of Geodesy and Geoinformation of the Technical University of Vienna (Associate Prof. Dr. Adrián Flores-Orozco).

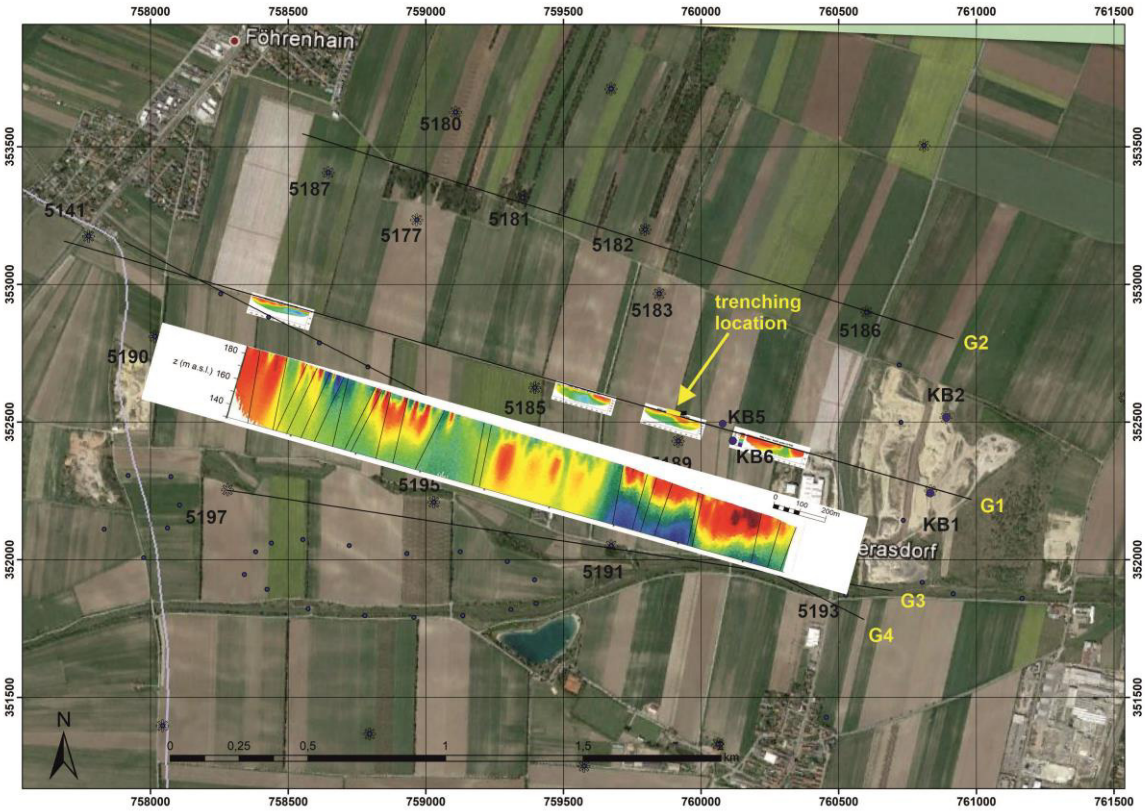

Fig. 6: Location of electrical resistivity tomography (ERT) measurements; four short ERT measurements (GDP 101, GDP 102, GDP 103, GDP 105); one ERT measurement along the Salzstraße with 2.17 km. Location of the reflection seismic and trenching location (yellow arrow).

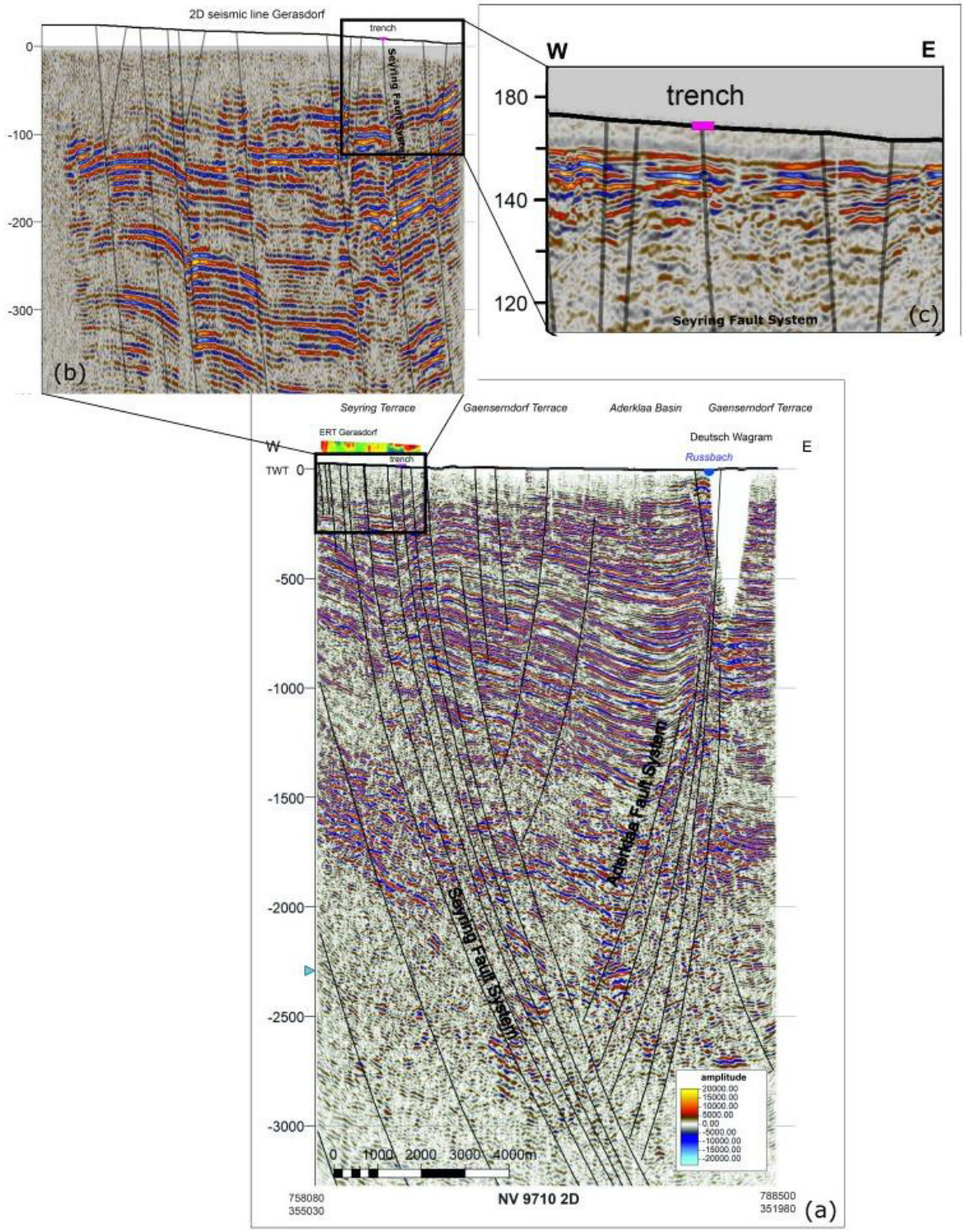

Fig. 7: a) and b) seismic profile of faults dissecting the Gänserndorf Terrace with interpreted Seyring Fault System and Aderklaa Fault System. c) inset of location of interest with interpreted faults of the Seyring Fault System and trenching location (pink).

In December 2020, the company Afry was assigned to operate and process a seismic reflection and refraction measurement along the Salzstraße in Gerasdorf to obtain a 2.4 km long 2D seismic profile in E-W direction. (Fig. 8) The measurements were processed with closely spaced shots of 5 m between each shot and seismic recorder with 5 m space between the 10 Hz geophones (Afry 2020). The shot density was increased to 2.5 m spacing in parts of the profile where ERT measurements indicated faults.

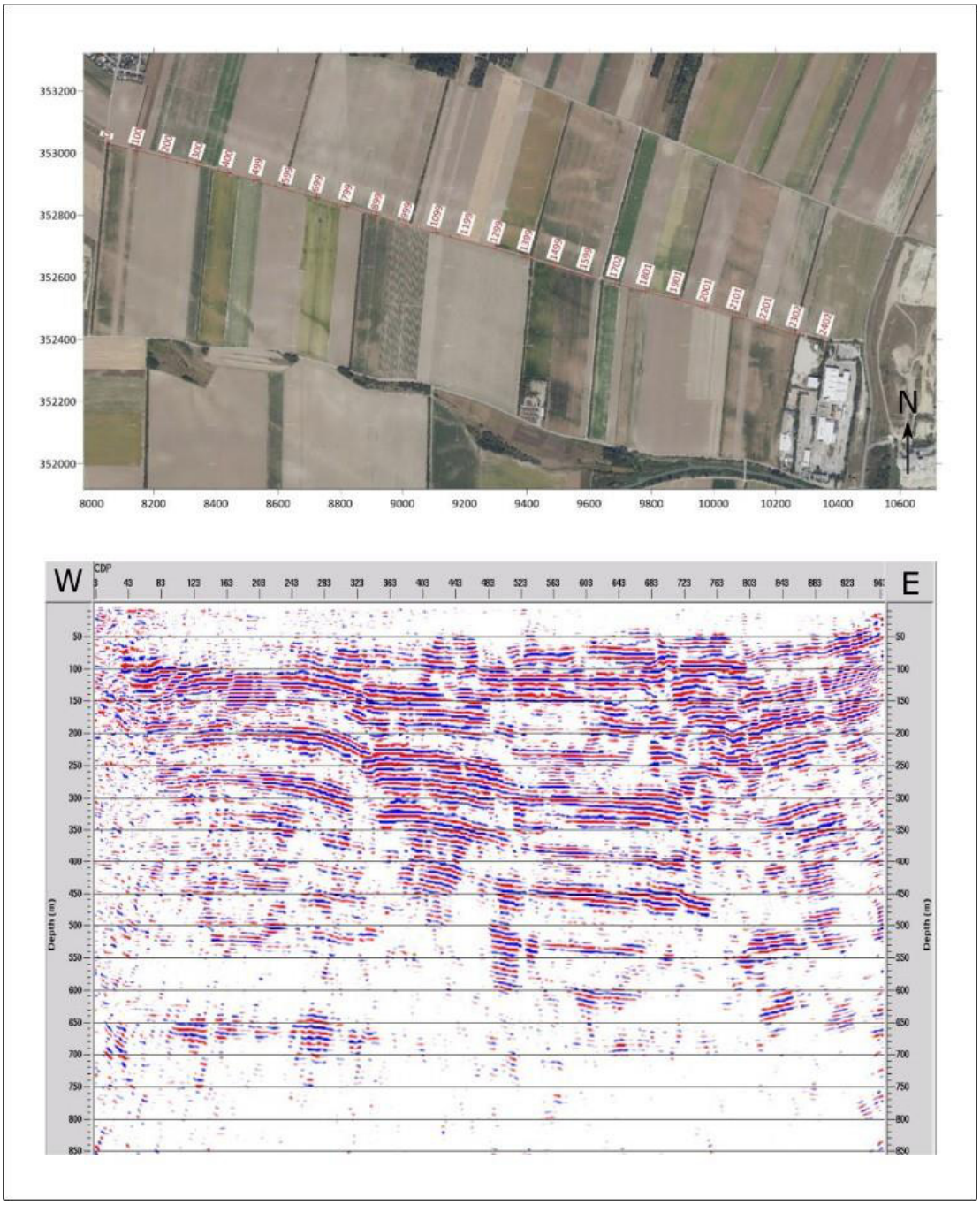

Fig. 8: seismic reflection profile and profile location from Afry 2020.

4.3 Paleoseismological trenching of the Seyring Fault

Paleoearthquakes create seismological evidence which can not only be observed on the ground surface, such as fault scarps, but also in trenches. Evidence for paleoearthquakes observed in trenches can be wedge – shaped, scarp – derived colluvial deposits that overly the pre-faulting surface (McCalpin 2009). Therefore, the colluvial wedge postdates an event and the sediments which it overlies predates the earthquake event and are consequently event horizons. Another event horizon can be a base of an unfaulted sediment layer capping a fault, indicating the undisturbed layer is postdating the event (Pantosti et al. 1993).

The stratigraphic sequences of both trench sides were documented, mapped and the color attributes of the sediments, according to Munsells Soil Book of Color, were determined. The color attributes are Hue, Value and Chroma. Hue is the color, such as Red (R), Yellow (Y), Green (G) etc., Value is how light or dark the color is and is indicated with a number, for example 2 or 6, where 2 is darker than 6. Chroma is how weak or strong the color is, this is typically a number between 2 and 14 (two is weaker than 14). These attributes lead to a three-dimensional Color code. For example, the color code 2.5Y 4/3 means that 2.5Y is the Hue (color), 4 is the Value (lightness or darkness) and 3 is the Chroma (weak/strong). Furthermore, orientation measurements of pebbles from gravel layers were conducted. The faults on both sides of the trench walls were mapped and the orientation of two faults (F1, F2) were measured, documented and later plotted, as well as the pebble orientations, with tectonics FP. The magnitude and the annual displacement rate were derived from the tectonic features observed in the trench, as each earthquake creates characteristic features which are related to the order of magnitude of the earthquake (Michetti et al. 2005).

Both trench walls were logged in a scale of 1:20 to create a detailed cross-section. Pictures of each square as well as drone images were taken to create a photomosaic in Agisoft Metashape (Version 1.5.2) and ArcGIS (Version 10.7.1). Out of this photomosaic a digital version of the northern and southern wall was constructed in Corel Draw and Corel Photo-Paint (Version 21.0.0.593).

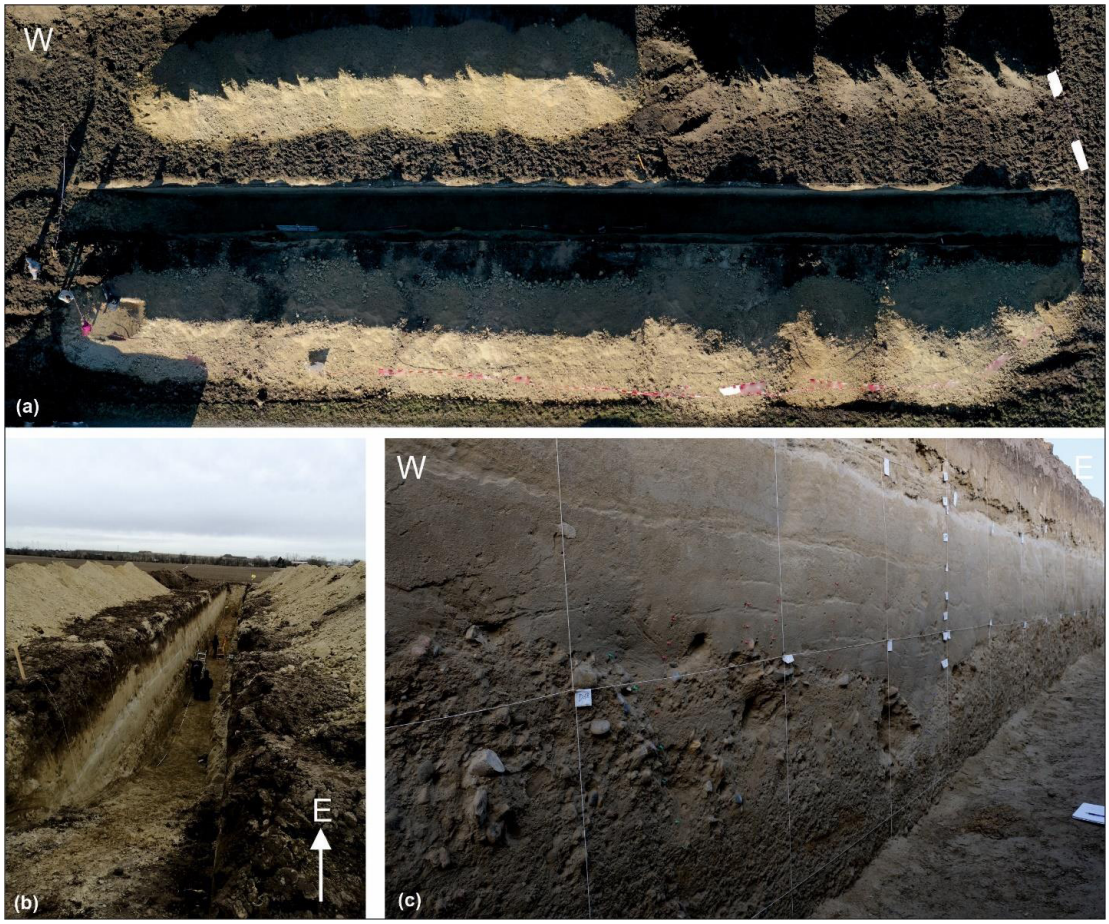

Fig. 9: a) trench site from above (drone image); b) and c) trench site and 1x1 m grid for scale.

4.4 Sampling and sample preparation

Two gravel samples were taken five meters from the west end of the trench (D5) and 1 meter from the middle part of the trench (D17). The grain shape and petrography of these samples was determined and a grain size distribution curve was plotted. Furthermore, seven loess and sand samples were collected from the northern and southern wall of the trench (Fig. 10) for geochronological age dating using the radiocarbon (^{14}C) method.

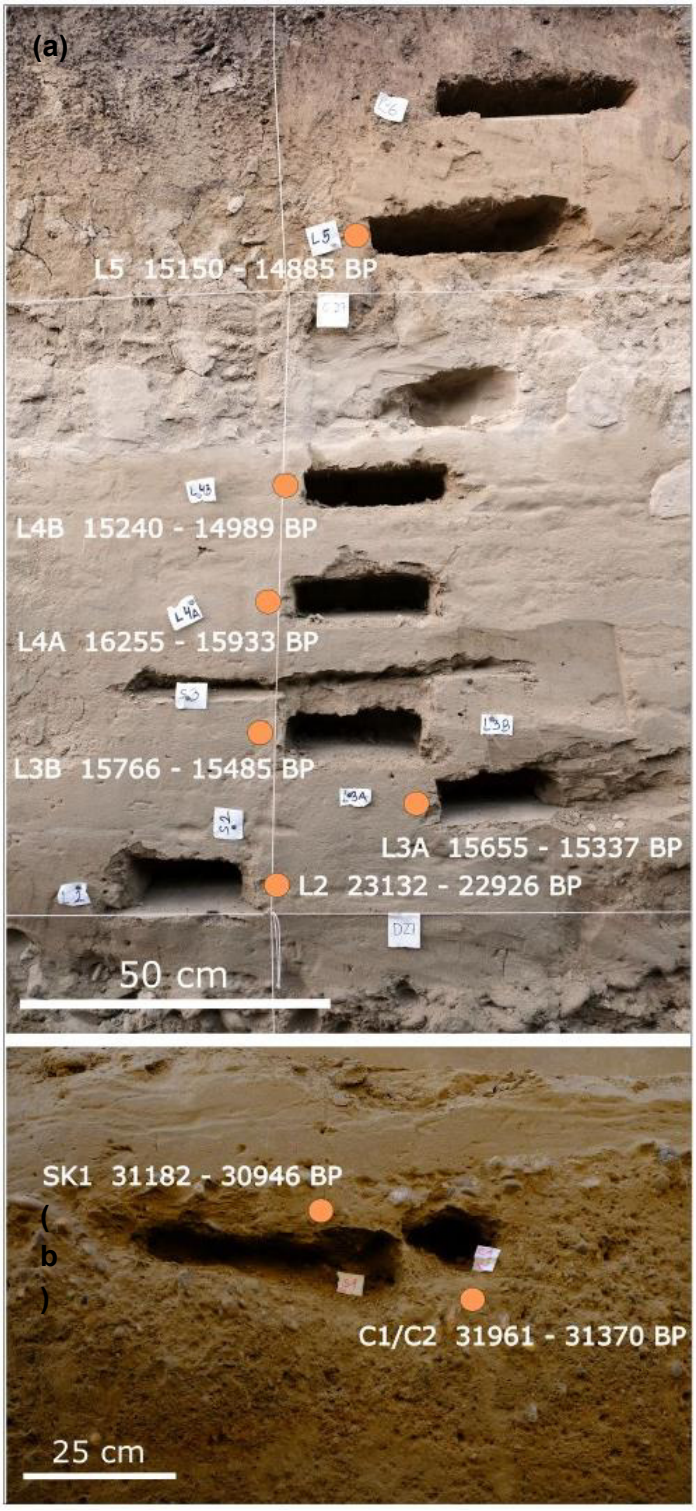

Fig. 10: gastropod sample locations (orange circles) for geochronological age dating and derived calibrated ages from gastropod samples; (a) northern wall with gastropod samples L2 to L5; (b) southern wall with mixed gastropod sample of C1 and C2 and gastropod sample SK1.

This samples were first sieved trough a 0.5 mm sieve. Afterwards loess gastropods and cement samples were picked under the microscope from all of these samples (Fig. 11 and Fig. 12). Ten gastropod samples (L1, L2, L3A, L3B, L4A, L4B, L5, S1/1N, S1/2S, C1C2) and one cement sample (S1CR) were then examined by Beta Analytic Inc. on their δ 13C value and on their O18/O16 ratio.

Eight samples (L1, L2, L3, S3, L4, S4, L5 and L5) from the north wall of the trench were analyzed by wet sieving with meshes from bigger 2mm to bigger 0.063mm. A grain size distribution graph was constructed out of the collected data.

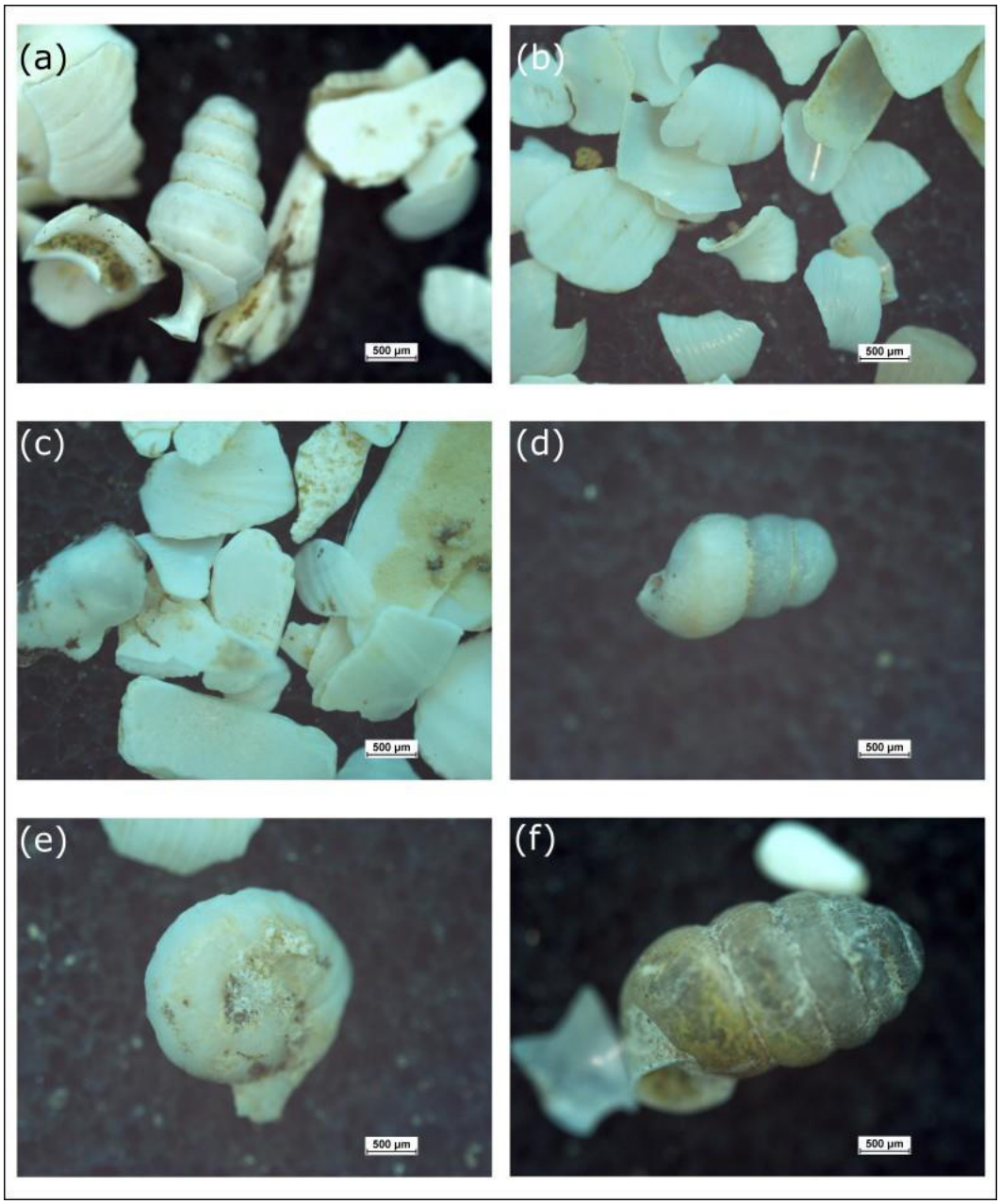

Fig. 11: Examples of loess gastropods from layer C1 (a) and C2 (b), S1 (c and d), L1 (e), L2 (f).

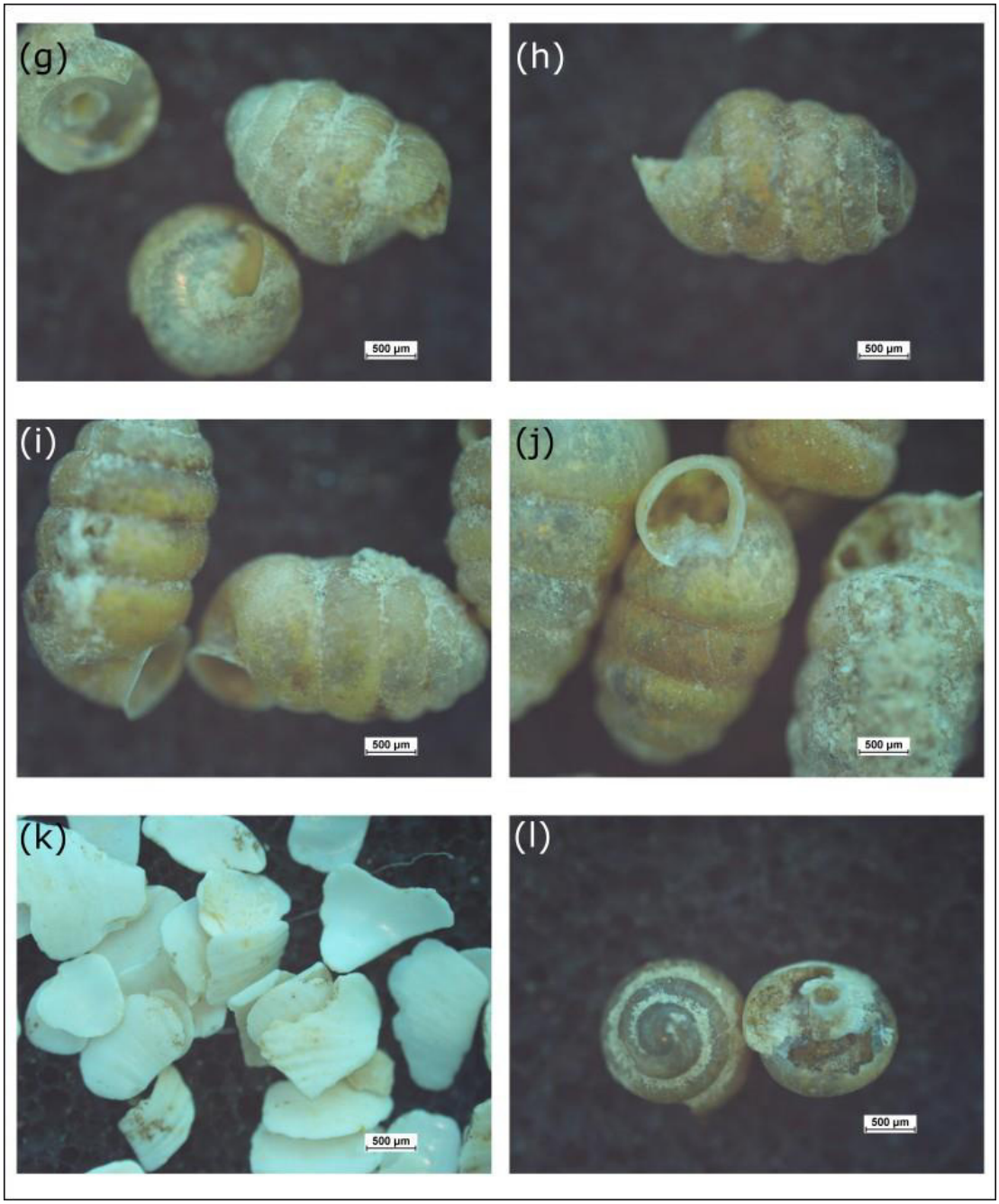

Fig. 12: examples of loess gastropods from layer L3A (g), L3B (h), L4A (i), L4B (j), L5 (k), L6 (l).

4.5 Radiocarbon dating (^{14}C)

The atmosphere constantly forms ^{14}C by the interaction of neutrons with ^{14}N and oxidizing the ^{14}C in air forming carbon dioxide which enters then the global carbon cycle. Radiocarbon dating is based on the isotope value of $^{14}C/^{12}C$ in an organism/sample. The lighter ^{12}C isotopes are stable while the heavier ^{14}C isotopes are radioactive and their nucleus is unstable due to their size. When the organism dies the exchange of ^{14}C with the atmosphere ends and no more ^{14}C can be absorbed and stored. The $^{14}C/^{12}C$ value declines due to the half-life of ^{14}C which is approximately 5 730 years. However, this method is only applicable in a geological short time frame. Within approximately 50 000 years the ^{14}C is completely depleted (Madea et al. 2015).

To receive ages from the sediment layers in the trench ten gastropod samples were assigned to Beta Analytic Laboratory. They use accelerator mass spectrometry (AMS) for radiocarbon dating in which the ^{14}C content of the sample is measured relative to ^{12}C and ^{13}C. As terrestrial gastropods contain about 12% carbon by weight and remain closed systems with respect to carbon, they are therefore ideal for dating purposes in loess deposits (Pigati et al. 2013).

4.6 Calcite encrustations

Several calcite crusts, enclosing pebbles, with an unusual pock like shape were found after sieving the loess, sand and gravel samples. Out of 33 encrustations a thin section, with a thickness of 30 micrometers, was made and observed under an optical Leica-microscope. Pictures were taken with the Leica DFC420 camera.

5 Results

5.1 Quaternary thickness from borehole data and geophysical measurements

The evaluation of the borehole data from the ÖMV and from the company Kovanda GmbH show a varying Quaternary thickness in all profiles. The highest Quaternary thickness in profile G1 is recorded at 2400 m (Fig. 13). At the western and eastern end of profile G1 the Quaternary thickness reaches only heights of 3.8 m in the west and 10 meters in the east, whereas at 2400 meters the Quaternary thickness reaches up to 26 meters.

Data from borehole 5141 in profile G1, which is located on the western most part of the investigated area, show a Quaternary thickness of only 3.8 m. At 2700 m the Quaternary base is offset by about 10 to 15 m. The Quaternary deposits from profiles G2-G4 also show a varying Quaternary thickness. In profile G2 the maximum Quaternary thickness of 22 m is visible in borehole 5181 which is located in the middle of the profile (G2). In the NW and the SE, the Quaternary gravel reaches a thickness of about 10 m. A clear depression of the Quaternary base is visible between boreholes 5177 and 5182 (Fig. 14). In profile G3 the Quaternary thickness increases from the west to the east. In the west it reaches a maximum thickness of 15.5 m and in the east only 10.3 m (Fig. 15). The Quaternary gravel in profile G4 reach a maximum thickness of about 17 m (borehole 50) in the SE part of the profile. The Quaternary thickness in the profile is varying between 6 m (borehole 37) in the middle part of the profile and 17 m in the SE. Between 1700 m and 2300 m, between blastholes 43 and 50, the Quaternary basis is offset of about 15 to 20 m. (Fig. 16).

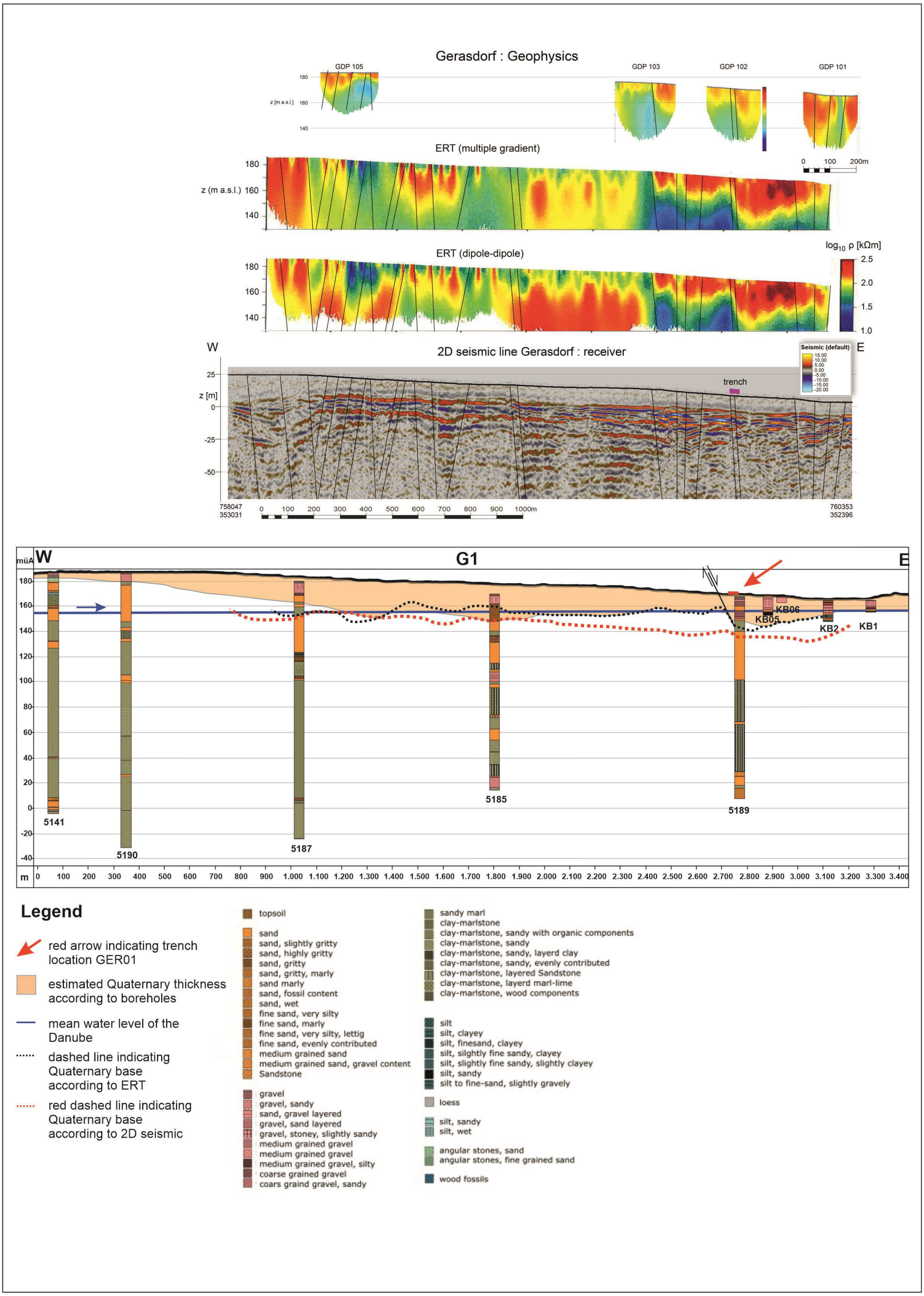

Fig. 13: Short ERT profiles (G101, G102, G103, G105) and long ERT profile. 2D seismic profile with interpreted faults (black lines). Profile G1 showing Quaternary thickness (orange) in profile G1 derived from borehole data from the OMV AG and Kovanda GmbH. Black dashed line indicating Quaternary base according to ERT measurements; red dashed line indicating Quaternary base according to 2D seismic. Mean water level of the Danube as well as flow direction indicated with blue arrow; red arrow indicating trenching location. Black arrows indicating fault (SFS).

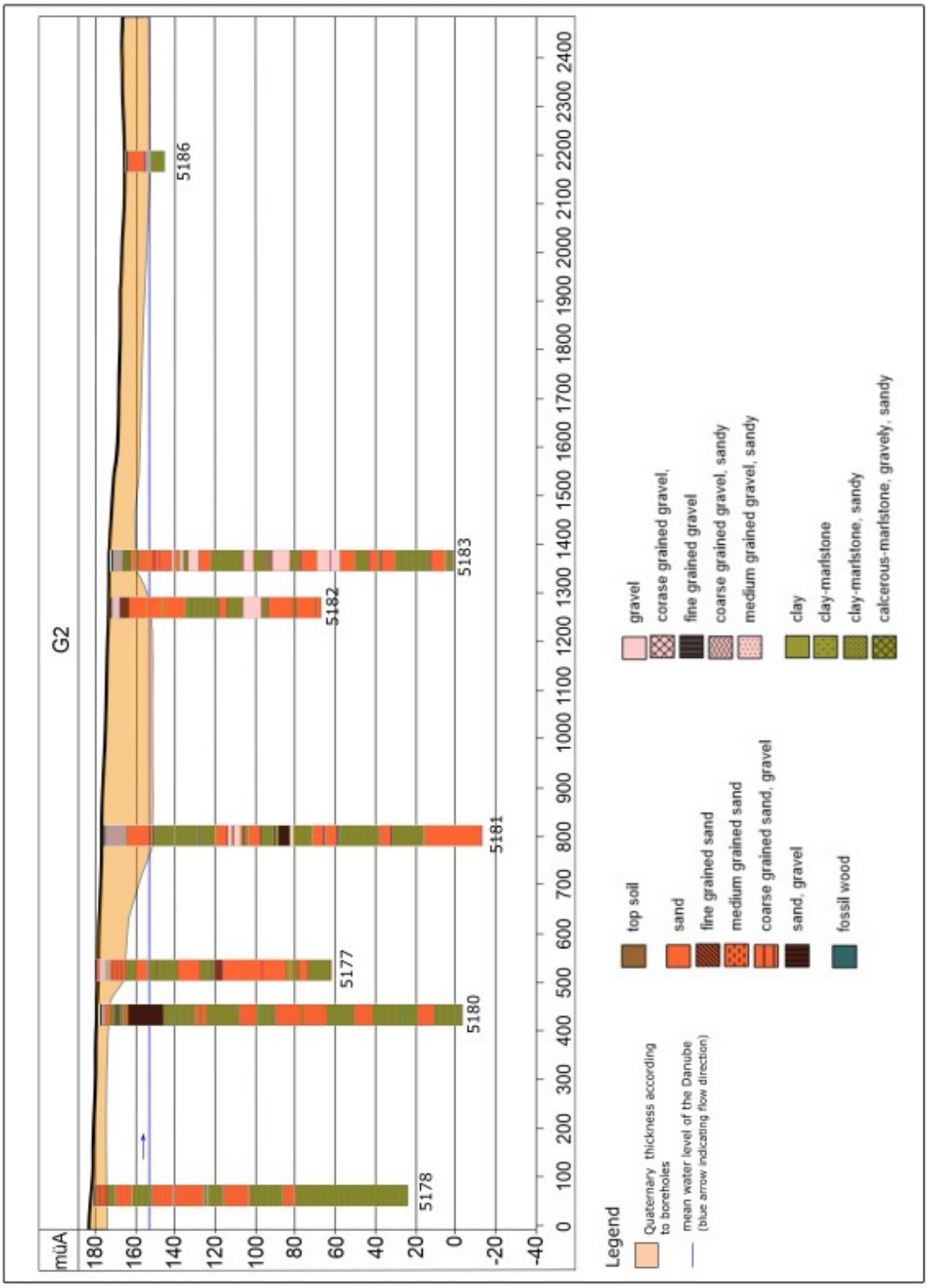

Fig. 14: Quaternary thickness (orange) in profile G2 derived from borehole data from the OMV AG. Mean water level of the Danube as well as flow direction indicated with blue arrow

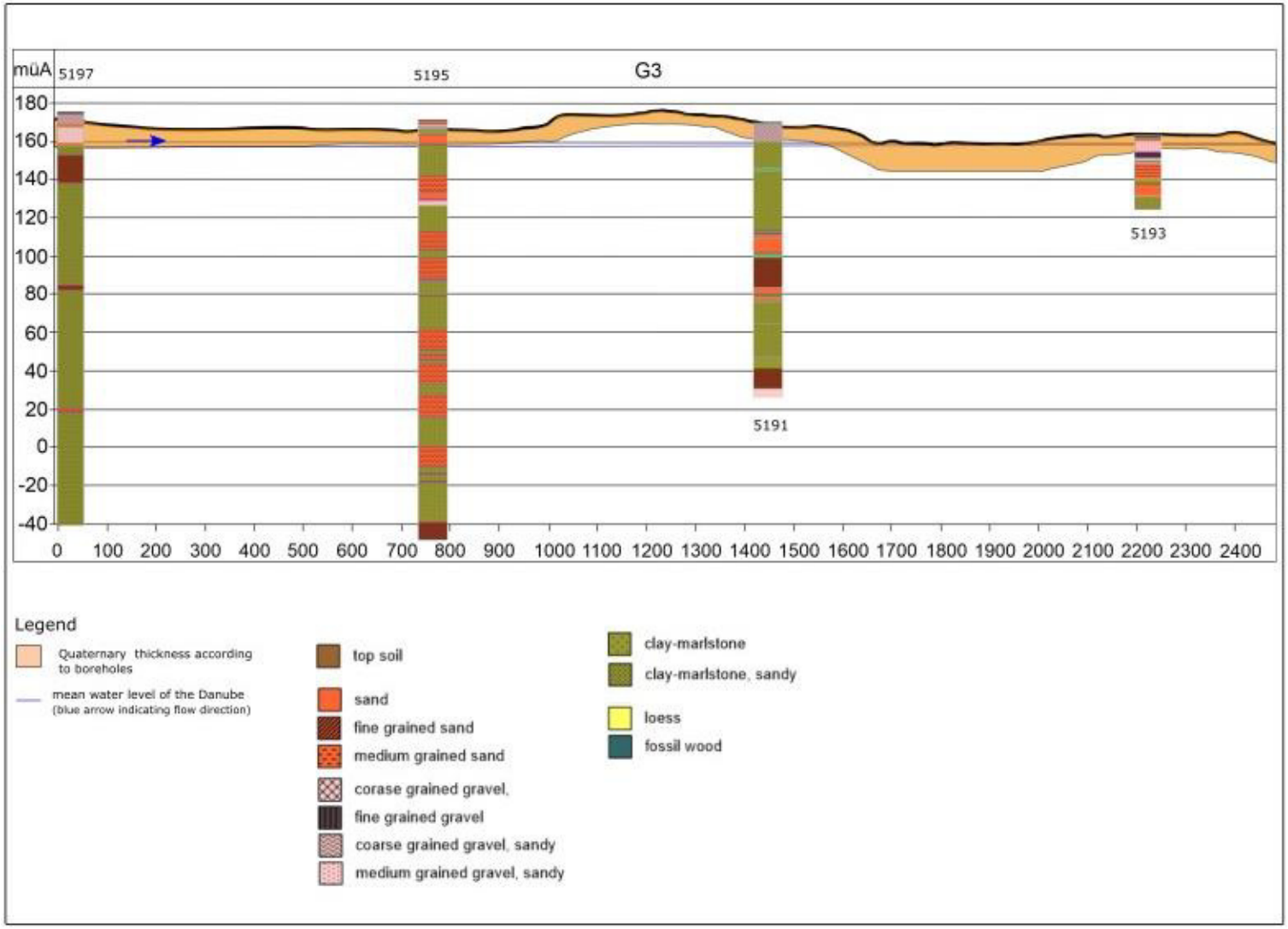

Fig. 15: Quaternary thickness (orange) in profile G3 derived from borehole data from the OMV AG. Mean water level of the Danube as well as flow direction indicated with blue arrow.

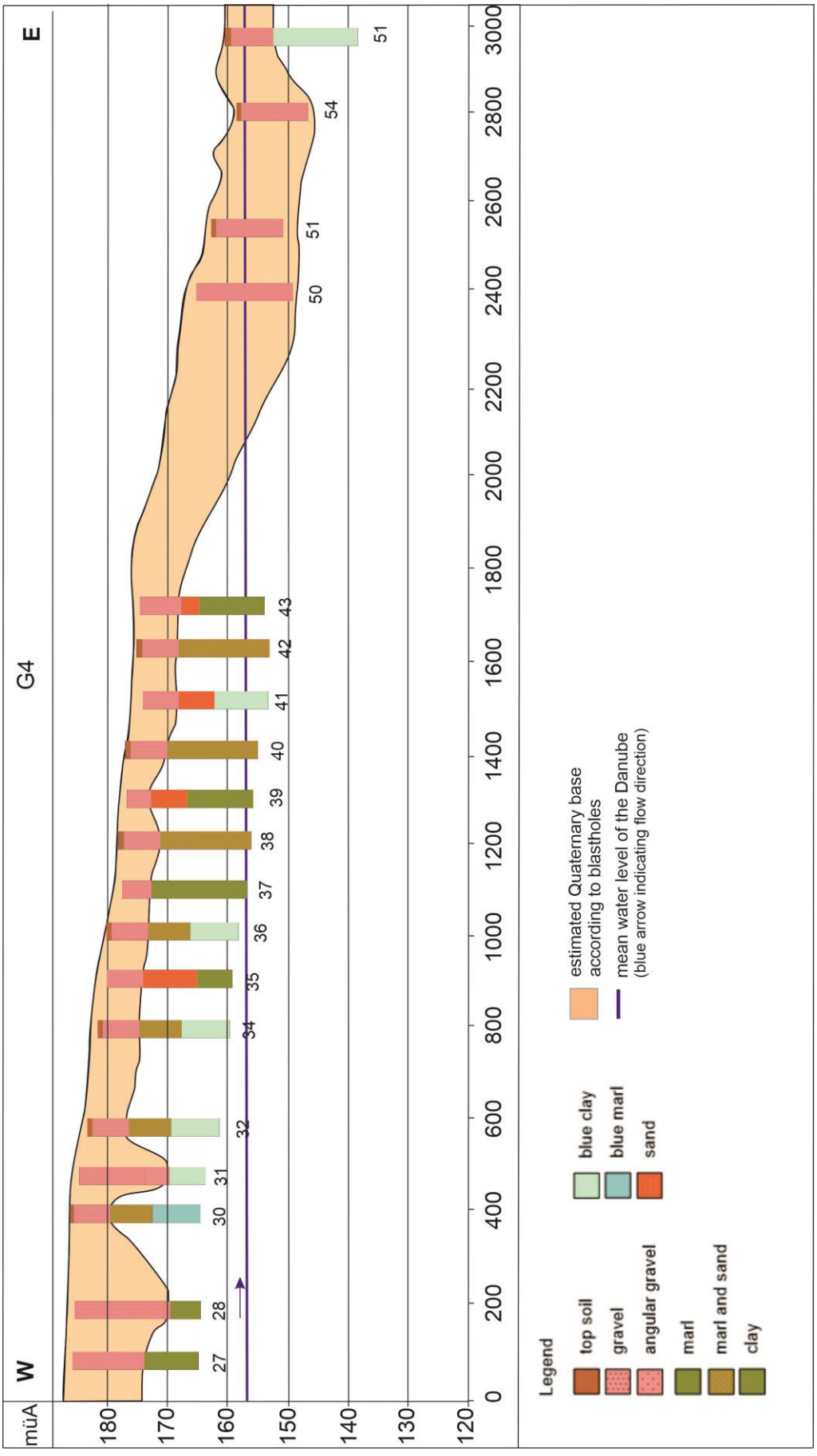

Fig. 16: Quaternary thickness (orange) in profile G4 derived from blast hole borehole data. Mean water level of the Danube as well as flow direction indicated with blue arrow.

5.2 Geophysical measurements

ERT measurements along the Salzstraße (profile G1) north of Gerasdorf show numerous indications of faults (Fig. 13). The most obvious indications of faults interpreted from ERT profile G1 where covered with four high-resolution ERT profiles (Fig. 17). Based on these profiles, faults could be localized with a horizontal precision high enough to select possible sites for Paleoseismological trenching.

Profile GDP 101 shows in the west and east high resistivity areas (in red and orange) which can be regarded as Quaternary gravels. Between meters 40 and 80 in this profile Miocene sediments indicated by a lower resistivity (green) separates the two red areas and might be an indicator for faulting. the Quaternary sediments (in red and orange) reach a thickness of up to approximately 30 m in the east (Fig. 17 and Fig. 18). GDP 102 and GDP 103 show depressions of Quaternary sediments with a high resistivity (yellow and orange) on the eastern side of the profile at 120 m and 140 m onwards, respectively (Fig. 17). GDP 102 shows a Quaternary thickness (red and yellow) of approximately 30 m in the east over more clayey Miocene deposits (blue). In the east the Quaternary thickness is only approximately 20 m. GDP 103 also shows approximately 20 m thick Quaternary deposits (red, yellow) in the east, whereas in the west the Quaternary thickness only reaches a height of up to 10 m. In the central part of the profile clayey Miocene deposits reaches a height of up to 10 m under the surface. In GDP 102 two normal fault branches and in GDP 103 one normal fault branch were interpreted to cause the depressions in both profiles and cause local subsidences, respectively (Fig. 18). The high resistivity area (red and orange) in GDP 105 is increasing to the west, showing significant areas in red between 20 and 50 m, 60 m and 80 m, 100 m and 120 m, 140 and 160 m and 170 m onwards toward the east. Whereas between 120 m and 170 m the low resistivity sediments of the Miocene nearly reach the top (Fig. 17). In GDP 105 five faults were interpreted between the high resistivity areas shown in red. GDP 105 shows a Quaternary thickness of 20 m in the west and thins out to the east, where it reaches heights of up to 10 m (Fig. 18).

Four Profiles reveal several promising trenching locations to investigate branch faults of the Seyring Fault System. Profile GDP 103 shows a promising location of a fault but the trench would have had to cross a road and therefore trenching was more difficult to execute. A location more to the east determined by GDP 102 was chosen because it shows a sharp offset of the base of the Quaternary gravel. The regional ERT profile shows that locally the basal Quaternary unconformity is dipping to the east against the flow direction of the Danube (Fig. 18). GDP 101 and 105 did not show fault locations as clearly and were therefore not considered as an option for trenching.

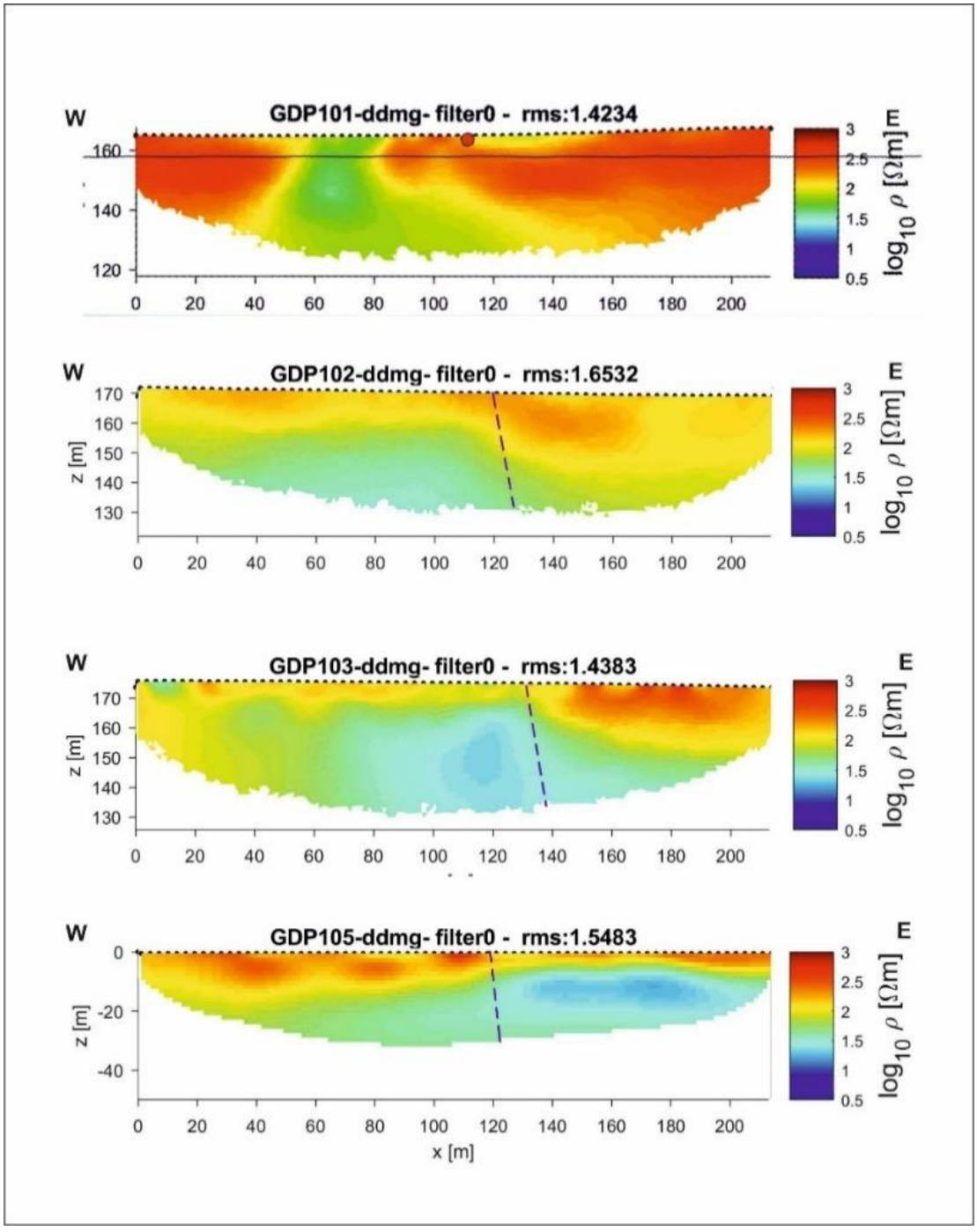

Fig. 17: ERT measurements GDP 101, GDP 102, GDP 103, GDP 105, with interpreted faults shown as dashed lines. The contrast between Quaternary fluvial sand and gravel (red and orange) and Miocene clayey sediments (blue and green) shows offsets and indicates the location of the unconformity at the base of the Quaternary sediments.

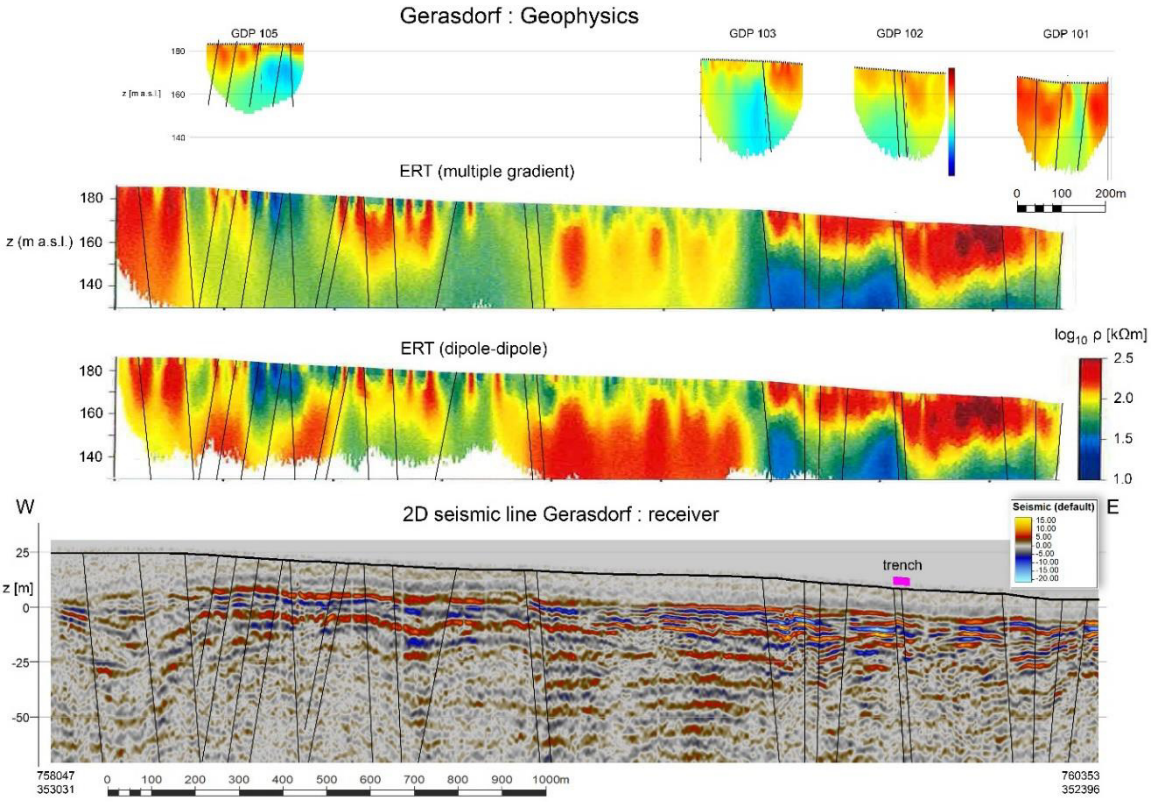

Fig. 18: ERT measurements and seismic profile with interpreted faults (black lines). The contrast between Quaternary sand and gravel (red and orange) and Miocene clayey sediments (blue and green) shows offsets and unconformities which are also visible in the seismic profile. Trenching location as pink line; after M. Weissl, pers. comm.

5.3 Lithological description of the Paleoseismological trench GER01

To observe the seismicity of the Seyring Fault System, in January 2021 a 32 m long, 1.5m wide and in maximum 3.5 m deep trench was opened along a fault segment in Gerasdorf which is situated 3.4 km NNE of Vienna along the E-W trending Salzstraße. The trench was excavated parallel to the road. The northern wall and the central part of the southern wall were cleaned and a coordinate grid which was 1 m x 1 m (with the description A1 to D31 on the northern trench wall and A0 to D5 on the southern trench wall) was spread out on the face of the walls.

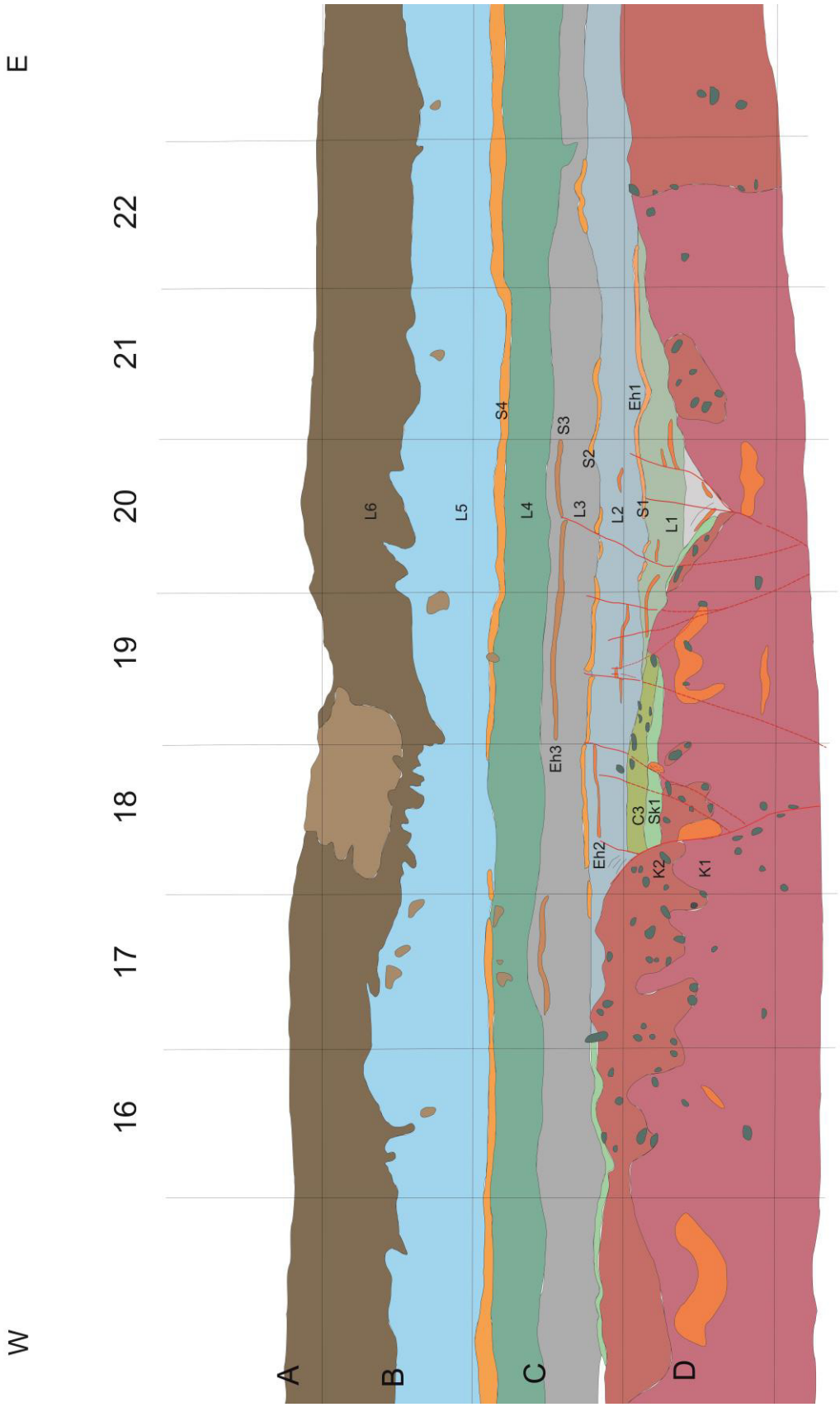

Fig. 19: Clipped northern trench wall. Gravel layers K1 and K2 (pink and red, respectively), with sand intercalated lenses (orange). SK1: medium grained sand layer with gravel components (turquoise). C3: colluvial wedge (green). L1: loess layer (grey). S1, S2 and S3: sand layers (orange). L2: loess layer (light grey). L3: loess layer (dark grey). L4: loess layer (dark turquoise). S4: wind-blown sand layer (orange). L5: loess layer (light blue). L6: top soil (brown). Eh1 – Eh3: event horizons 1 – 3. Red lines: faults. Red dashed lines: presumed faults, not visible. grey circles: pebbles. Light grey shapes: bioturbation.

On both trench walls a lithological sequence with gravel layers on the bottom and alternating loess and sand layers on the top can be observed (Fig. 19). In Fig. 20 a schematic sketch of the lithological sequence is presented:

1. The lowermost layers of the trench are composed of Pleistocene fluviatile sandy gravel layers (K1 and K2) deformed by cryoturbation followed by
2. a sequence of loess and fine to medium grained sand layers (L1 and S1 to S4 and L4) followed by
3. a loess layer (L5) which is heavily deformed by bioturbation
4. The topmost layer consists of very dark brown fine grained clayey, sandy silt which is transformed to chernozem.

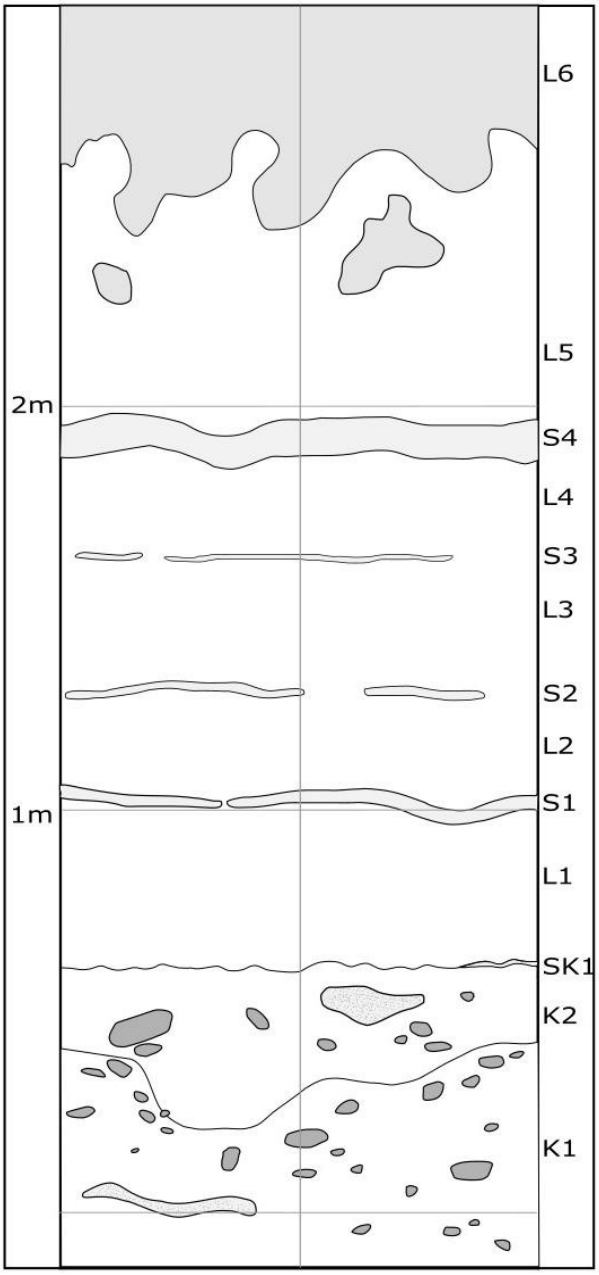

Fig. 20: Lithological sketch of the sedimentary succession observed in the trench GER01. Different sand layers in grey with cryoturbated sand lenses (light grey with dotted filling) in gravel layers. Larger gravel components in dark grey. Bioturbated top soil in middle grey.

The lower part of both trench walls consist of fine to coarse sandy gravels (K1 and K2) which were exposed on the trench wall, with a thickness of up to 1.5 m in total (Fig. 19). Sandy gravel is intercalated with sand lenses of up to 20 cm thickness and half a meter length.

The bottom gravel layer (K1) has well sorted and well-rounded fine to medium grained fluvial gravel components with a maximum grain size of 5 cm. This layer is matrix supported with a matrix consisting of fine to medium grained sand. The sandy matrix contains fragments of terrestrial gastropods. The gravel is a polymict with a high amount of quartz and crystalline components, carbonate components were not recorded (Table. A. 2). The grain shape is round, some of the grains are elongated but most of them are cubic and spherical in shape. The layer is not stratified. The grain size distribution of K1 shows well graded medium grained gravel with most of the grain sizes between 0.1 and 1 mm as well as 6.3 and 20 mm (Table. A. 4). Some of the gravel are encrusted by calcite cement which is very uneven and displays a pock-like surface. Thin section analysis of this crusts reveals cemented calcite enclosing quartz grains which are from the pock-like surface of the crust as well as a layered structure of the calcite (Fig. 21).

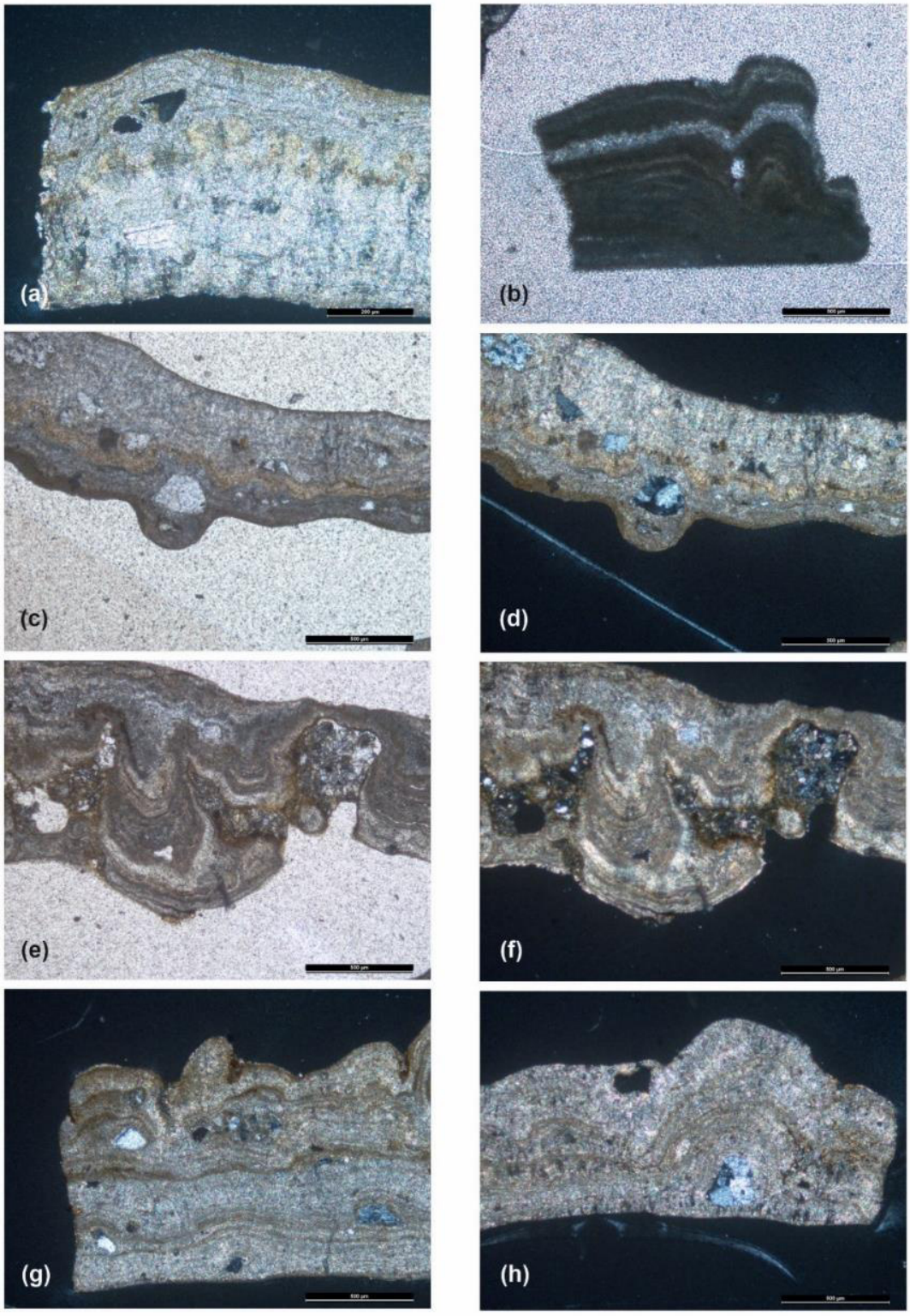

Fig. 21: Thin sections of calcite crusts enclosing quartz grains. Layered structure of calcite due to multiphase growth. Pictures a, d, f, g and h in cross polarized light. Pictures b, c and e in plain polarized light.

Layer K1 has a grey to brown color (Fig. 26a) which, according to the Munsell color chart, shows a color code of (2.5Y 4/3) where 2.5Y is the Hue, 4 is the Value and 3 is the Chroma. The orientation of the long axes of the pebbles on the northern and southern trench wall of the gravel layers show preferred orientations and therefore were measured. The pebbles show a steep orientation between 70 and 90° towards the west and some towards the east (Fig. 22).

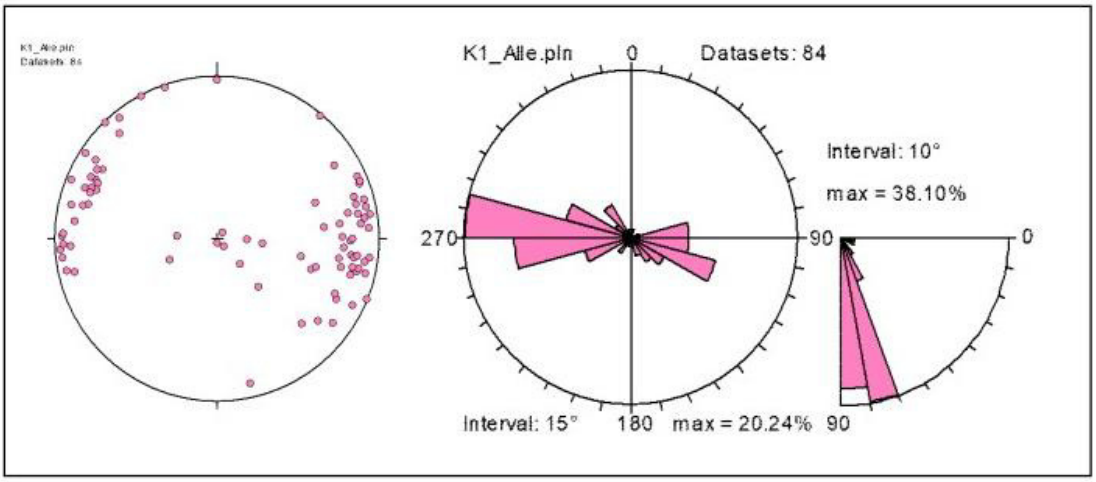

Fig. 22: Stereoplot of pole points and rose diagram of pebble orientation in K1.

The second gravel layer (K2) consists of sandy coarse gravel with stones. The sediment is matrix supported with well-rounded pebbles up to 15 cm in diameter and a medium grained sand matrix. The gravel is not stratified or laminated, pebbles consist dominantly of quartz and a few metamorphic rock components. The grains are mostly square and platy and angular (Table. A. 5). The quartz components are often cemented with calcite and form a pock-like surface (Fig. 21). The grain size distribution shows that most of the grains have sizes between 0.1 and 1 mm and 6.3 and 63 mm which is a sandy fine to coarse grained gravel (Table. A. 3). The color is grey to brown (Munsell code 2.5Y 4/3) (Fig. 26b). The long axes of pebbles show mostly a steep west orientation with angles between 80 and 90° (Fig. 23). However, the orientations of the gravels are more scattered than in K1, indicating cryoturbation. The lower contact to the gravel layer K1 is not horizontal and as in K1 there are some sand pocket formations in the gravel layers.

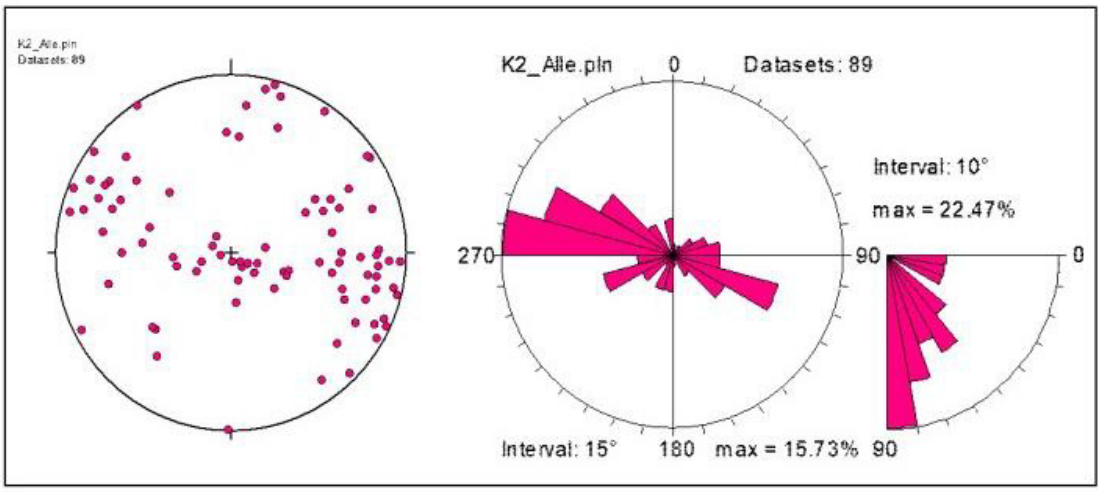

Fig. 23: Stereoplot of pole points and rose diagram of pebble orientation in K2.

The layer SK1 is up to 9 cm thick and is not continuously visible throughout the trench profile (Fig. 19). SK1 is only visible on the middle and western part of the trench between meters 5 and 7 and between meters 14 and 19. This layer consists of medium grained sand with fine grained gravel components. It is matrix supported, gravel components are well rounded and sometimes depict coarse sub-horizontal lamination. There is no preferred orientation of the rounded components. The sediments show horizontal lamination adjacent to the fault (Fig. 26f).

This layer is off-set by a fault in the middle part of the trench and lies 49 centimeters lower on the hanging wall than on the footwall (Fig. 19). This layer is only visible on the western and middle part of the trench wall and thins out towards the east.

Three wedge-shaped layers (C1, C2 and C3) which can only be found in the central part of the trench follow the gravel layer (see paragraph on deformation history). C1 and C2 overlie gravel K2, C3 also rests directly on K2 and SK1 (Fig. 19 and Fig. 24).

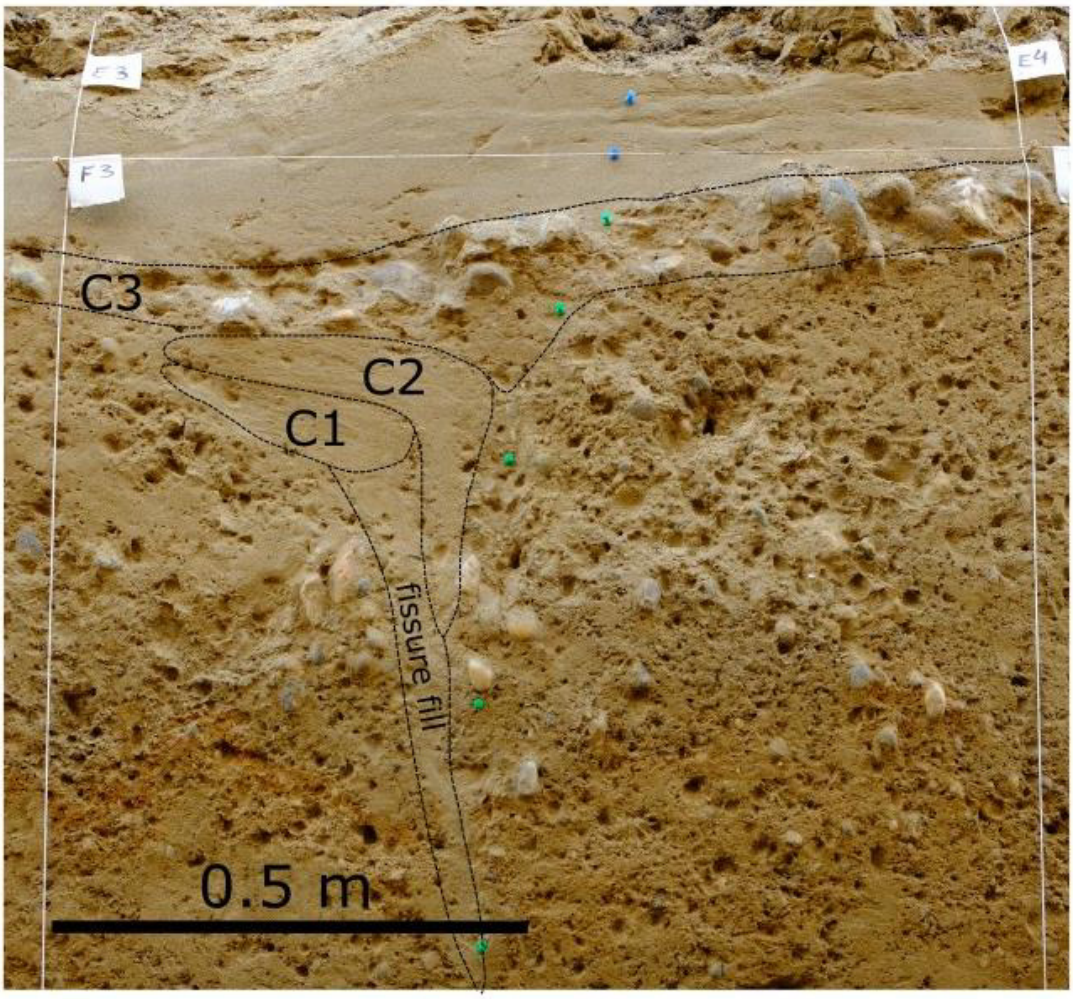

Fig. 24: C1, C2 and C3 on the southern trench wall and fissure fill. Green and blue needles indicate location of fault F1.

The southern profile wall exposed two small wedge-shaped layers of fine to medium grained gravel (C1 and C2) (Fig. 24). Those layers are very poorly sorted. C1 has a thickness of about 7 cm and extends laterally for about 20 cm, C2 is about 7.8 cm thick. C2 directly connects to fault F1 and extends to a distance of 50 cm from the fault. Material of C2 fills a tension fissure adjacent to fault F1. C1 and C2 are brown in color (Munsell code 2.5Y 6/3) (Fig. 26 c, d). The two layers are only exposed on the southern trench wall.

The wedge-shaped gravel layer C3 lies above layers C1 and C2. This layer is visible on both trench walls. The sediments of layer C3 on the northern side of the wall are adjacent to the fault. The layer consists of fine to medium grained gravel and is very poorly sorted.

On the southern trench wall, the layer (C3) consists of coarse gravel with stones and a matrix of sandy medium grained gravels. The pebbles show imbrication and NW or SW orientation (Fig. 25). On the western part the layer is up to 16 cm thick and it decreases in thickness to the east. It is approximately 1.5 m long and displays a “V” shape.

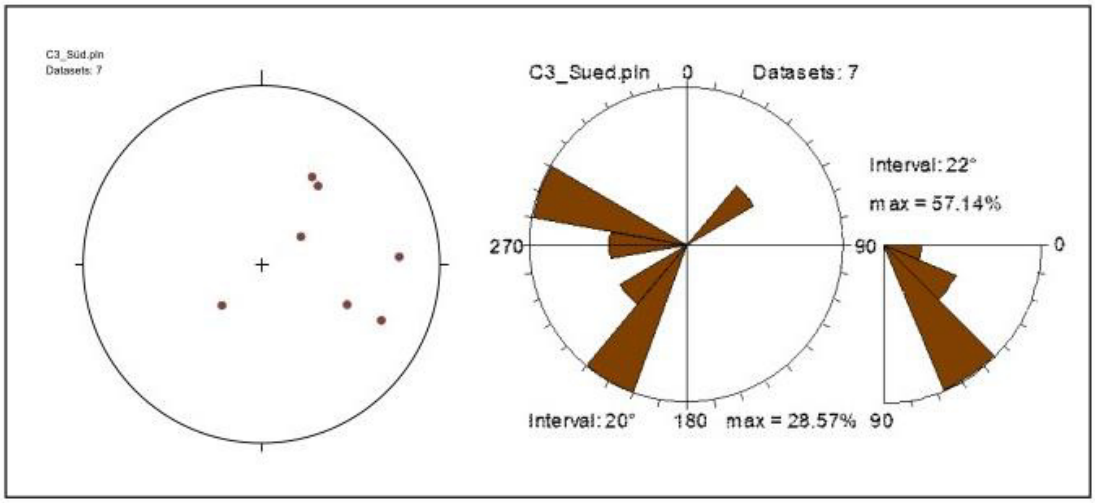

Fig. 25: Rose diagram of pebble orientation of C3 on the southern trench wall.

The sediments of C3 on the northern side of the wall directly lie against fault F4 (Fig. 35). On the northern trench wall, the layer consists of fine to medium grained gravel and stones and a sandy matrix. Long axes of elongated pebbles are orientated horizontally; some pebbles show imbrication towards the NW and SW. On the western part the layer is in maximum 19.5 cm thick and it decreases in thickness to the east. It is traced to a distance of approximately 1.5 m from fault F4. The gravel layer shows horizontal lamination (Fig. 26e).

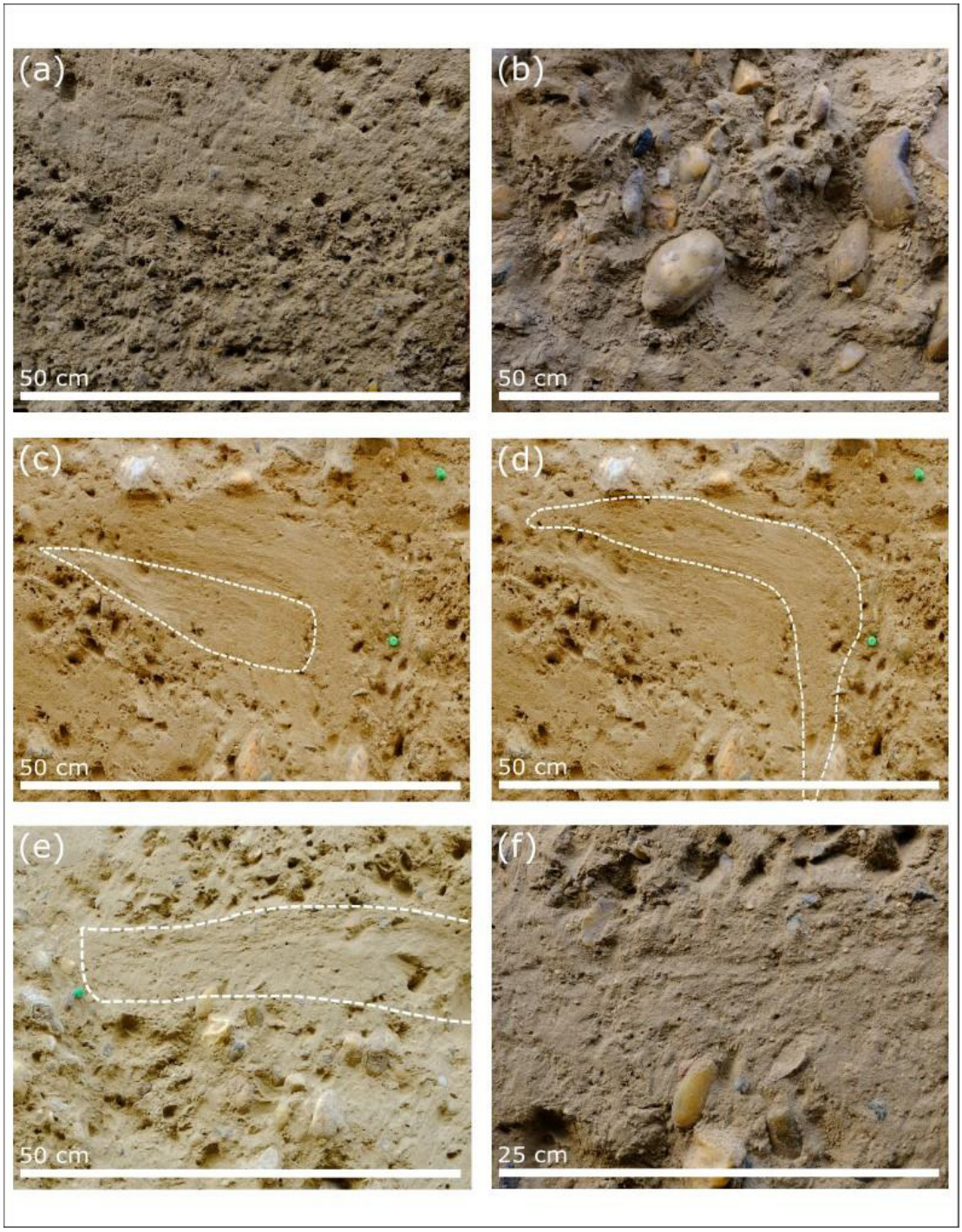

Fig. 26: gravel layers K1 (a), K2 (b), SK1 (f) and colluvial wedges C1 (c), C2 (d) and C3 (e).

The gravel layers K1, K2 and the wedge-shaped deposits C1 to C3 are overlain by a sequence of up to 2.5 meters of alternating loess and sand (Fig. 19).

The bottom most layer (L1A and L1B) of this succession is a silty fine-grained sand. L1A is on the bottom of this layer and is displaying lamination dipping with about 25° to the E. L1B lies on top of L1A and is showing horizontal plane lamination. Together, layers L1A and L1B are up to 30 cm thick and extend over 3m between running meters 19 and 22 of the trench near fault F2, apparently filling a pre-existing relief next to the fault (Fig.

35). The layer contains several distinct sand layers. The color of this layer is grey to brown (Munsell code 2.5Y 8/1) (Fig. 28a). L1 consists of 55.4 % silt and of 39.6 % fine grained sand and of 5% medium to coarse grained sand which defines it as a sandy loess (Fig. 32) (Table. A. 6).

On top of L1 lies a fine to medium grained sand layer (S1) (Fig. 19). However, due to the small sample size it was not possible to determine a grain size distribution. S1 is approximately 4 cm thick. This layer is well sorted and the color is very light brown to grey (Munsell code 2.5Y 5/4) (Fig. 29a). Layer S1 is only traceable in this part of the trench, running meters 19 to 22.

Next comes a layer (L2) that consists of 57.8 % silt, of 37.8 % fine grained sand and of 4.4% medium to coarse grained sand which defines it as sandy loess (Fig. 32) (Table. A. 6).This layer is a little bit darker brown then L1 (Munsell color 2.5Y 5/3) (Fig. 29b). This layer has a maximum thickness of 23.5 cm and extends over 15 m over the trenching wall. L2 is only visible on the eastern side (hanging wall). It reappears in the middle western section of the wall but there it reaches only a thickness of 20 cm over a length of about 4.5 meters. This layer is completely absent on the most western section of the wall. L2 is presumed to be loess because of its grain size and the thickness of the layer. In L2 cemented rootlets (rhizolithes) could be observed (Fig. 27).

Fig. 27: Cemented rootlets(rhizolites) in L2.

Sand layer S2 overlays L2 and separates L2 from L3 (Fig. 19). It is not continuous but interrupted at several locations. It is up to 2 cm thick; the longest laterally continuous layer extends over a length of 2 m. This layer consists of medium grained sand without a silt fraction. S2 is of a light greyish color (Munsell color 2.5Y 7/1) (Fig. 30b). Due to the small sample size it was not possible to retrieve enough material for a grain size distribution analysis.

Above S2, an up to 50 cm thick loess layer (L3) is mapped through the whole profile of the northern and southern wall (Fig. 19). It consists of fine-grained sand and silt which has a light brown color (Munsell code 2.5Y 5/3) (Fig. 29c). L3 consists of 55.79 % silt and of 36.79 % fine grained sand and 7.42% medium to coarse grained sand which defines it as sandy loess (Fig. 32) (Table. A. 6). Some parts of this layer (mostly on the eastern side of the northern wall) show darker spots (Munsell code for the darker spots 2.5Y 6/2) (Fig. 29c). These spots are presumably signs of “pseudovergleyung” caused by reduction processes from Fe^{3+} to Fe^{2+} due to precipitation or waterlogging above ground frost. During dry periods when oxidizing conditions prevail, Mn and Fe are precipitated, causing reddish-brown spots (Peticzka and Weissl, pers. Comm.). The layer contains a fine to medium-grained sand horizon (S3). The sand layer is well sorted, devoid of silt and shows horizontal lamination. The layer is 1 cm thick and interrupted at several locations. This layer is mostly visible in the central part of the trench wall above the faults F4 and F5. The color of this layer is greyish brown (Munsell color 2.5Y 8/1) (Fig. 30c). S3 consists of 54.93% loess or silt and of 40.95% fines grained sand and of 4.12% medium to coarse grained sand (Fig. 32) (Table. A. 6).

The layer above L3 is an up to 30 cm thick fine-grained sand and silt layer with greyish color (Munsell color 2.5Y 5/4) referred to as L4 (Fig. 29d). L4 is distinguished from L3 by its darker color. Also L4 shows no signs of drainage spots. L4 consists of 64.07% silt and 32.51% fine grained sand and of 3.41% medium to coarse grained sand which defines it as sandy loess (Fig. 32) (Table. A. 6).

L4 is topped by a fine to medium grained sand layer (S4) (Fig. 19). The layer is laminated and up to 29 cm thick (Fig. 30d). S4 consists of 22.65% silt or loess and of about 69.57% fine grained sand and of 7.78% medium to coarse grained sand (Fig. 32 and Fig. 34) (Table. A. 6). This layer is well sorted with grain sizes mostly between 0.063 mm and 0.25 mm. The color is light grey (Munsell color 5Y 8/1). This sand layer separates L4 from the next layer L5 which consists of fine-grained sand and silt which is brownish in color (Munsell color 2.5Y 6/5) (Fig. 29 e) and is up to 50 cm in thickness. L5 consists of 53.5% fine grained sand, 43.78% silt and of 2.71% medium to coarse grained sand (Fig. 32) (Table. A. 6). This layer shows darker spots of the layer above (L6) through the whole profile (Fig. 28).

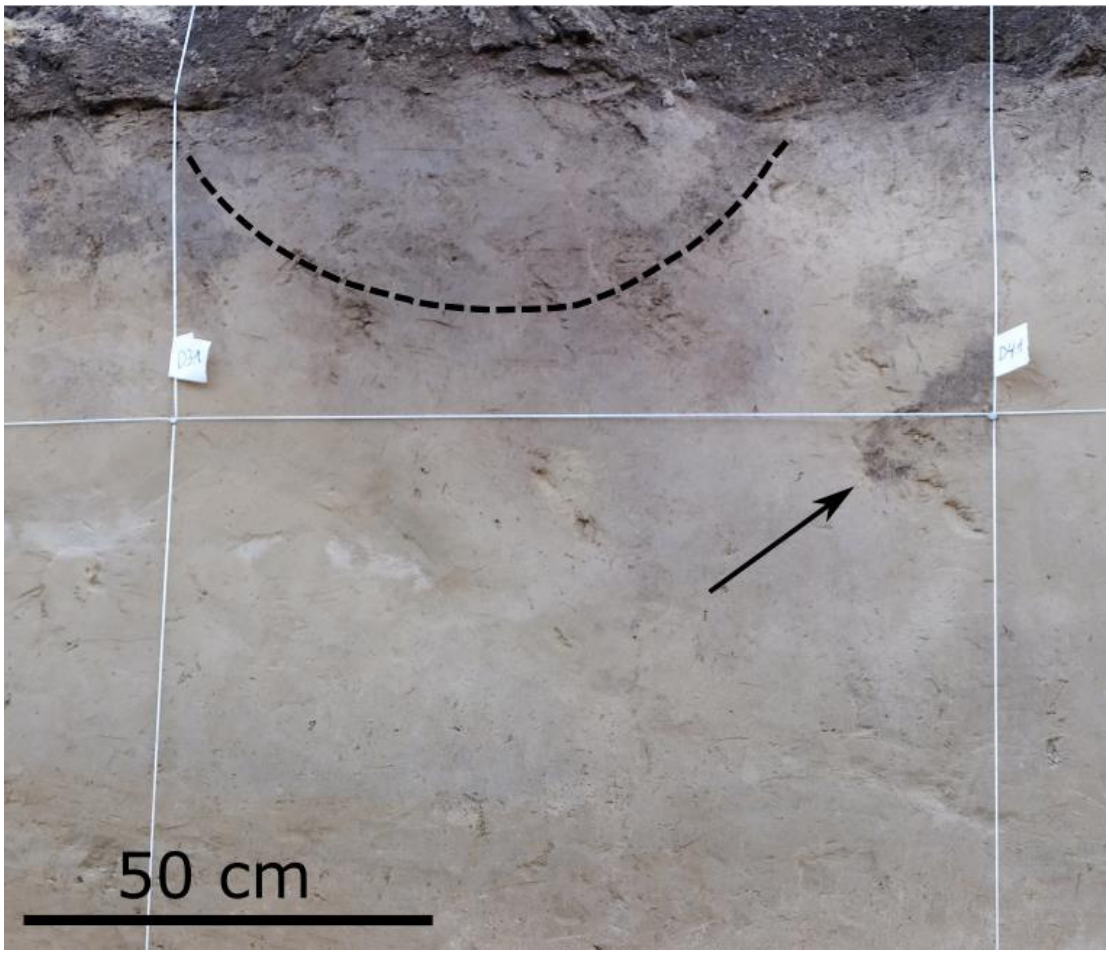

Fig. 28: Bioturbation in layer L5 shown as darker spots. Large depression of L6 into L5 is presumed to be a fox den.

The last and upper most layer (L6) consists of fine grained silty and clayey sand, and is up to 80 cm thick. L6 consists of 32.01% silt , 61.11% fine grained sand and of 6.88% medium to coarse grained sand (Fig. 32). This top soil layer shows a very distinct dark brown color (Munsell color 10YR 3/2 or 4/3) (Fig. 29f). On the southern trench wall, a prominent depression of L6 which bulges down 1.5 m into layers L5 to L3 can be observed at running meters 3 to 5 (Fig. 28).

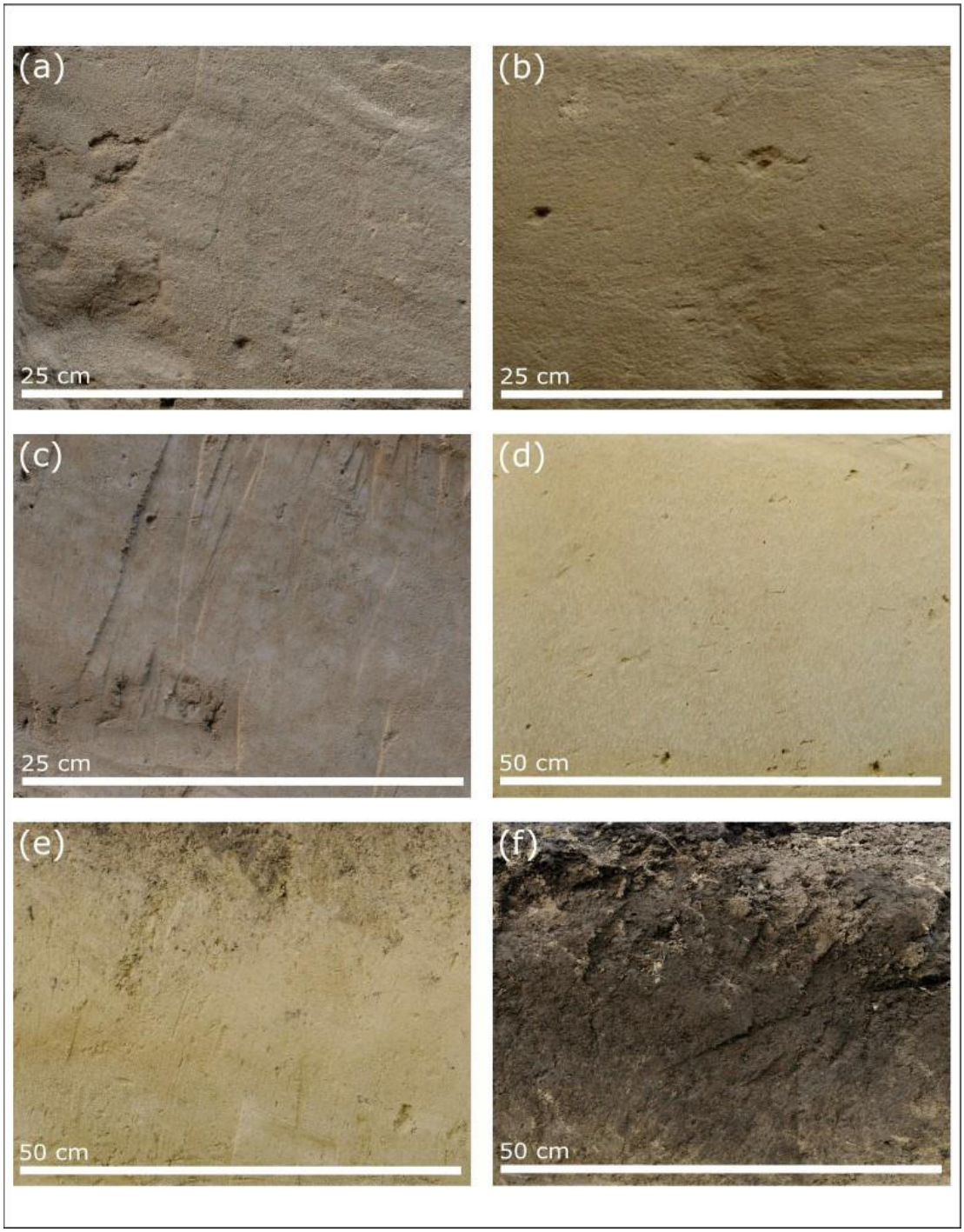

Fig. 29: Loess layers from oldest to youngest: L1 (a), L2 (b), L3 (c), L4 (d), L5 (e), L6 (f).

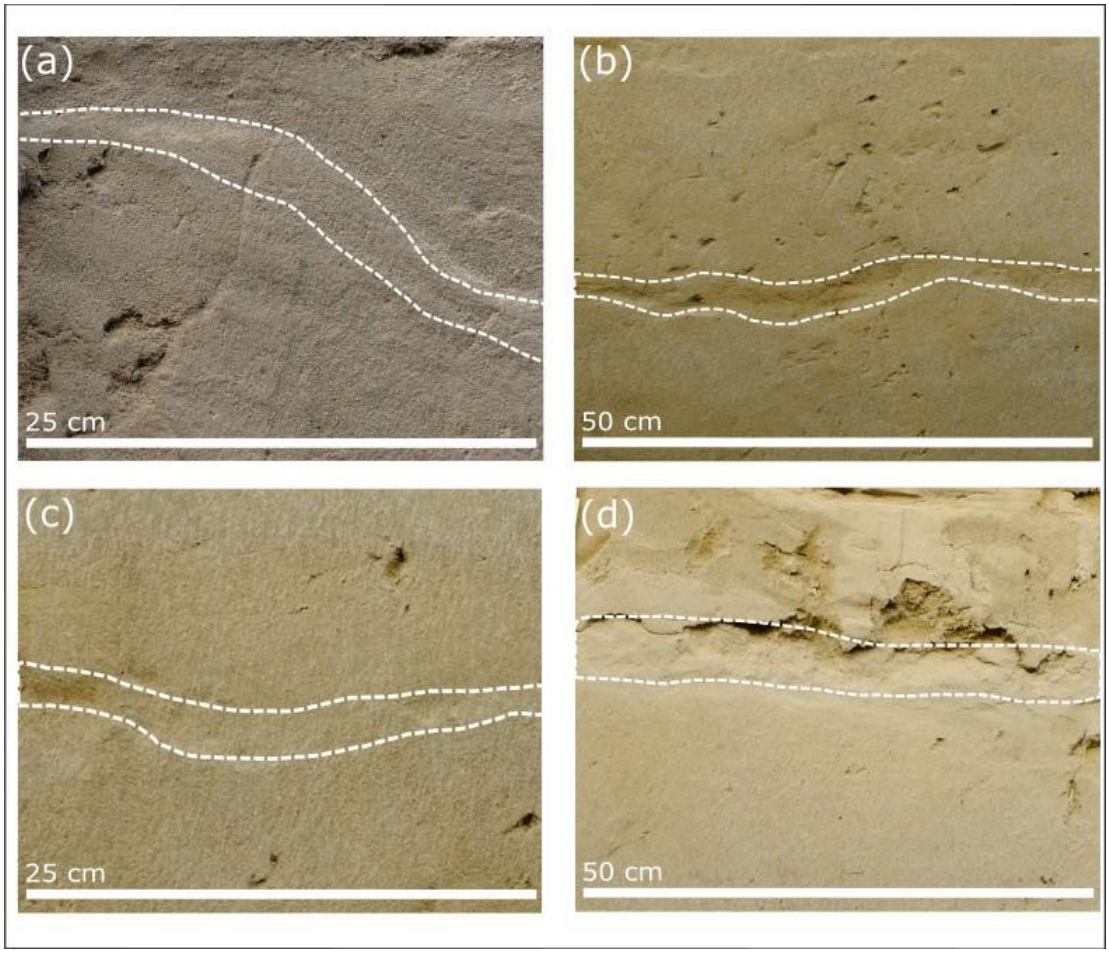

Fig. 30: Sand layers from oldest to youngest: S1 (a), S2 (b), S3 (c), S4 wind-blown sand (d). White dashed line encloses the sand layers.

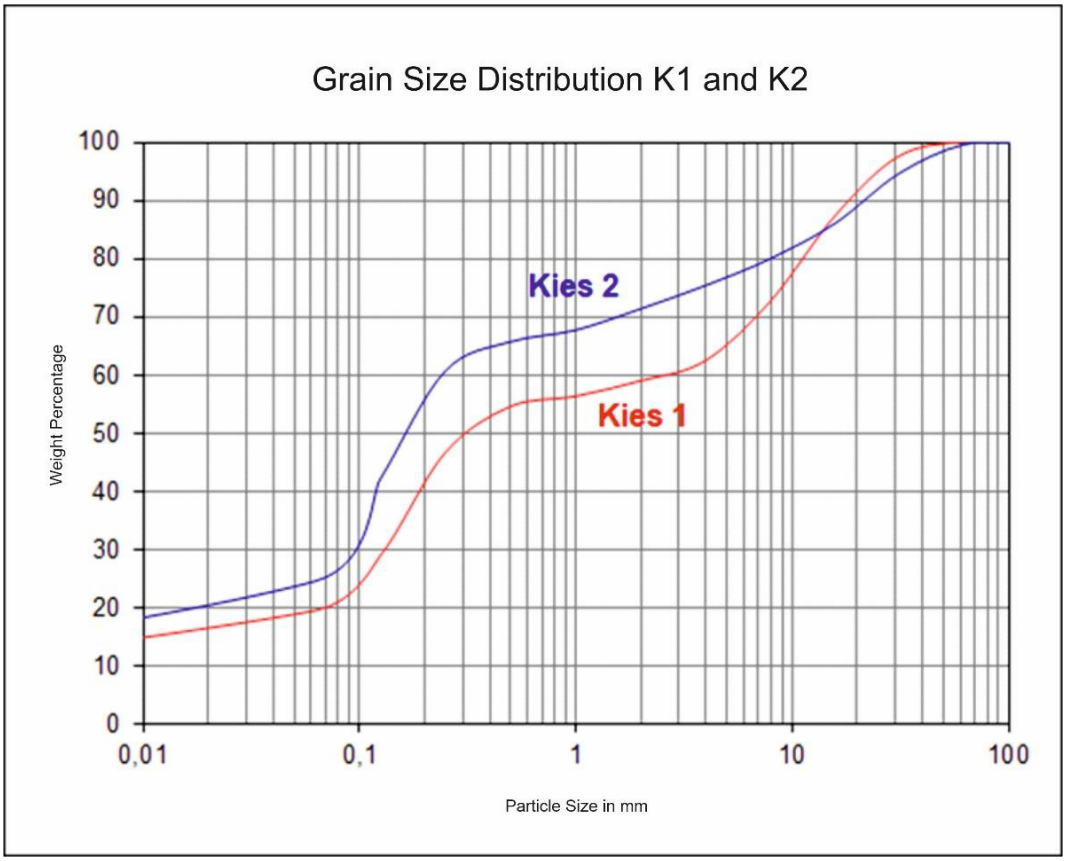

Fig. 31: Grain size distribution of K1 (red) and K2 (blue).

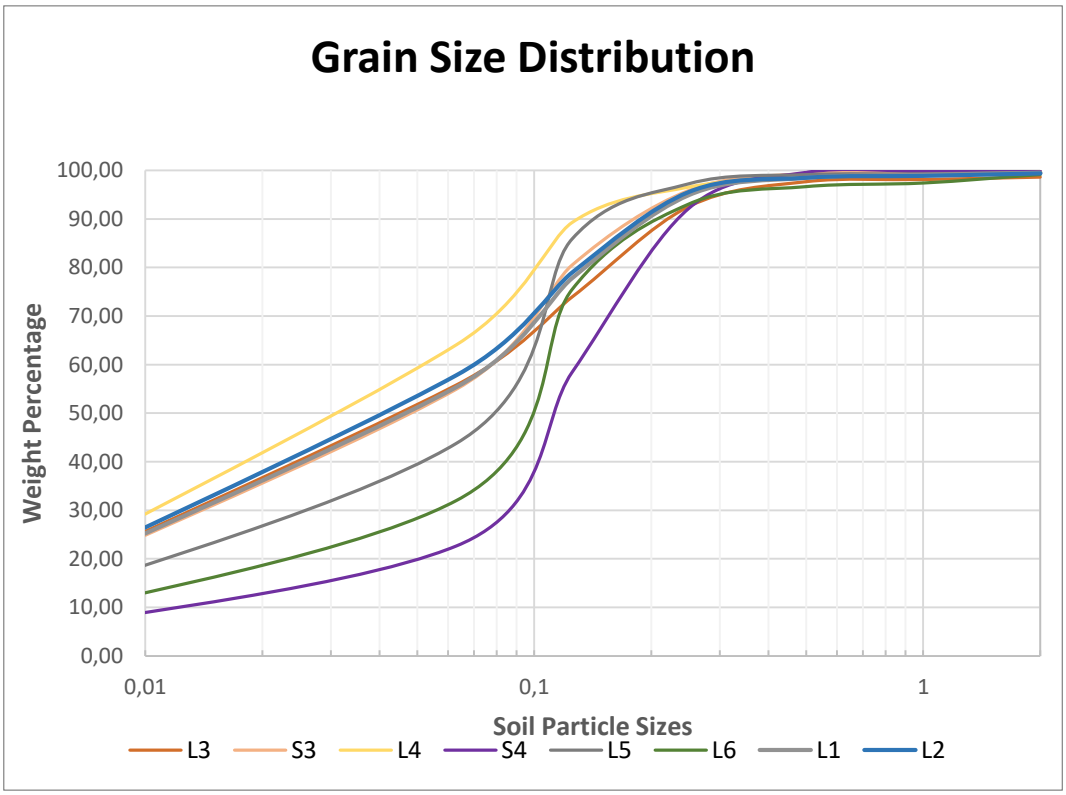

Fig. 32: Grain size distribution of L1 to L6 and S3 to S4 showing accumulation of particle sizes between 0.1 and 1 mm.

5.4 ^{14}C Dating

The gastropod samples analyzed by Beta Analytic Laboratory, using the ^{14}C method, provide valid calibrated ages between 31961 - 31370 BP and 14885 - 15150 BP (Table. A. 7). The bottom layer of the sand silt sequence (L1) directly above the gravel layers provides a conventional age of 20920 +/-70 BP. This age, however, is associated with some uncertainty because of the small mass of the datable gastropod shells and could not be calibrated.

The colluvial wedges C1 and C2 on the southern wall provide a mixed age between 31961 and 31370 cal BP which lie above the layer SK1 revealing an age between 31182 and 30946 cal BP on the southern trench wall and an age between 30437 and 30025 cal BP on the northern trench wall (Table. A. 7). The aforementioned ages belong to the stage of the MIS 2 placing it at the end of the Würm glaciation. The colluvial wedges together with the gravels K1 and K2 overlie the deposits of the fluvial terrace recorded in boreholes KB 05, KB 06, 5185 and 5189 (Fig. 5). K1 and K2 are the oldest sediments in the trench. K2 provides an age between 31148 - 30733 cal BP. These sediments are overlain by loess (L2) yielding an age between 23132 and 22926 cal BP which lies also in the MIS 2 stage and puts it at the end of the Würm glaciation.

A time gap of approximately 7000 years between L2 and L3A indicates no sediment deposition.

The sand and loess sequence which follows provide ages for L3A between 15655 and 15337 cal BP, for L4A between 16255 - 15933 cal BP, for L4B between 15150-14885 cal BP and for L5 between 15150 and 14885 cal BP (Table. A. 7). However, ages in L3A and B, L4A and L5 are associated with uncertainty because of the heavy bioturbation in this layer which transported and mixed sediments from different layers.

At the termination of the glacial period loess and sand layers (L3A to L5) of MIS 1 (Holocene) are deposited.

The pock shaped calcite crusts from the sand and gravel layers were also analyzed using the ^{14}C method. However, due to the long-time process of the calcite build-up an age between 44189 and 42751 cal BP was provided. Therefore, the calcite crusts were not suitable for dating and cannot be used in a time-stratigraphical-framework.

6 Discussion and Interpretation

6.1 Borehole profiles and geophysical measurements

Based on the results from the boreholes in profile G1, in the eastern part, between borehole 5189 and KB05, a basal unconformity of the Quaternary gravel with a dip to the west can be observed contrary to the eastward flow direction of the Danube. This indicates, that the sediments must have been tilted after their deposition. The Quaternary thickness reaches 26 meters at this point. This geometry can also be observed in the ERT GDP 102, in the long ERT and in the 2D seismic and can be interpreted as a down thrown block of the Quaternary deposits on the hanging wall (Fig. 13). The ERT and seismic measurements indicates an offset in the Quaternary deposits of about 10 to 20 m. In profile G2, an increase in Quaternary thickness to the east can also be observed, indicating fault activity. In profile G4 due to the lack of borehole data and in the area of question (between boreholes 43 and 50), the basal unconformity cannot be mapped accurately. However, an increase in Quaternary thickness of at least 6 m between these two boreholes is evident. The base of the Quaternary sediments drops from about 169 m (west) at 2700 m to below 150 m (east) at 2300 m, indicating a fault offset of about 15-20 m (Fig. 16). The inferred fault is interpreted as the southern continuation of the fault trenched in the Paleoseismological trench GER01.

To locate the position of the fault, GDP 102 (Fig. 17) was the most promising of the four shorter ERT measurements. It shows a depression of the Quaternary gravel base (shown in red) from 120 m onward.

In GDP 102, the fault was interpreted to be between 120 and 140 m in the ERT measurement GDP 102, shown as dashed line in Fig. 17. These observations correlate with the interpreted Quaternary gravel base from the borehole data in profile G1 (Fig. 13), as GDP 102 is situated between 2300 and 2500 meters in Profile G1. This depression can also be seen on the long ERT measurement at the same location (Fig. 18). The dip of the basal unconformity investigated in the borehole profile G1 shows the same geometry at the same location as the ERT measurement. The borehole data and the geophysical data combined show a sharp offset of the Quaternary base at the trench location and also a basal Quaternary unconformity dipping to the east against the flow direction of the Danube. This indicates, the offset results from tectonic subsidence after the gravel accumulation of the GDT.

6.2 Lithology and grain size distribution analysis

Both gravel layers, K1 and K2, show polymodal grain size distributions with about 40-50% silt and fine-grained sand and 30-40% gravel. The gravel of K1 and K2 were deposited by the Danube which built the Pleistocene Gänserndorf Terrace. The gravels of K1 were reworked together with originally overlying fine-grained sediments by periglacial processes such as frost creep or solifluction, and cryoturbation as indicated by fine-grained sediment lenses which are mixed into the gravel layer (Fig. 33b) and

terrestrial gastropod shells contained in the fine-grained matrix. Elongated pebbles in this layer are preferably oriented E-W. However, the E-W orientation of the trench could bias orientation data in favor of an E-W oriented pebbles. The calcite encrustations of some pebbles show lamination. The layered structure indicates a multiphase growth over a long period of time due to precipitation of calcite in the upper soil which encloses in some samples small quartz grains.

The gravels of K1 show sand pockets as well as an uneven contact between layers K1 and K2. This indicates cryoturbation during the last glacial period, which was also observed for the gravels of K2. A large ice wedge cast, at running meter 12, can be observed on the northern wall, indicating another sign of periglacial processes. The deposits of K2 are bulged down in the gravels of K1 as well as sand and silt which are mixed into layer K1 (Fig. 33a, Fig. 33b and Fig. 33c). Therefore, both gravel layers (K1 and K2) can be interpreted as strongly deformed by periglacial processes during the last glaciation in the Würm seen by the ice cast wedges and cryoturbation. The sum of the process led to the missing of fluvial gravels and previously overlying fine-grained sediment including loess as indicated by the occurrence of terrestrial gastropods.

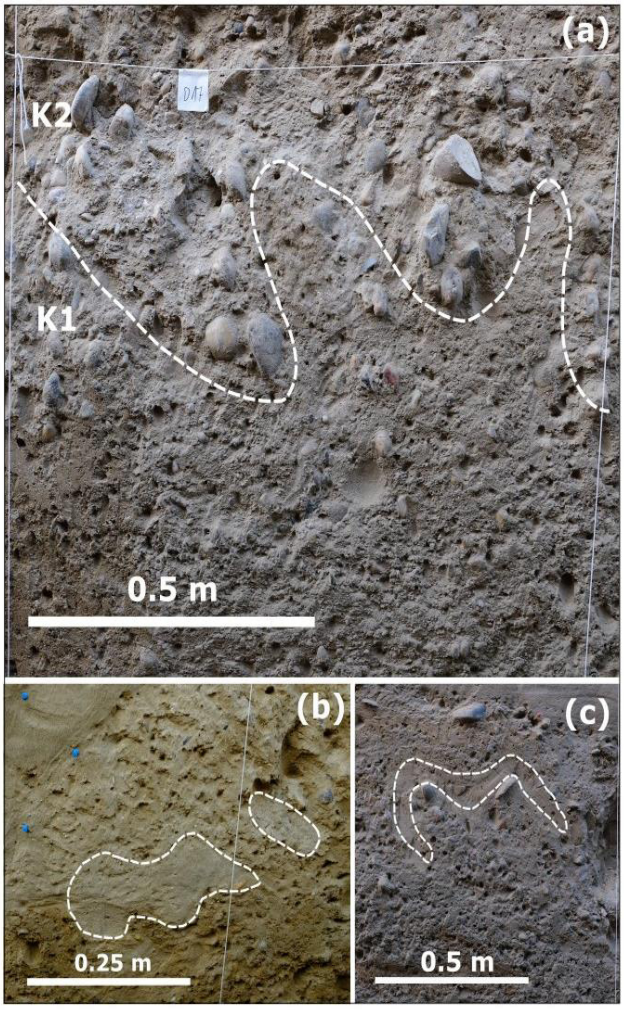

Fig. 33: Cryoturbation signs on the northern trench wall. a) uneven contact between layers K1 and K2. b) and c), sand pockets in layer K1.

The medium grained sand layer SK1 can be followed as a separate, but inconsistent horizon separating the gravel layers K1 and K2 and the loess layers throughout the trench. The layer can be interpreted as a wash facies horizon which was eroded down from the top of the scarp by rainsplash, slopewash and creep processes (McCalpin 2009).

The colluvial wedges (C1, C2 and C3) which are only found in the central part of the trench adjacent to faults that set off the sedimentary succession are a clear indicator for seismic events. The tension fissure adjacent to fault F1 separates the fault from C1 proving that C1 and C2 result from distinct depositional events (Fig. 24) (see following paragraph for deformation history). The layers L1A and L1B apparently fill a pre-existing relief. Gastropod fragments were found in the layer indicating this fine to medium grained layer is a terrestrial deposit (Fig. 10e).

Throughout the following loess sequence (L1 to L6) gastropod shells could be found indicating terrestrial soil formation and dry conditions. However, the distribution of L2 is completely absent on the western section. The rhizolithes in L2, which are calcium carbonate surrounded roots, indicate arid and semi-arid conditions and early soil (chernozem) formation (Durand 2010).

Due to the small sample size it was not possible to retrieve sufficient material for a grain size distribution analysis for S1 and S2. However, the comparison to S4, shows similarities in the grain sizes which leads to the conclusion that the layers might be wind transported sand or sand loess which are very common sediments of Quaternary glacial periods in Europe (Haase 2007). The aeolian sands are local outblows from the fluvial deposits of the paleo Danube (Sebe et al. 2015).

Loess layer L3 shows in some parts of this layer (mostly on the eastern side of the northern wall) darker spots which presumably are a sign of “pseudovergleyung” due to precipitation or waterlogging above ground frost (Peticzka and Weissl, pers. Comm., Olson 1988).

The thickness and accumulation of grain sizes between 0.063 mm and 0.5 mm in its grain size distribution indicates S4 being wind transported sand. Wind-blown sand shows a grain size maximum of <0.2 to 0.6 mm (Fig. 32) (Amelung et al. 2018, chapter 2).

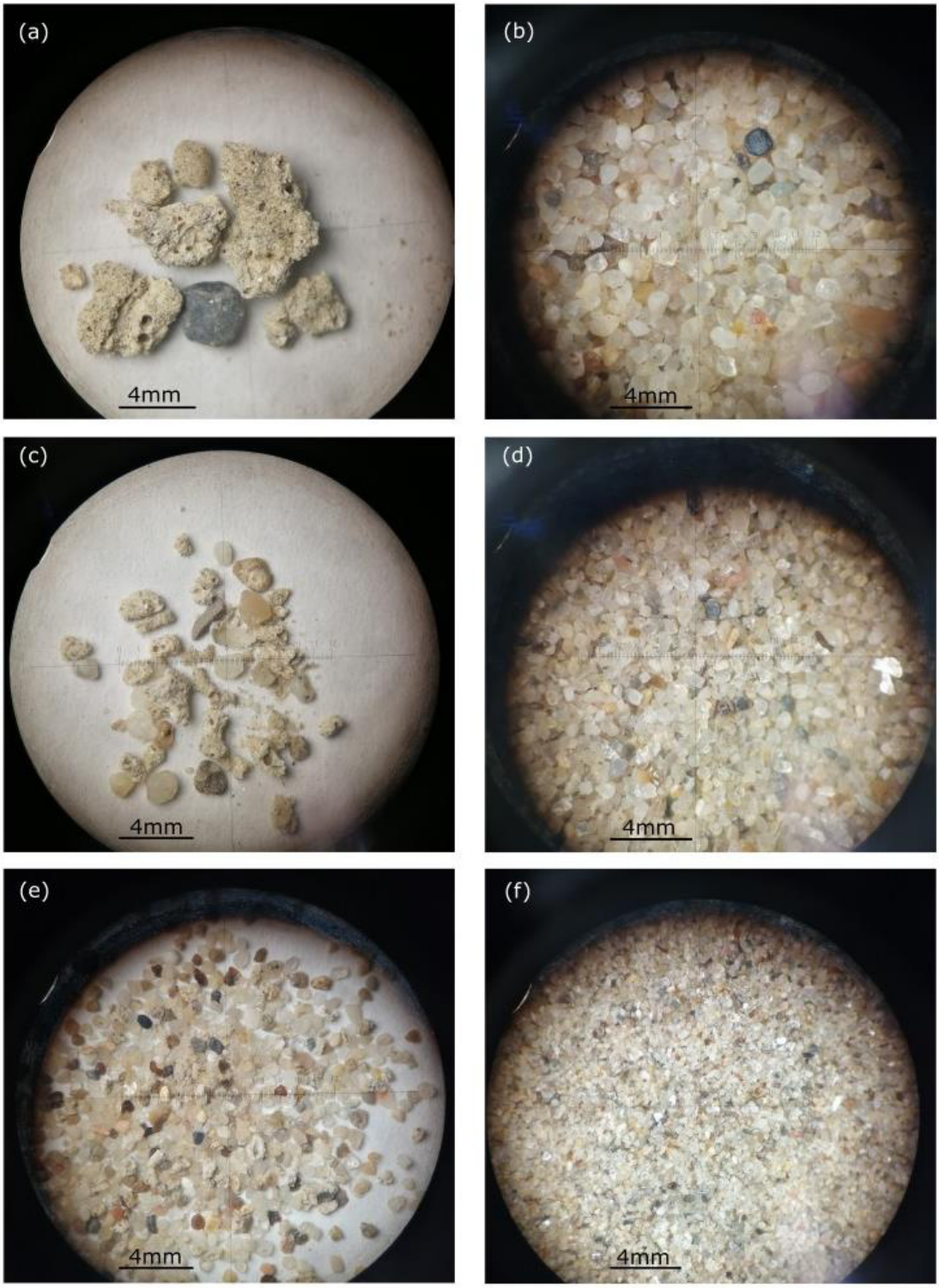

Fig. 34: Sediment samples of S4 under reflected light. a) <2 mm; b) <1 mm; c) <0.5 mm; d) <0.25 mm; e) <0.125 mm; f) <0.063°mm

The layer L5 is strongly overprinted by bioturbation which is shown by darker spots of sediments from L6 that were dug down into the layer by small mammals. On the southern side a two meters wide depression which is presumed to be a fox den could be observed.

This is the largest feature of bioturbation in the trench (Fig. 28). Some smaller mammal burrows also can be observed on both trench walls in L5 and L6.

The top soil (chernozem) layer L6 can easily be recognized by its very dark brown color.

The grain size distribution curves from the gravel, loess and sand samples show similarities in their particle sizes. Particle sizes accumulate in all samples between 0.1 and 1 mm indicating that loess and sand, which lie on top of the gravel layer were mixed into the gravel by cryoturbation processes and therefore showing similar grain size distribution curves (Fig. 31 and Fig. 32).

6.3 Deformation history

The trench exposes several faults (F1-F9) which belong to the Seyring Fault System. Offset sediments were visible in the middle part of the trench both at the northern and the southern wall in the layers K1 to L3 (Fig. 35).

Layers K1 and K2 are offset by faults F1, which dips to the east, and F2, which dips to the west. F1 and F2 produce an offset resulting in the gravels of the eastern side of the trench (footwall) lying approximately 20 cm lower relative to the gravels on the western side of the wall (hanging wall).

Faults F1 and F2 formed an approximately 70 cm deep relief (Graben structure) that was later filled up by sediments of C1 to C3, SK1 and L1A to L2. L1A and L1B are later offset by a new Fault F3 which branches off from F2 and sets off this sediment layer by a few millimeters (Fig. 35).

L2 which is only visible on the downthrown block laps on the scarp face and pinches out towards the east. Later L2 is affected by a new west dipping fault F4 that branches off from F1. F4 produces a small-scale graben structure within L2.

Following the F4 event, a newly formed west dipping fault (F5) breaches through K1, SK1 and C3 and sets off L2 and S2 by a few centimeters. A newly formed west dipping fault (F6) offsets layers L1B, L2, S2, L3 and S3 by a few centimeters. However, faults F5 and F6 are not visible in the layers underlying the loess and sand sequence due to the grain size of the gravels and its low offset. (Fig. 35)

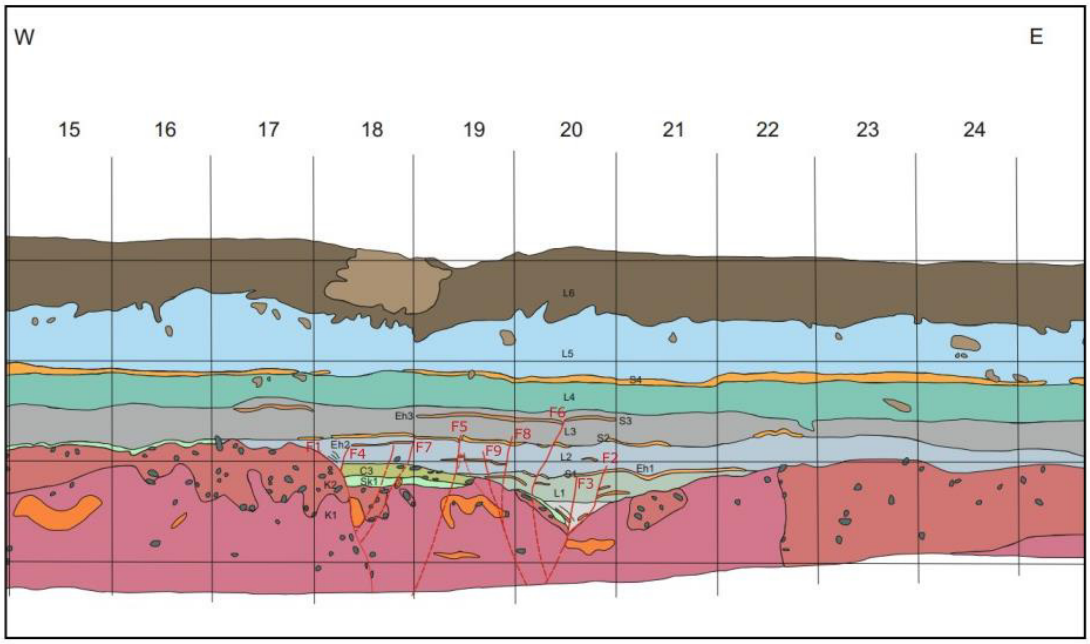

Fig. 35: Sector of faulted area on the northern trench wall. Faults F1 to F9 (red) with interpreted course (dashed red line). Event horizons Eh1 to Eh3. Gravel layers K1 and K2 (pink and red). Loess sequence L1 to L6 (grey, blue and brown). Sand sequence S1 to S4 (orange).

On the middle part of the northern wall six events (E1 to E6) could be determined that offset layers of gravel, loess and sand.

Events "E1 to E3":

On the southern and northern trench wall two main faults, F1 and F2, are observed, which cut through the gravel layers K1 and K2.

The fault F1, exposed on both trench walls, dips towards the east (094/76) on the northern wall face and on the southern wall face respectively (094/53). F2 dips towards the west (273/79) on the northern wall face as well as on the southern wall (264/56). The dip direction of F1 corresponds to the orientation of the SFS as seen in the seismic profile (Fig. 7). The antithetic fault F2 cuts through the gravel layers. Generally, all observed faults within the trench show a steep dip (Fig. 36).

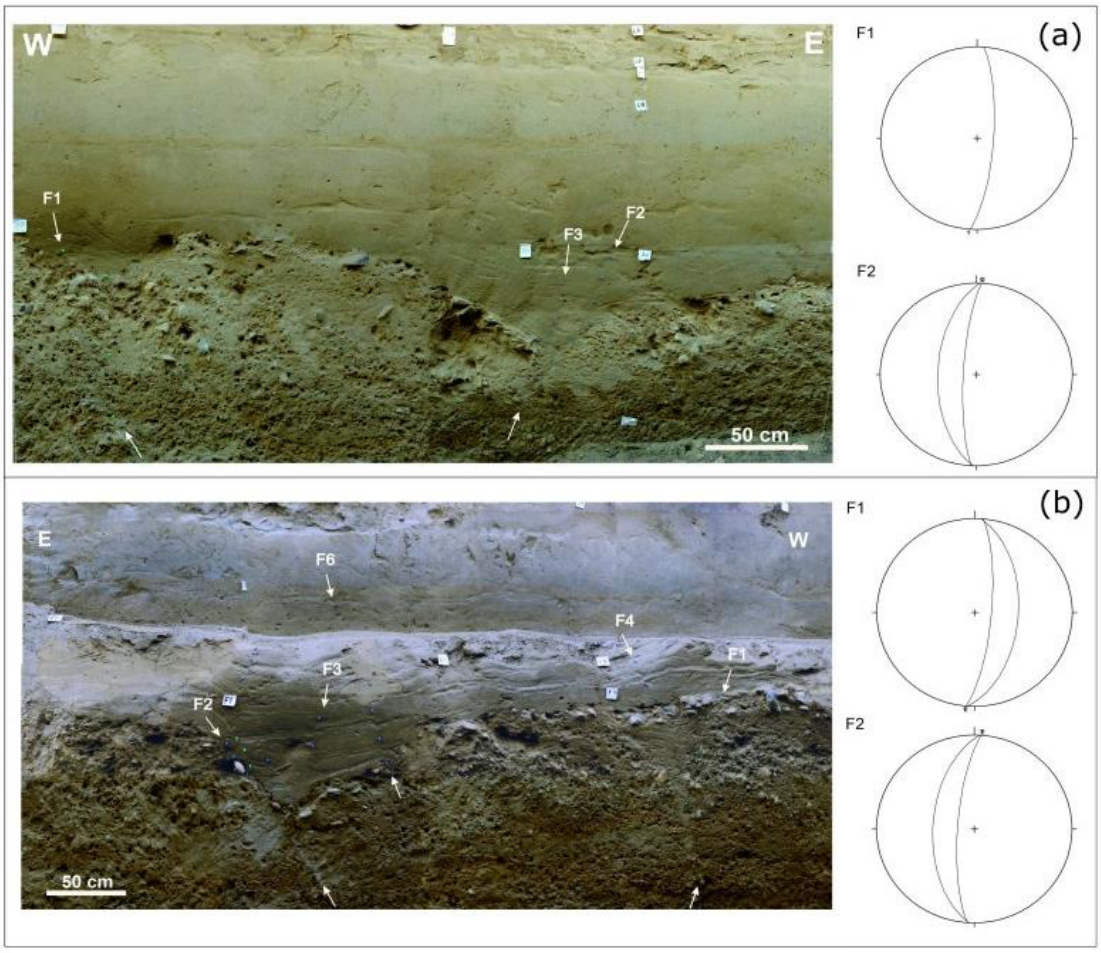

Fig. 36: North (a) and south wall (b) of trench with faults and stereoplots of normal faults F1 and F2.

On the southern wall two colluvial wedges (C1 and C2), which are not visible on the northern trench wall, were observed. C2 is in direct contact with fault F1 indicating its formation at a free face of a fault scarp formed by displacement along F1 (Fig. 37, Events 1 and 2). Although lithologically similar, the two colluvial wedges are clearly distinguished by a tensile fissure that formed between the fault plane F1 and C1, and which is filled with material consisting of fine gravel and coarse sand. The fissure fill is overlain by laminated pebbly sand of C2 (Fig. 24). The succession is related to two earthquakes triggered by the fault F1 which formed a fault scarp with a free face (C1) and a free face with a tension fissure (C2). After the development of the fault scarp loose material exposed on the scarp and the uplifted block was washed to the base of the scarp and created the wedge-shaped deposits (C1, C2).

C1 and C2 show a thickness of about 7 cm (C1) and 8 cm (C2). After McCalpin (2009) we can indirectly reconstruct the height of the free face of the fault scarp resulting from displacements along F1 from the height of the colluvial wedges which are assumed to be half of the scarp height. Resulting in a scarp height of 14 cm for event “E1” and about 16 cm and for event “E2”. The low volume of sediment of C1 and C2 did not allow for separate sampling of terrestrial gastropods. The ^{14}C age from the colluvial wedges C1 and C2 revealed a mixed age between 31961 - 31370 cal BP, indicating event “E1” and

“E2” being younger than 27 kyr and older than L1, yielding an conventional age of about 20 kyr (Table. A. 7).

On the northern trench wall faulting produced a half graben and fault rollover. The half graben is located between F1 and F2, while the fault rollover lies adjacent to the listric fault F2. A Rollover tilted the top of K2, SK1 and L1A for about 25°. The E-dipping sediments are overlain by horizontally laminated sand of L1B (Fig. 35). The maximum thickness of the fault rollover is 23 cm. Neither L1A and L1B could be dated. Therefore, and due to the lack of observation of the stratigraphic relation between C1 to C3 and L1A, the rollover event could not be aligned with the other tectonic events observed in the trench.

Both trench walls expose the colluvial wedge C3 lying against fault F1 (Fig. 37, Event 3). The wedge buries the lower part of the former free face of the fault scarp. C3 has a maximum thickness of 20 cm. It is traced to a maximum distance of about 1.5 m from F1 and displays a fining of sediments with increasing distance from the fault towards the east. Imbricated pebbles suggest aquatic transport from the footwall to the hanging wall of F1. In the northern wall a sediment filled the graben between F1 and a small antithetic fault separates the upper part of C3 from F1 indicating a younger reactivation of F1 (see event E5 below). The thickness of C3 of 20 cm and 16 cm on the northern and southern wall, respectively, indicate an initial scarp height in the order of 30-40 cm.

This interpretation is in line with the observed offset of sand gravel horizon SK1, which forms a marker horizon that is offset for about 40 cm at F1. This offset is regarded to the total offset at F1 during the Events E1 to E3 (Fig. 35).

Following events “E1 to E3” loess (L1A) with a thickness of 32 cm was deposited and filled the rollover at fault F2 and the adjacent depression of the top of K1 and K2. The loess layer L1 shows a conventional age of 20920+/- 110 BP. On top of the loess layer (L1B), a 4 cm thick sand layer (S1) formed. This sand layer is only visible in the fault area (Fig. 37b).

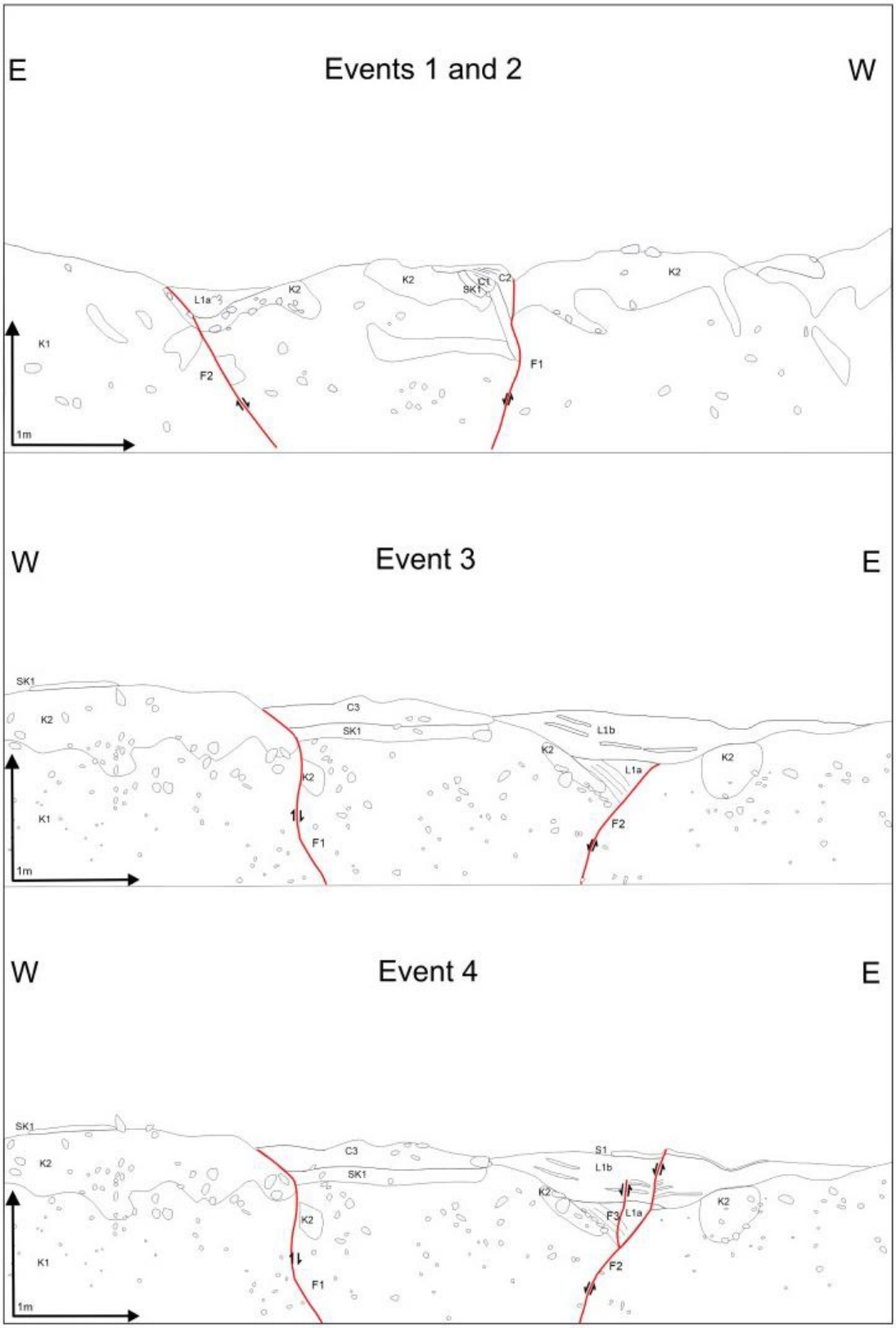

Fig. 37: Events 1 and 2 only visible on the southern trench wall. Event 3 on the northern trench wall and event 4; observed faults in red.

Event “E4”:

After the sedimentation of L1A and S1 event E4 reactivated fault F2 by renewed faulting and formed fault F3 that cuts through the rollover adjacent to fault F2 and the overlying loess L1B. F2 offsets several minor sand layers within L1B and the overlying S1 by 3 cm (Fig. 37, Event 4). On the southern trench wall the fault F3 is also visible although an offset cannot be determined.

The age of L1, though questionable because of the low mass of dateable material, yields a conventional age of 20920 +/-70 BP. Event “E4” is therefore younger than 20.92 kyr but older then the loess layer L2 which yields a calibrated age between 23132-22926 BP.

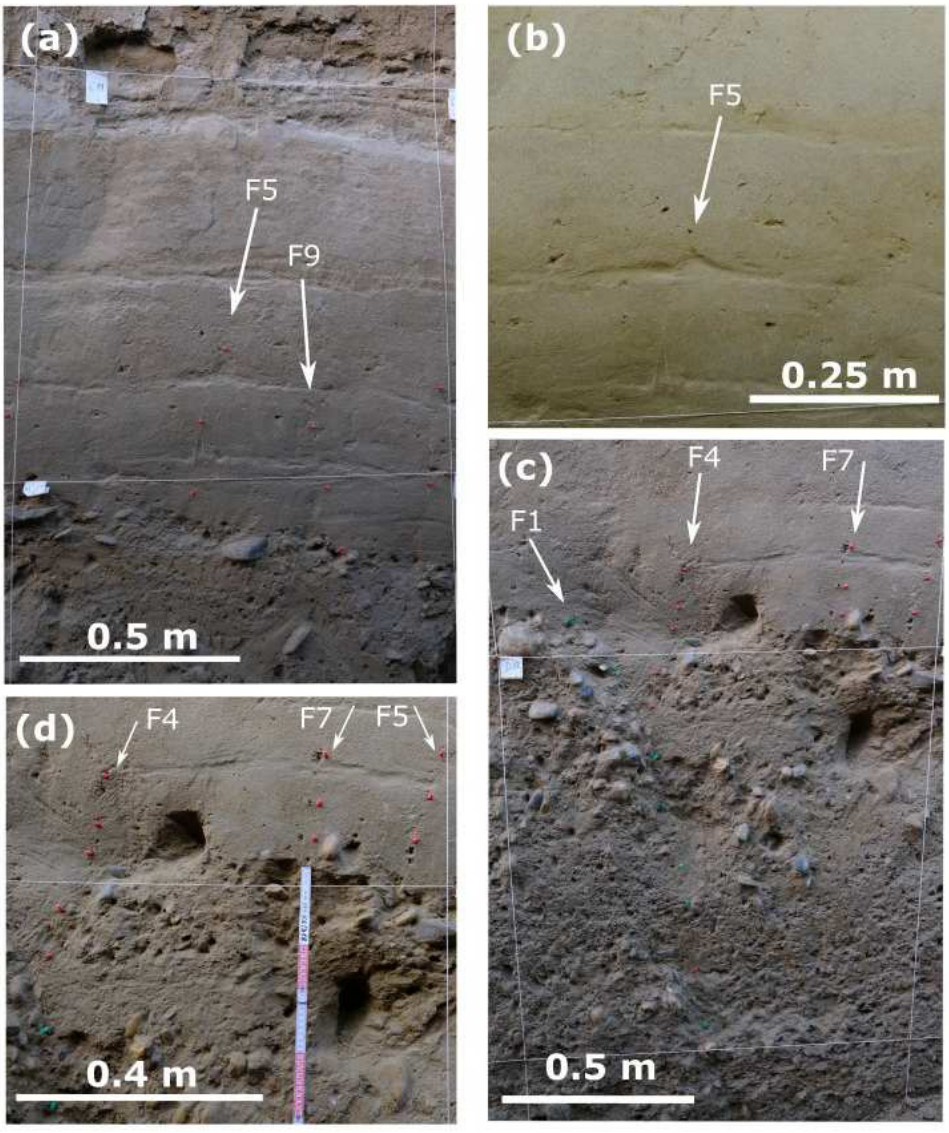

Fig. 38: Fault related offset of sand layers. a) faults F5 and F9 (red pins) breaching through sand and loess layers. b) inset figure of F5 offsetting a sand layer. c) offset of gravel layers by F1 (green pins). F4 (red pins) forming a small-scale graben structure and F7 (red pins) offsetting a sand layer. d) faults F4, F5 and F7 (red pins).

Event "E5":

After the sedimentation of L2 and S2 a new fault F5 formed that offsets the sand layer S2 by 6 cm (Fig. 40, Event 5). This fault is not visible in the gravel layers K1 and K2 beneath the loess and sand layers probably due to its low offset and the grain size of the gravel. A small antithetic fault F4 branches off from the top part of F1 forming a small-scale graben structure between F1 and C3 which is well depicted by the offset lamination of loess layer L2 (Fig. 38c and d). On the southern trench wall two faults (F6, F10) offset the sand layer S2 by 2 cm. (Fig. 39) All faults terminate upwards at an event horizon near to the top of S2. Another Fault (F7) branches off from F5 and new faults F8 and F9 breach through the gravel and loess layers (Fig. 38a and b).The upward termination of faults F4 and F5 at or close to sand layer S2 defines an event horizon (Fig. 38a and b) which is dated by the ages derived from L2 and L3 that was deposited on top of the sand layer S2. L3 revealed ages between 15655-15337 cal BP for L3A and 15766-15485 cal BP for L3B, respectively. Event "E5" therefore post-dates L2 with an age between 23132-22926 cal BP and pre-dates L3A with 15655-15337 cal BP (Table. A. 7).

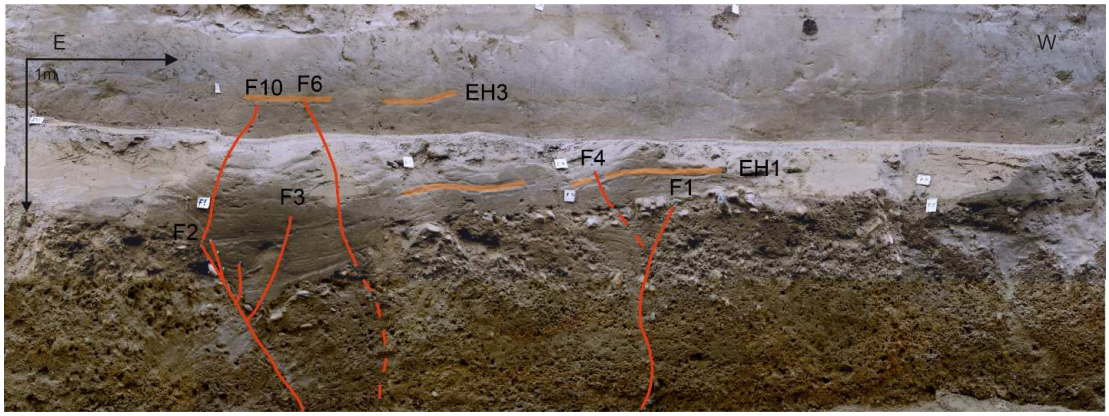

Fig. 39: South wall of trench with faults (red lines) and interpreted course of faults in red dashed lines.

Event "E6":

The youngest event, only visible on the northern trench wall, occurred after the sedimentation of L3 and the overlying sand layer S3.

A newly formed W-dipping normal fault (F6) displaces the sand layer S3 by 3 cm. S3 is the stratigraphically highest deformed horizon in the trench (Fig. 40, Event 6). Again, the fault F6 is not visible in the gravel layers K1 and K2 probably due to the difficulty of recognizing deformation bands with low-offset in coarse-grained sediment. The age of F6 is older than the loess L4A that revealed a calibrated age between 16255-15933 BP and L4B revealing a calibrated age between 15240-14989 BP and is younger than the layer L3A that shows a calibrated age of 15655-15337 BP (Table. A. 7). However, these sediments might be mixed up by bioturbation and redeposition of gastropod shells that have been found in this layers and might therefore reveal mixed up ages.

After the last earthquake event took place, a sequence of loess (L4), wind-blown sand (S4) and loess (L5) were deposited before finally soil (L6) formed on top (Fig. 35).

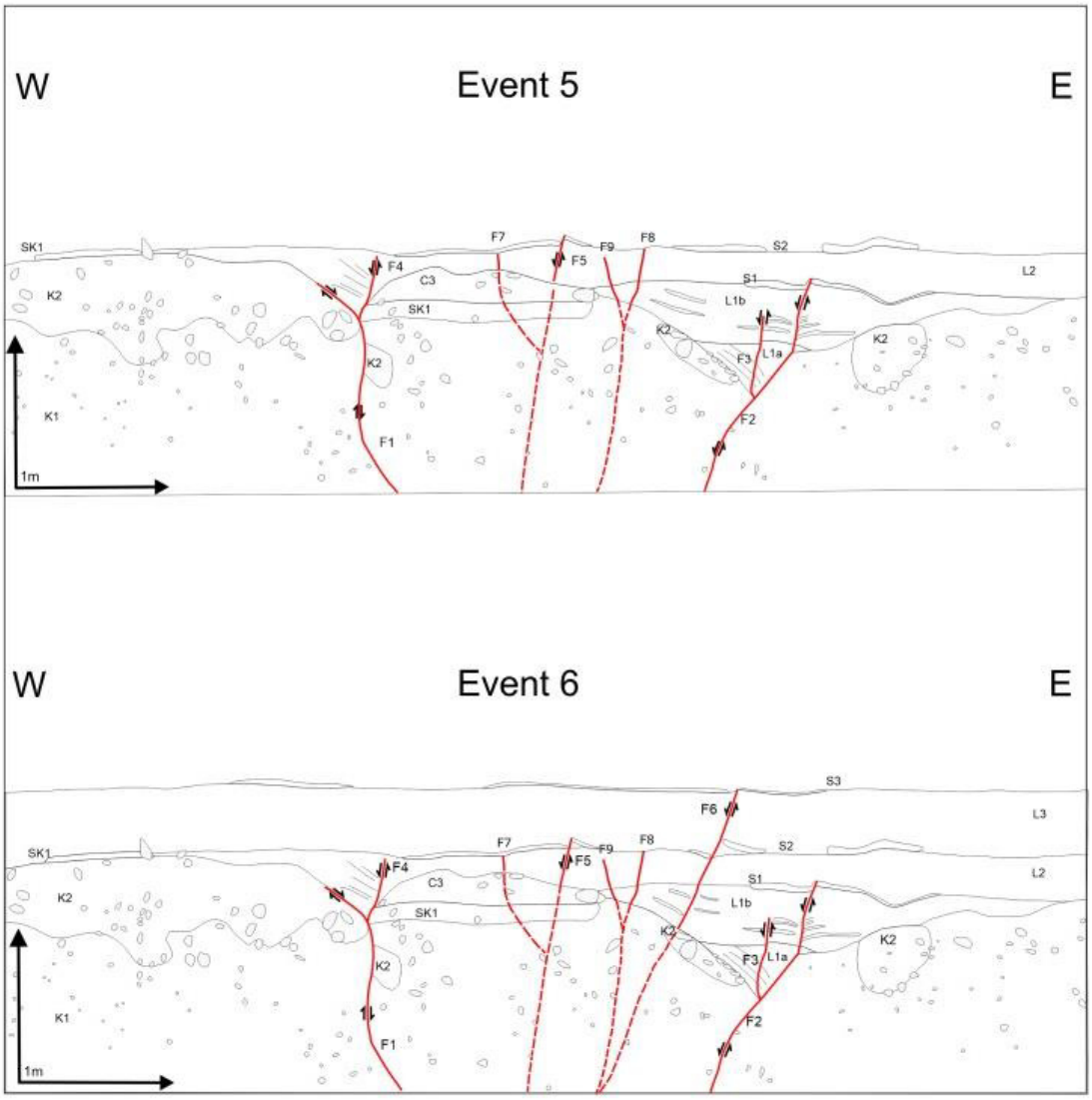

Fig. 40: Event 5 and Event 6 on the northern trench wall with observed faults in red and interpreted course in red dashed line.

The maximum vertical offset observed in the trench is around 0.4 m, derived from the colluvial wedge of C3 on the northern side of the trench wall. Whereas, the vertical offset derived from C3 on the southern trench wall was 32 cm. Using the maximum calibrated average age of 31961 kyr obtained from ^{14}C dating for events E1 and E2 this would lead to a maximum slip rate of 0.01 mm/a for the Seyring Fault Segment. However, this is a rough estimation of deformation rates. The offset from The total height difference of the gravel top on the hanging wall compared to the gravel top on the footwall is approximately 30 cm and the height difference of the marker horizon SK1 on the hanging wall lies 40 cm higher than on the footwall. These observations are very well in line with the scarp height of about 40 cm derived from the colluvial wedge C3 and the calculated average slip-rate.

The magnitudes of the events E4 to E6 causing offsets of 3 to 6 cm, as well as the magnitudes of the colluvial wedges C1 and C2 (E1 and E2) can only be estimated. However, experience shows, that faults with maximum offsets between 1 and about 20 cm are produced by earthquakes with magnitudes between M=5 and M=6, as the

threshold for surface displacement is around intensity I ≈ VIII (M=5 to 5.5) (Michetti A.M. et al. 2005, McCulpin 2009).

The magnitude of the earthquake which produced the largest displacement (0.4 m) is derived from the colluvial wedge thickness of C3 observed on the northern trench wall and is evaluated with about M=6.4 using the empirical relation between maximum surface offset and magnitude of Wells and Coppersmith (1994). On the southern trench wall, the same colluvial wedge with a height of 0.32 m indicates a magnitude of about M=6.3. Both values compare well with the observed 40 cm offset of the gravel top. These results are in line with several other studies shown in Bonilla et al. (1984) who compared displacements with magnitudes, claiming a M=6.57 earthquake in Bulgaria in 1928 produced a displacement of 40 cm or a M=6.34 earthquake in the U.S. in 1954 produced a displacement of about 30 cm.

6.4 Recurrence intervals for earthquakes at the Seyring Fault System

In sum, Paleoseismological results from the trench GER01 revealed six ground-breaking fault slip events (“E1” to “E6”), including three events (“E1” to “E3”) for which ground cracks and colluvial wedge formation prove seismic slip. These six events took place within some 15 kyr, with the oldest events “E1 and E2” showing a maximum age of 31961 cal BP and the youngest event “E6” showing an age between 15766 yr and 14989 yr cal BP. This active time is followed by an inactive stage of some 14 kyr where loess and sand layers deposited without deformation. This indicates a clustered behavior for earthquakes along the Seyring Fault System as observed at the Markgrafneusiedl fault 15 km east of Vienna by Hintersberger et al. (2018). They suggest, that earthquakes along the MF with a magnitude M ≥ 6.5 cluster in two time intervals within the last 120 kyr. Also, they presume that the MF is between clusters at the moment with the next calculative cluster occurring in approximately 10 kyr. Comparing this interpretation to the Seyring Fault Segment, which produced six events within some 15 kyr followed by some 14 kyr of quiescence, that leads also to the presumption that slip of the SFS also occurs in clusters. However, the age of the event clusters at the SFS does not match the events observed at the MF (Table 1).

Markgrafneusiedl Fault		**Seyring Fault**		
Event no.	mean Occurence time	Event no.	maximum age [cal BP]	minimum age [cal BP]
E5b	109 +/- 3 kyr	E1 and E2	31.96 kyr	31.37 kyr
E4b	106 +/- 3kyr	E3	31.37 kyr	22.93 kyr
E3	43.3 +/- 4.9 kyr	E4	22.93 kyr	20.92 +/-70 kyr (conventional age)
E2	37.1 +/- 4.9 kyr	E5	23.13 kyr	15.34 kyr
		E6	15.66 kyr	14.99 kyr

Table 1: Earthquake events and their occurrence time of the Markgrafneusiedl Fault (Hintersbergeret al. 2018) and the branch fault of the Seyring Fault System.

7 Conclusion

The Pleistocene Gänserndorf Terrace in the central Vienna Basin, formed by the fluvial plain of the Danube, is dissected into several parts by the Aderklaa-Bockfließ Fault and the Markgrafneusiedl Fault. On the western margin, the Seyring Fault separates the Gänserndorf Terrace from the Terrace West of Seyring. In this study seismic profiles, electrical resistivity tomography (ERT) data and borehole data were used to locate a segment of the Seyring Fault. This segment was further investigated by trenching. The lithological sequence in the trench is heavily influenced by cryoturbation processes of the last glacial period (Würm; MIS 2) as well as bioturbation processes of small mammals visible in the top layers. Typical glacial deposits as wind-blown sand and loess alternate on top of the gravel deposits of the High Terrace.

Although the Vienna Basin is considered to be of moderate seismicity, observations in the trench show that the Quaternary sediments are affected by faulting (maximum offset of 40 cm) (Fig. 41). Several offsets in the gravel, sand and loess layers as well as three colluvial wedges, with the largest height of 0.2 m (colluvial wedge thickness) were observed. Assuming this event was tectonically triggered, a maximum slip rate for the Seyring Fault can be estimated, using the maximum ^{14}C age from the colluvial wedge of approximately between 31.96 and 31.37 kyr cal BP. The maximum slip rate for the trenched splay fault of the SFS is therefore about 0.01 mm/yr which is significantly lower than the slip rate of the MF with 0.02 – 0.05 mm/yr. The strongest paleoearthquake recorded in the trench GER01 of the SFS derived from the colluvial wedge thickness of C3 corresponds to a magnitude of M= 6.4. Trenching results also provide evidence of earthquakes with M<6 which are typically not recorded by Paleoseismological techniques.

In total six surface breaking events were observed in the trench. The oldest events" E1 and E2" show a maximum age of about 31.96 kyr and a minimum age of about 20.92 kyr and the youngest event "E6" showing an age between 15.66 kyr and 14.99 kyr (Table 2). This reveals, that after a tectonically active time of some 15 kyr a time of some 14 kyr of quiescence followed until today. A correlation between the surface breaking events of the Seyring Fault and the MF (Hintersberger et al. 2018) underlines the hypothesis of temporal earthquake clustering. While data from the MF suggest that the fault is between clusters at the moment, this cannot be stated for the SFS where the trenched sedimentary record is too short to assess time periods between possible clusters. It must be further noted that the Paleoseismological data produced by all splays of the SFS may therefore be higher than the number of earthquakes recorded in the trench.

We finally conclude, that due to the potential of the SFS to cause earthquakes with magnitudes M>6 and the closeness to the City of Vienna, the SFS poses significant hazards to this economic and social center.

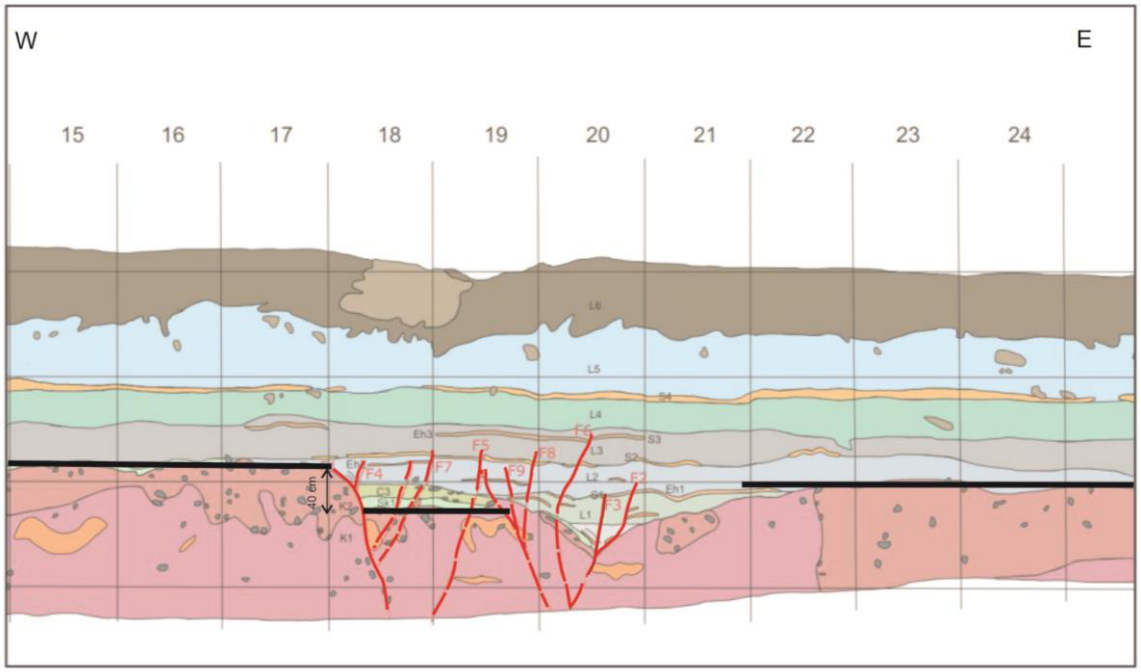

Fig. 41: Segment of northern trench wall with maximum offset of about 40 cm (black line). Faults (red lines), estimated faults (dashed red lines).

Event no.	evidence	Age [cal BP]		offset [cm]	estimated magnitude
		maximum age	minimum age		
E1	colluvial wedge	31961	31370	14	6.1
E2	colluvial wedge	31961	31370	16	6.1
E3	colluvial wedge	31370	22926	40	6.4
E4	event horizon	22926	20920 +/-70 BP (conventional age)	3	5.5
E5	event horizon	23132	15337	6	5.8
E6	event horizon	15655	14989	3	5.5

Table 2: Number of events with type of evidence, maximum and minimum calibrated ages. Offset in cm and estimated magnitudes.

References

Afry: 2D Reflexionsseismik 2020 Raasdorf und Gerasdorf.

ACORN: Catalogue of Earthquakes in the Region of the Alps – Western Carpathians Bohemian Massif for the period from 1267 to 2004, 2004. Computer File, Vienna (Central Institute for Meteorology and Geo-dynamics, Department of Geophysics) – Brno (Institute of Physics of the Earth, University Brno.

Amelung, Blume, H.-P., Fleige, H., Horn, R., Kandeler, E., Kögel-Knabner, I., Kretzschmar, R., Stahr, K., Wilke, B.-M., 2018. Scheffer/Schachtschabel Lehrbuch der Bodenkunde (17th ed. 2018.). Springer Berlin Heidelberg: Imprint: Springer Spektrum.

Bagnold, R.A., 1953. The physics of blown Sand and dessert dunes. London.

Beidinger, A. & Decker, K., 2011. 3D geometry and kinematics of the Lassee flower structure: Implications for segmentation and seismotectonics of the Vienna Basin strikeslip fault, Austria. Tectonophysics 499, 22-40.

Bagnold, R.A., 1953. The physics of blown Sand and dessert dunes. London.

Beidinger, A. & Decker, K., 2011. 3D geometry and kinematics of the Lassee flower structure: Implications for segmentation and seismotectonics of the Vienna Basin strikeslip fault, Austria. Tectonophysics 499, 22-40.

Beidinger, A., Decker, K., Roch, K.H., 2011. The Lassee segment of the Vienna Basin fault system as a potential source of the earthquake of Carnuntum in the fourth century A.D. International Journal of Earth Science 100, 1315–1329.

Bonilla, M.G., 1988. Minimum Earthquake Magnitude Associated with Coseismic Surface Faulting. Environmental & Engineering Geoscience, 25, 17-29.

Bonilla, M.G., Mark, R.K. and Lienkaemper, J.J., 1984. 'Statistical relations among earthquake magnitude, surface rupture length, and surface fault displacement', Open-file report (United States Geological Survey. 1978).

Braumann, S.M., et al., 2018. Challenges in constraining ages of fluvial terraces in the Vienna Basin (Austria) using combined isochron burial and pIRIR225 luminescence dating, Quaternary International.

Bus Z., Grenerczy G., Toth L., Monus P., 2009. Active crustal deformation in two sesimogenic zones of the Pannonian region– GPS versus seismological observations. Tectonophysics 474, 343–352.

Chwatal, W., Decker, K., Roch, K.H., 2005. Mapping of active capable faults by high resolution geophysical methods: examples from the central Vienna Basin. Austrian Journal of Earth Sciences 97, 52–59.

Decker, K., Gangl, G., Kandler, M., 2006. The earthquake of Carnuntum in the fourth century A.D. – archaeological results, seismologic scenario and seismotectonic implications for the Vienna Basin Fault, Austria. Journal of Seismology, 10, 479–495.

Decker, K., Peresson, H., 1998. Miocene to present-day tectonics of the Vienna Basin transform fault. In: Links between the Alps and the Carparthians, XVI Congress of the Carparthian-Balkan Geological Association, Geologische Bundesanstalt, Wien, pp. 33-36.

Decker, K., Peresson, H., Hinsch, R., 2005, Active tectonics and Quaternary basin formation along the Vienna Basin Transform fault. Quaternary Science Reviews 24, 305–320, Amsterdam.

Durand, N., Monger, C. H., Canti, M. G., 2010. Calcium Carbonate Features. In Interpretation of Micromorphological Features of Soils and Regoliths, 149–194.

Everett, Mark E., 2013. Near-Surface Applied Geophysics. Cambridge University Press.

Fink, J. & Majdan, H., 1954. Zur Gliederung der pleistozänen Terrassen des Wiener Raumes.Jahrbuch der Geologischen Bundesanstalt 97 (2), 211-249.

Fink, J., 1955. Das Marchfeld. In: Fink, J., Grill, R., Küpper, H. (Eds.), Beiträge zur Pleistozänforschung in Österreich, Verhandlungen der Geologischen Bundesanstalt. Sonderheft D, Wien, 88–116.

Fossen, H., 2010. Structural Geology. Cambridge: University Press.

Grill, R., 1968. Erläuterungen zur Geologischen Karte des nordöstlichen Weinviertels und zu Blatt Gänserndorf. Geologische Bundesanstalt, Wien, 155 pp.

Grill, R., Braumüller, E., Friedl, K., Götzinger, G., Janoschek, R., Küpper, H., 1954. Gänserndorf mit dem österreichischen Anteil des Blattes Marchegg – Geologische Spezialkarte der Republik Österreich 1:75.000. Geologische Bundesanstalt, Wien.

Haase, D., Fink, J., Haase, G., Ruske, R., Pécsi, M., Richter, H., Altermann, M. Jöger, K.D. 2007. Loess in Europe--its spatial distribution based on a European Loess Map, scale 1:2,500,000. Quaternary Science Reviews, 26, 1301-1312.

HADES: Bohrdatenbank des geologischen Dienstes, 2007. Amt der Niederösterreichischen Landesregierung, Computerfile, St. Pölten.

Hammerl, Ch., Lenhardt, W.A., 2013. Erdbeben in Niederösterreich von 1000 bis 2009 n. Chr. Abhandlungen der Geologische Bundesanstalt, 67, 3-297.

Harzhauser, M., Daxner-Höck, G., Piller, W.E., 2004. An integrated stratigraphy of the Pannonian Late Miocene in the Vienna Basin. Austrian Journal of Earth Sciences, 9596, 6–19.

Harzhauser, M., Kovar-Eder, J., Nehyba, S., Ströbitzer- Hermann, M., Schwarz, J., Wójcicki, J. and Zorn, I., 2003. An Early Pannonian (Late Miocene) transgression in the Northern Vienna Basin. The paleoecological feedback. Geologica Carpathica, 54, 41-52.

Harzhauser, M., Kranner, M., Mandic, O., Strauss, P., Siedl, W., Piller, W. E., 2020. Miocene lithostratigraphy of the northern and central Vienna Basin (Austria). Austrian Journal of Earth Sciences, 113, 169–199.

Hinsch, R., Decker K., Peresson, H., 2005b. 3-D seismic interpretation and structural modeling in the Vienna Basin: implications for Miocene to recent kinematics. Austrian Journal of Earth Sciences 97, 38–50.

Hinsch, R., Decker, K., Wagreich, M., 2005a. 3-D mapping of segmented active faults in the southern Vienna Basin. Quaternary Sciences 100, 1925-1935.

Hinsch, R., Decker, K., 2011. Seismic slip rates, potential subsurface rupture areas and seismic potential of the Vienna Basin transfer fault. International Journal of Earth Sciences: Geologische Rundschau 100(8), 1925-1935.

Hintersberger, E., 2019. Mögliche geologische Evidenz zum Carnuntiner Erdbeben. In: Das Carnuntiner Erdbeben im Kontext, Amt der Niederösterreichischen Landesregierung, 143.

Hintersberger, E., Decker, K., Lomax, J., Luethgens, C., 2018. Implications frompalaeoseismological investigations at the Markgrafneusiedl Fault (Vienna Basin, Austria) for seismic hazard assessment. Natural Hazards and Earth System Sciences, 18.2, 531–553.

Hoelzel, M., Decker, K., Zamolyi, A., Strauss, P., Wagreich, M., 2010. Lower Miocene structural evolution of the central Vienna Basin (Austria). Marine and Petroleum Geology, 27, 666–681.

Kandler, M., 1989. Eine Erdbebenkatastrophe in Carnuntum? Acta Archaeol Acad Sci Hung 41:313-336. Akademia Kiado, Budapest.

Krézsek, C., Adam, J., and Grujic, D.: Mechanics of fault and expulsion rollover systems developed on passive margins detached on salt: insights from analogue modelling and optical strain monitoring, Geol. Soc. Lond., Spec. Pub., 292, 103–121.

Kröll, A., Gnojek, I., Heinz, H., Jiřiček, R., Meurers, B., Seiberl, W., Steinhauser, P., Wessely,

G., ZycH, D., 1993. Erläuterungen zu den Karten über den Untergrund des Wiener Beckens und der angrenzenden Gebiete. – Geol. B.-A.: Wien 22 pp., 1 Abb., 1 Tab., 3 Tafeln.

Lee, E.Y., Wagreich, M., 2016. Polyphase tectonic subsidence evolution of the Vienna Basin inferred from quantitative subsidence analysis of the northern and central parts. Int. J. Earth Sci. 106, 687-705.

Leonard M (2010) Earthquake fault scaling: self-consistent relating of rupture length, width, average displacement, and moment release. Bull Seismol Soc Am 100, 1971–1988.

Loke, M. H. (1999). A Practical Guide to 2D and 3D Surveys. Electrical Imaging Surveys for Environmental and Engineering Studies, 8-10.

Madea, B., & Taylor Francis. (2015). Estimation of the time since death (Third edition). CRC Press, an imprint of Taylor and Francis. 259-266.

McCalpin, J.P., 2009. Paleoseismology. 2nd Edition, Academic Press, Amsterdam-London, 615 p. (International Series, 95).

Michetti,A. M., Audemard M., F. A., Marco, S., 2005. Future trends in paleoseismology; integrated study of the seismic landscape as a vital tool in seismic hazard analyses. Tectonophysics, 408(1-4), 3–21.

Nagel, J., 1768. Ausführliche Nachricht von dem am 27ten Hornung dieses laufenden Jahrs 1768 in und um Wien erlittenen Erdbeben. – 24 S., Wien.

Nasir, A. et al., 2013. Assessing the completeness of historical and instrumental earthquake data in Austria and the surrounding areas. Austrian Journal of Earth Sciences 106.1, pp. 90–102.

Nasir, A., Hintersberger, E., Decker, K., 2020, the 1906 Dobrá Voda Earthquake (M=5.7) at the Vienna Basin Transfer Fault: Evaluation of the ESI2007 intensity and analysis of the aftershock sequence. Austrian Journal of Earth Sciences, vol. 113, no. 1, 43-58.

Olson, C.G. & Nettelton, W.D. 1998. Paleosols and the effects of alteration. Quaternary International, 51/52, 185-194.

Pantosti, D., Yeats, R.S., 1993. Paleoseismology of great earthquakes of the late Holocene. Ann. Geophys. [Internet].

Penck, A. & Brückner, E., 1909. Die Alpen im Eiszeitalter, Leipzig.

Peresson, H., and Decker, K., 1997. Far-field effects of Late Miocene subduction in the Eastern Carpatians: EW compression and inversion of structures in the Alpine-Carpatian-Pannonian region, Tectonics, 16.1, 38-56.

Pigati, J.S. et al., 2013. 'Radiocarbon dating late Quaternary loess deposits using small terrestrial gastropod shells', Quaternary science reviews, 76, pp. 114–128.

Reimer, P. J., Bard, E., Bayliss, A., Beck, J. W., Blackwell, P. G., Ramsey, C. B., Brown, D. M., Buck, C. E., Edwards, R. L., Friedrich, M., Grootes, P. M., Guilderson, T. P., Haflidason, H., Hajdas, I., Hatté, C., Heaton, T. J., Hogg, A. G., Hughen, K. A., Kaiser, K. F., … van der Plicht, J. (2013). Selection and Treatment of Data for Radiocarbon Calibration: An Update to the International Calibration (IntCal) Criteria. Radiocarbon, 55, 1923–1945.

Royden, L.H., 1985. The Vienna Basin: A thin skinned pull apart basin. In: Biddle, K.T. and Christie Blick, N. (eds.), Strike slip deformation, basin formation and sedimentation. SEPM Special Publication 37, 319-338.

Royden, L.H., 1988. Late Cenozoic tectonics of the Pannonian basin system. In: Royden L.H., Horvath F. (eds) The Pannonian basin: a study in basin evolution. AAPG Memoir 45. American Association of Petroleum Geologists and Hungarian Geological Society, Tulsa, 27–48.

Royden, L.H., Horvath, F., Rumpler, J., 1983. Evolution of the Pannonian basin system, 1. Tectonics. Tectonics 2, 63–90.

Salcher, B.C., Meurers, B., Smit, J., Decker, K., Holzel, M., Wagreich, M., 2012. Strike-slip tectonics and Quaternary basin formation along the Vienna Basin fault system inferred from Bouguer gravity derivatives. Tectonics 31, 1-21.

Salcher, B.C., Wagreich, M., 2010. Climate and tectonic controls on Pleistocene sequence development and river evolution in the Southern Vienna Basin (Austria). Quaternary International 222, 154-167.

Schnabel, W., 2002. Legende und kurze Erläuterung zur Geologischen Karte von Niederösterreich 1:200.000.

Sebe, K., Roetzel, R., Fiebig, M., Lüthgens, C., 2015. Pleistocene wind system in eastern Austria and its impact on landscape evolution. Catena 134, 59-74.

Smalley, I.J., 1995. Making the material: the formation of silt-sized primary mineral particles for loess deposits. Quaternary Science Reviews 14, 645–651.

Strauss, P., Harzhauser, M., Hinsch, R. and Wagreich, M., 2006. Sequence stratigraphy in a classic pull apart basin (Neogene, Vienna Basin) - A 3D seismic based integrated approach. Geologica Carpathica.

van Husen, D., Reitner, J.M., 2011a. An Outline of the Quaternary Stratigraphy of Austria. E&G: Quaternary Science Journal 60, 366-387.

Weissl, M., Hintersberger, E., Lomax, J., Luethgens, C., Decker, K., 2017. Active tectonics and geomorphology of the Gaenserndorf Terrace in the central Vienna Basin (Austria). Quaternary International, 451, 209–222.

Wells, D.L., Coppersmith, K.J., 1994. New empirical relationships among magnitude, rupture length, rupture width, rupture area, and surface displacement. Bull Seismol Soc Am 4.84, pp. 975–1002.

Wessely G., 1993. Der Untergrund des Wiener Beckens. In: Brix F, Schulz O (eds) Erdöl und Erdgas in Österreich. Naturhistorisches Museum Wien und F. Berger, Horn, pp 249–280.

Wessely, G., 2006. Wiener Becken. In: Wessely, G. (Ed.), Geologie der österreichischen Bundesländer: Niederösterreich, Vienna: Geologische Bundesanstalt, pp. 189-226.

Wiesbauer, H., Mazzucco, K., Schratt-Ehrendorfer, L., 1997. Dünen in Niederösterreich: Ökologie und Kulturgeschichte eines bemerkenswerten Landschaftselementes, Fachberichte des NÖ Landschaftsfonds 6, St. Pölten: Amt der Niederösterreichischen Landesregierung.

A. Appendix

A.1 Additional Plates, Figures and Tables

Plate 1 trenchlog – photomosaic of GER01 – N and S section

Plate 2 digital trenchlog – GER01 – N and S section

Table. A. 1: Gauß-Krüger coordinates of the trench site GER01 and height in meters above sea-level.

Table. A. 2: Grain size distribution curve of K1.

Table. A. 3: Grain size distribution curve of K2.

Table. A. 4: Grain form, roundness, roughness and petrography of gravels in K1.

Table. A. 5: Grain form, roundness, roughness and petrography of gravels in K2.

Table. A. 6: Grain size distribution of L1 to L6 and S3 and S4.

Table. A. 7: Conventional and calibrated ages of gastropod samples in L1 to L4B and L6, S1, C1 and C1 and calcite crusts.

Table. A. 8: Dip and dip direction of F1 and F2.

Radiocarbon dating results Beta Analytic Testing Laboratory

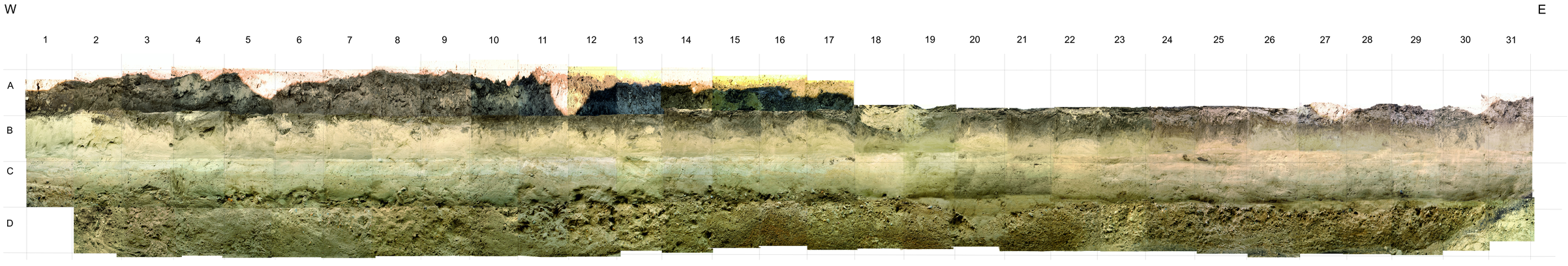

Paleoseismological Trench Seyring Fault Gerasdorf

Orthorectified Photomosaic of N and S section
grid spacing 1m

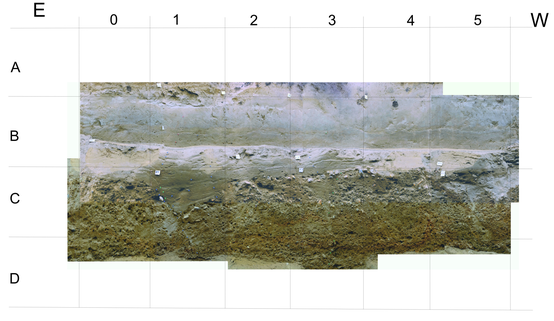

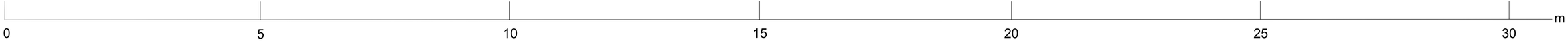

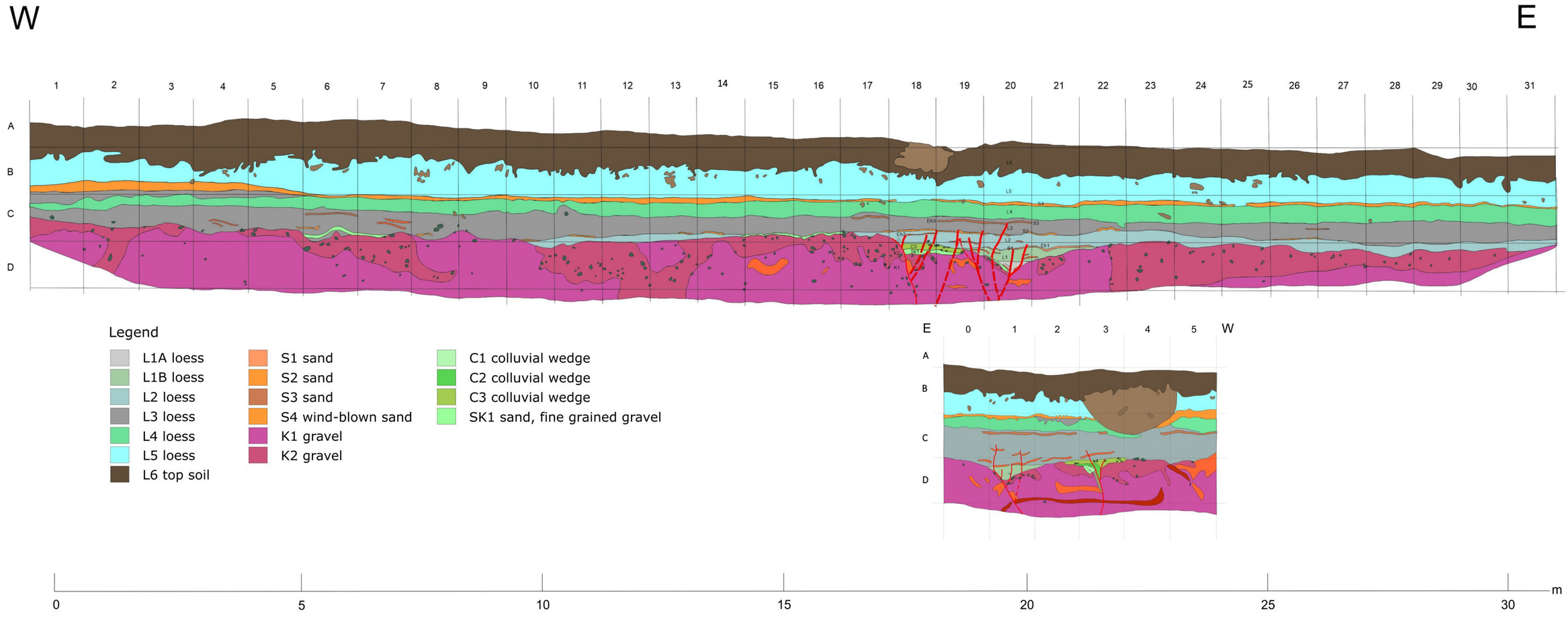
W
E
1 2 3 4 5 6 7 8 9 10 11 12 13 14 15 16 17 18 19 20 21 22 23 24 25 26 27 28 29 30 31
A
B
C
D
L6
L5
L4
L3
L2
L1
S4
S3
S2
S1
Eh3
Eh2
Eh1
C3
SK1
K2
K1
Legend
L1A loess
L1B loess
L2 loess
L3 loess
L4 loess
L5 loess
L6 top soil
S1 sand
S2 sand
S3 sand
S4 wind-blown sand
K1 gravel
K2 gravel
C1 colluvial wedge
C2 colluvial wedge
C3 colluvial wedge
SK1 sand, fine grained gravel
E 0 1 2 3 4 5 W
A
B
C
D
0 5 10 15 20 25 30 m

Trenching location coordinates (Gauß Krüger)					
GER01	**ID**	**X (m)**	**Y (m)**	**Height (mü A)**	**Location**
	OF01	759943.447	352528.466	169.801	NW point
	OF02	759943.121	352526.013	169.782	SW point
	OF03	759904.643	352535.445	170.685	NE point
	OF04	759905.058	352537.735	170.642	SE point

Table. A. 1: Gauß-Krüger coordinates of the trench site GER01 and height in meters above sea-level.

K 1

mm	% of passing
63	100,0
32	97,5
16	87,4
8	72,6
4	62,4
2	58,9
1	56,3
0,5	54,5
0,25	46,5
0,125	28,8
0,063	19,5

grain size (mm)	% retained
> 63	0,0
> 20	8,8
> 6,3	22,8
> 2,0	9,5
> 0,63	3,5
> 0,2	14,4
> 0,063	21,5

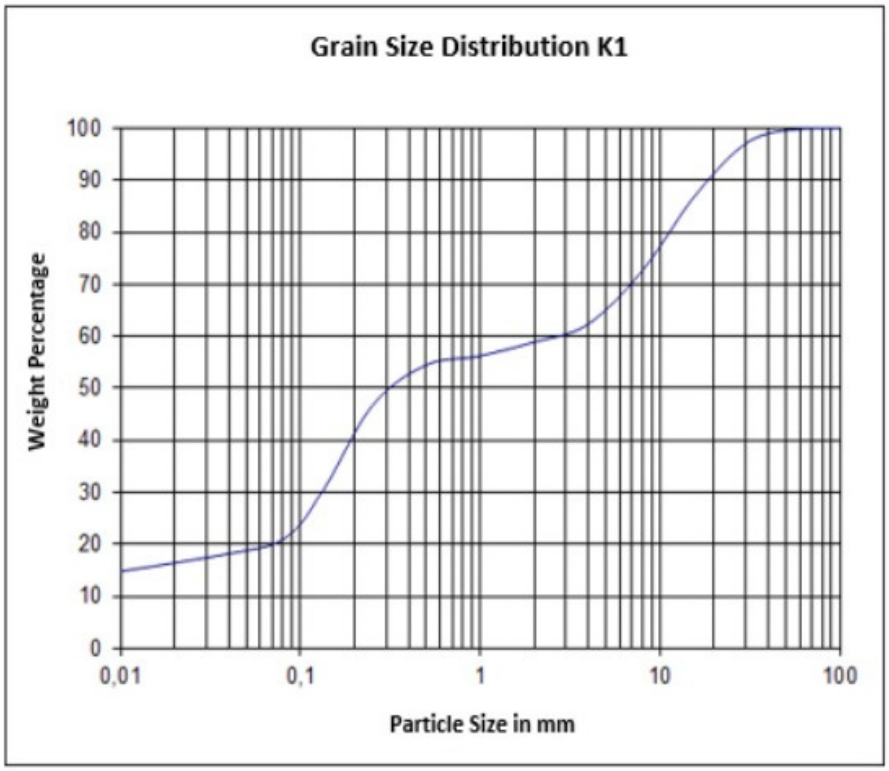

Table. A. 2: Grain size distribution curve of K1.

K 2

mm	% of passing
63	99,6
32	94,6
16	86,0
8	79,9
4	75,3
2	71,3
1	67,6
0,5	65,6
0,25	60,6
0,125	41,9
0,063	24,6

grain size (mm)	% retained
> 63	0,4
> 20	10,8
> 6,3	10,7
> 2,0	6,8
> 0,63	4,8
> 0,2	11,2
> 0,063	30,7

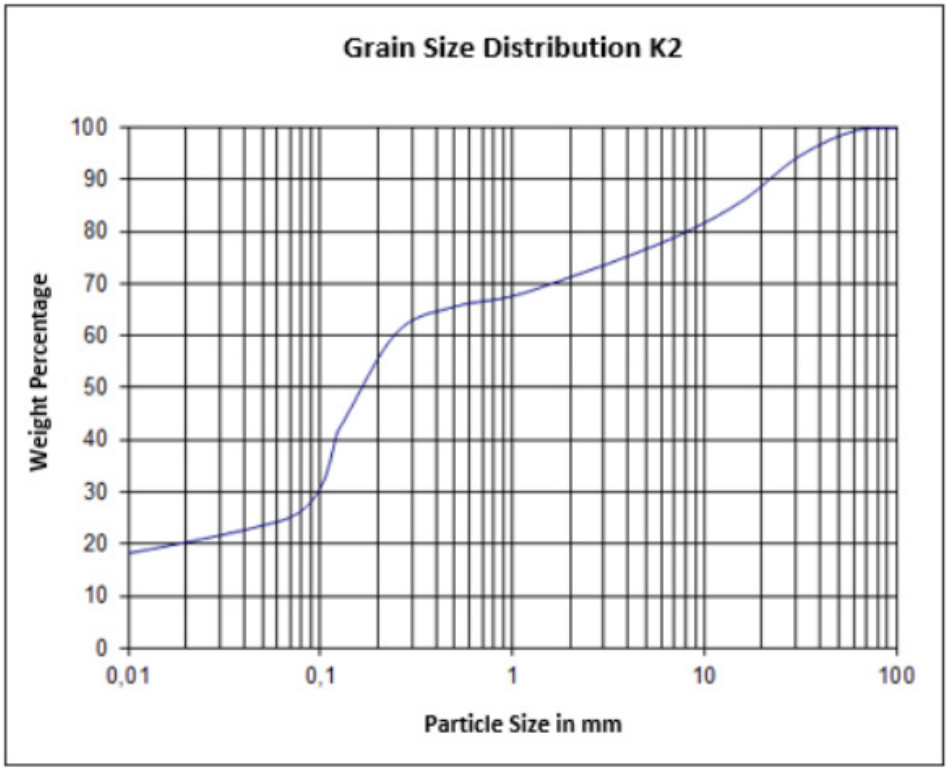

Table. A. 3: Grain size distribution curve of K2.

K 1

grain form		**16/32**
round	dice shaped	36 %
flat	quadratic platty	22 %
	platty	12 %
elongated	stängelig, stäbchenförmig	30 %

roundness	**16/32**
round	3 %
slightly rounded	21 %
angular	61 %
very angular	15 %

roughness	**16/32**
very rough	15 %
rough	40 %
smooth	31 %
very smooth	14 %

petrography	**16/32**
quarz, chert	64 %
carbonate	25 %
metamorphite	11 %

Table. A. 4: Grain form, roundness, roughness and petrography of gravels in K1.

K 2

grain form		grain form
round	round	19 %
flat	flat	42 %
	plattig	43 %
elongated	elongated	14 %

roundness	16/32
round	2 %
slightly rounded	16 %
angular	70 %
very angular	12 %

roughness	16/32
very rough	4 %
rough	44 %
smooth	46 %
very smooth	6 %

petrography	16/32
quarz, chert	80 %
carbonate	13 %
metamorphite	7 %

Table. A. 5: Grain form, roundness, roughness and petrography of gravels in K2.

L1			
>mm	g retained	% retained	% of passing
2	0,9	0,5	99,5
1	0,8	0,4	99,1
0,5	1,1	0,6	98,5
0,25	6,5	3,5	94,9
0,125	31,5	17,2	77,8
0,063	41,2	22,4	55,4
<0,063	101,7	55,4	0,0
Total	183,7	100,0	

L2			
>mm	g retained	% retained	% of passing
2	1,1	0,6	99,4
1	0,9	0,5	98,9
0,5	0,7	0,4	98,5
0,25	5,2	2,9	95,6
0,125	29,8	16,6	79,0
0,063	37,9	21,2	57,8
<0,063	103,6	57,8	0,0
Total	179,2	100,0	

L3			
>mm	g retained	% retained	% of passing
2	2,5	1,4	98,61
1	0,9	0,5	98,1
0,5	0,8	0,4	97,7
0,25	9,2	5,1	92,6
0,125	33,7	18,7	73,9
0,063	32,7	18,1	55,8
<0,063	100,7	55,8	0,0
Total	180,5	100,0	

L4			
>mm	g retained	% retained	% of passing
2	0,8	0,5	99,6
1	0,6	0,3	99,2
0,5	0,9	0,5	98,7
0,25	3,8	2,1	96,6
0,125	13,1	7,3	89,3
0,063	45,0	25,2	64,1
<0,063	114,5	64,1	0,0
Total	178,7	100,0	

L5			
>mm	g retained	% retained	% of passing
2	0,9	0,4	99,6
1	0,8	0,3	99,3
0,5	0,4	0,2	99,2
0,25	4,6	1,9	79,3
0,125	28,2	11,4	85,9
0,063	103,9	42,1	43,8
<0,063	108,1	43,8	0,0
Total	246,9	100,0	

L6			
>mm	g retained	% retained	% of passing
2	1,0	0,8	99,2
1	2,1	1,7	97,4
0,5	0,9	0,8	96,7
0,25	4,3	3,6	93,1
0,125	21,3	17,7	75,5
0,063	52,4	43,5	32,0
<0,063	38,6	32,0	0,0
Total	120,6	100,0	

S3			
>mm	g retained	% retained	% passing
2	0,3	0,2	99,8
1	0,3	0,2	99,7
0,5	0,5	0,3	99,4
0,25	6,1	3,5	95,9
0,125	26,9	15,4	80,5
0,063	44,6	25,5	54,9
<0,063	95,9	54,9	0,0
Total	174,6	100,0	

S4			
>mm	g retained	% retained	% of passing
2	0,2	0,1	99,9
1	0,1	0,1	99,8
0,5	0,4	0,2	99,6
0,25	12,8	7,4	92,2
0,125	58,7	33,8	58,4
0,063	62,0	35,7	22,7
<0,063	39,3	22,7	0,0
Total	173,5	100,0	

Table. A. 6: Grain size distribution of L1 to L6 and S3 and S4.

BETA	SUBMITTER NO	SERVICES	MATERIAL / PRETREATMENT	CONVENTIONAL AGE	CALIBRATED AGE	IRMS d13C	IRMS d18O	RECEIVED	REPORTED
600796	S1CR	AMS-Standard delivery	(carbonate): acid etch	40140 +/- 440 BP	44189 - 42751 cal BP	+1.5 o/oo	-8.17	8.19.2021 12:00:00 AM	09.09.2021 10:46
600795	L5	AMS-Standard delivery	(shell): acid etch	12600 +/- 30 BP	15150 - 14885 cal BP	-5.9 o/oo	-4.00	8.19.2021 12:00:00 AM	09.09.2021 10:46
600794	L4B	AMS-Standard delivery	(shell): acid etch	12680 +/- 30 BP	15240 - 14989 cal BP	-6.8 o/oo	-3.91	8.19.2021 12:00:00 AM	09.09.2021 10:46
600793	L4A	AMS-Standard delivery	(shell): acid etch	13370 +/- 40 BP	16255 - 15933 cal BP	-6.6 o/oo	-3.66	8.19.2021 12:00:00 AM	09.09.2021 10:46
600792	L3B	AMS-Standard delivery	(shell): acid etch	13040 +/- 30 BP	15766 - 15485 cal BP	-4.5 o/oo	-4.66	8.19.2021 12:00:00 AM	09.09.2021 10:46
600791	L3A	AMS-Standard delivery	(shell): acid etch	12970 +/- 30 BP	15655 - 15337 cal BP	-7.1 o/oo	-4.72	8.19.2021 12:00:00 AM	09.09.2021 10:46
600790	L2	AMS-Standard delivery	(shell): acid etch	19120 +/- 50 BP	23132 - 22926 cal BP	-7.1 o/oo	-4.31	8.19.2021 12:00:00 AM	09.09.2021 10:46
600789	L1			20920 +/-70 BP					
600787	SK1/1N	AMS-Standard delivery	(shell): acid etch	26030 +/- 90 BP	30437 - 30025 cal BP	-6.3 o/oo	-4.35	8.19.2021 12:00:00 AM	09.09.2021 10:46
600786	C1C2	AMS-Standard delivery	(shell): acid etch	27790 +/- 110 BP	31961 - 31370 cal BP	-7.4 o/oo	-3.14	8.19.2021 12:00:00 AM	09.09.2021 10:46
600785	SK1/2S	AMS-Standard delivery	(shell): acid etch	26870 +/- 100 BP	31182 - 30946 cal BP	-6.9 o/oo	-4.84	8.19.2021 12:00:00 AM	09.09.2021 10:46
636868	K2	AMS-Standard delivery	(shell): acid etch	26670 +/- 120 BP	31148 - 30733 cal BP	-7.5 o/oo	-4.90	08.19.2022	08.09.2022

Table. A. 7: Conventional and calibrated ages of gastropod samples in L1 to L4B and L6, S1, C1 and C1 and calcite crusts.

Fault	DipDir	Dip
F1	094	76
F1	095	76
F1	094	53
F2	272	57
F2	273	79
F2	275	55
F2	274	76

Table. A. 8: Dip and dip direction of F1 and F2.

Beta Analytic, Inc.
4985 SW 74th Court
Miami, FL 33155 USA
Tel: 305-667-5167
Fax: 305-663-0964
info@betalabservices.com

ISO/IEC 17025:2017-Accredited Testing Laboratory

September 09, 2021

Mr. Kurt Decker
University of Vienna
Institute of Geology
Vienna, 1090
Austria

RE: Radiocarbon Dating Results

Dear Mr. Decker,

Enclosed are the radiocarbon dating results for ten samples recently sent to us. As usual, the method of analysis is listed on the report with the results and calibration data is provided where applicable. The Conventional Radiocarbon Ages have all been corrected for total fractionation effects and where applicable, calibration was performed using 2020 calibration databases (cited on the graph pages).

The web directory containing the table of results and PDF download also contains pictures, a cvs spreadsheet download option and a quality assurance report containing expected vs. measured values for 3-5 working standards analyzed simultaneously with your samples.

Reported results are accredited to ISO/IEC 17025:2017 Testing Accreditation PJLA #59423 standards and all chemistry was performed here in our laboratory and counted in our own accelerators here. Since Beta is not a teaching laboratory, only graduates trained to strict protocols of the ISO/IEC 17025:2017 Testing Accreditation PJLA #59423 program participated in the analyses.

As always Conventional Radiocarbon Ages and sigmas are rounded to the nearest 10 years per the conventions of the 1977 International Radiocarbon Conference. When counting statistics produce sigmas lower than +/- 30 years, a conservative +/- 30 BP is cited for the result unless otherwise requested. The reported d13C values were measured separately in an IRMS (isotope ratio mass spectrometer). They are NOT the AMS d13C which would include fractionation effects from natural, chemistry and AMS induced sources.

When interpreting the results, please consider any communications you may have had with us regarding the samples.

Our invoice will be emailed separately. Please forward it to the appropriate officer or send a credit card authorization. Thank you. As always, if you have any questions or would like to discuss the results, don't hesitate to contact us.

Sincerely,

Chris Patrick
Vice President of Laboratory Operations

Beta Analytic, Inc.
4985 SW 74th Court
Miami, FL 33155 USA
Tel: 305-667-5167
Fax: 305-663-0964
info@betalabservices.com

ISO/IEC 17025:2017-Accredited Testing Laboratory

REPORT OF RADIOCARBON DATING ANALYSES

Kurt Decker

University of Vienna

Report Date: September 09, 2021

Material Received: August 19, 2021

Laboratory Number	Sample Code Number	Conventional Radiocarbon Age (BP) or Percent Modern Carbon (pMC) & Stable Isotopes	
Beta - 600786	**C1C2**	**27790 +/- 110 BP**	IRMS δ13C: -7.4 o/oo IRMS δ18O: -3.1 o/oo
(95.4%)	**30012 - 29421 cal BC**	**(31961 - 31370 cal BP)**	

Submitter Material: Shell (Freshwater/Terrestrial)
Pretreatment: (shell) acid etch
Analyzed Material: Shell
Analysis Service: AMS-Standard delivery
Percent Modern Carbon: 3.14 +/- 0.04 pMC
Fraction Modern Carbon: 0.0314 +/- 0.0004
D14C: -968.55 +/- 0.43 o/oo
Δ14C: -968.82 +/- 0.43 o/oo (1950:2021)
Measured Radiocarbon Age: (without d13C correction): 27500 +/- 110 BP
Calibration: BetaCal4.20: HPD method: INTCAL20

Results are ISO/IEC-17025:2017 accredited. No sub-contracting or student labor was used in the analyses. All work was done at Beta in 4 in-house NEC accelerator mass spectrometers and 4 Thermo IRMSs. The "Conventional Radiocarbon Age" was calculated using the Libby half-life (5568 years), is corrected for total isotopic fraction and was used for calendar calibration where applicable. The Age is rounded to the nearest 10 years and is reported as radiocarbon years before present (BP), "present" = AD 1950. Results greater than the modern reference are reported as percent modern carbon (pMC). The modern reference standard was 95% the 14C signature of NIST SRM-4990C (oxalic acid). Quoted errors are 1 sigma counting statistics. Calculated sigmas less than 30 BP on the Conventional Radiocarbon Age are conservatively rounded up to 30. d13C values are on the material itself (not the AMS d13C). d13C and d15N values are relative to VPDB. References for calendar calibrations are cited at the bottom of calibration graph pages.

Beta Analytic, Inc.
4985 SW 74th Court
Miami, FL 33155 USA
Tel: 305-667-5167
Fax: 305-663-0964
info@betalabservices.com

ISO/IEC 17025:2017-Accredited Testing Laboratory

REPORT OF RADIOCARBON DATING ANALYSES

Kurt Decker

University of Vienna

Report Date: September 09, 2021

Material Received: August 19, 2021

Laboratory Number	Sample Code Number	Conventional Radiocarbon Age (BP) or Percent Modern Carbon (pMC) & Stable Isotopes
Beta - 600787	**S1/1N**	**26030 +/- 90 BP**

IRMS δ13C: -6.3 o/oo

IRMS δ18O: -4.4 o/oo

(94.3%) 28488 - 28076 cal BC (30437 - 30025 cal BP)
(1.1%) 28729 - 28681 cal BC (30678 - 30630 cal BP)

Submitter Material: Shell (Freshwater/Terrestrial)
Pretreatment: (shell) acid etch
Analyzed Material: Shell
Analysis Service: AMS-Standard delivery
Percent Modern Carbon: 3.91 +/- 0.04 pMC
Fraction Modern Carbon: 0.0391 +/- 0.0004
D14C: -960.85 +/- 0.44 o/oo
Δ14C: -961.19 +/- 0.44 o/oo (1950:2021)
Measured Radiocarbon Age: (without d13C correction): 25720 +/- 90 BP
Calibration: BetaCal4.20: HPD method: INTCAL20

Results are ISO/IEC-17025:2017 accredited. No sub-contracting or student labor was used in the analyses. All work was done at Beta in 4 in-house NEC accelerator mass spectrometers and 4 Thermo IRMSs. The "Conventional Radiocarbon Age" was calculated using the Libby half-life (5568 years), is corrected for total isotopic fraction and was used for calendar calibration where applicable. The Age is rounded to the nearest 10 years and is reported as radiocarbon years before present (BP), "present" = AD 1950. Results greater than the modern reference are reported as percent modern carbon (pMC). The modern reference standard was 95% the 14C signature of NIST SRM-4990C (oxalic acid). Quoted errors are 1 sigma counting statistics. Calculated sigmas less than 30 BP on the Conventional Radiocarbon Age are conservatively rounded up to 30. d13C values are on the material itself (not the AMS d13C). d13C and d15N values are relative to VPDB. References for calendar calibrations are cited at the bottom of calibration graph pages.

Beta Analytic, Inc.
4985 SW 74th Court
Miami, FL 33155 USA
Tel: 305-667-5167
Fax: 305-663-0964
info@betalabservices.com

ISO/IEC 17025:2017-Accredited Testing Laboratory

REPORT OF RADIOCARBON DATING ANALYSES

Kurt Decker

University of Vienna

Report Date: September 09, 2021

Material Received: August 19, 2021

Laboratory Number	Sample Code Number	Conventional Radiocarbon Age (BP) or Percent Modern Carbon (pMC) & Stable Isotopes	
Beta - 600788	**S1/2S**	**26870 +/- 100 BP**	IRMS δ13C: -6.9 o/oo IRMS δ18O: -4.8 o/oo
(95.4%)	**29233 - 28997 cal BC**	**(31182 - 30946 cal BP)**	

Submitter Material: Shell (Freshwater/Terrestrial)
Pretreatment: (shell) acid etch
Analyzed Material: Shell
Analysis Service: AMS-Standard delivery
Percent Modern Carbon: 3.53 +/- 0.04 pMC
Fraction Modern Carbon: 0.0353 +/- 0.0004
D14C: -964.74 +/- 0.44 o/oo
Δ14C: -965.04 +/- 0.44 o/oo (1950:2021)
Measured Radiocarbon Age: (without d13C correction): 26570 +/- 100 BP
Calibration: BetaCal4.20: HPD method: INTCAL20

Results are ISO/IEC-17025:2017 accredited. No sub-contracting or student labor was used in the analyses. All work was done at Beta in 4 in-house NEC accelerator mass spectrometers and 4 Thermo IRMSs. The "Conventional Radiocarbon Age" was calculated using the Libby half-life (5568 years), is corrected for total isotopic fraction and was used for calendar calibration where applicable. The Age is rounded to the nearest 10 years and is reported as radiocarbon years before present (BP), "present" = AD 1950. Results greater than the modern reference are reported as percent modern carbon (pMC). The modern reference standard was 95% the 14C signature of NIST SRM-4990C (oxalic acid). Quoted errors are 1 sigma counting statistics. Calculated sigmas less than 30 BP on the Conventional Radiocarbon Age are conservatively rounded up to 30. d13C values are on the material itself (not the AMS d13C). d13C and d15N values are relative to VPDB. References for calendar calibrations are cited at the bottom of calibration graph pages.

Beta Analytic, Inc.
4985 SW 74th Court
Miami, FL 33155 USA
Tel: 305-667-5167
Fax: 305-663-0964
info@betalabservices.com

ISO/IEC 17025:2017-Accredited Testing Laboratory

REPORT OF RADIOCARBON DATING ANALYSES

Kurt Decker

University of Vienna

Report Date: September 09, 2021

Material Received: August 19, 2021

Laboratory Number	Sample Code Number	Conventional Radiocarbon Age (BP) or Percent Modern Carbon (pMC) & Stable Isotopes	
Beta - 600790	**L2**	**19120 +/- 50 BP**	IRMS δ13C: -7.1 o/oo IRMS δ18O: -4.3 o/oo
(95.4%)	**21183 - 20977 cal BC**	**(23132 - 22926 cal BP)**	

Submitter Material: Shell (Freshwater/Terrestrial)
Pretreatment: (shell) acid etch
Analyzed Material: Shell
Analysis Service: AMS-Standard delivery
Percent Modern Carbon: 9.25 +/- 0.06 pMC
Fraction Modern Carbon: 0.0925 +/- 0.0006
D14C: -907.47 +/- 0.58 o/oo
Δ14C: -908.26 +/- 0.58 o/oo (1950:2021)
Measured Radiocarbon Age: (without d13C correction): 18830 +/- 50 BP
Calibration: BetaCal4.20: HPD method: INTCAL20

Results are ISO/IEC-17025:2017 accredited. No sub-contracting or student labor was used in the analyses. All work was done at Beta in 4 in-house NEC accelerator mass spectrometers and 4 Thermo IRMSs. The "Conventional Radiocarbon Age" was calculated using the Libby half-life (5568 years), is corrected for total isotopic fraction and was used for calendar calibration where applicable. The Age is rounded to the nearest 10 years and is reported as radiocarbon years before present (BP), "present" = AD 1950. Results greater than the modern reference are reported as percent modern carbon (pMC). The modern reference standard was 95% the 14C signature of NIST SRM-4990C (oxalic acid). Quoted errors are 1 sigma counting statistics. Calculated sigmas less than 30 BP on the Conventional Radiocarbon Age are conservatively rounded up to 30. d13C values are on the material itself (not the AMS d13C). d13C and d15N values are relative to VPDB. References for calendar calibrations are cited at the bottom of calibration graph pages.

Beta Analytic, Inc.
4985 SW 74th Court
Miami, FL 33155 USA
Tel: 305-667-5167
Fax: 305-663-0964
info@betalabservices.com

ISO/IEC 17025:2017-Accredited Testing Laboratory

REPORT OF RADIOCARBON DATING ANALYSES

Kurt Decker

University of Vienna

Report Date: September 09, 2021

Material Received: August 19, 2021

Laboratory Number	Sample Code Number	Conventional Radiocarbon Age (BP) or Percent Modern Carbon (pMC) & Stable Isotopes	
Beta - 600791	**L3A**	**12970 +/- 30 BP**	IRMS δ13C: -7.1 o/oo IRMS δ18O: -4.7 o/oo

(95.4%) 13706 - 13388 cal BC (15655 - 15337 cal BP)

Submitter Material: Shell (Freshwater/Terrestrial)
Pretreatment: (shell) acid etch
Analyzed Material: Shell
Analysis Service: AMS-Standard delivery
Percent Modern Carbon: 19.90 +/- 0.07 pMC
Fraction Modern Carbon: 0.1990 +/- 0.0007
D14C: -801.03 +/- 0.74 o/oo
Δ14C: -802.73 +/- 0.74 o/oo (1950:2021)
Measured Radiocarbon Age: (without d13C correction): 12680 +/- 30 BP
Calibration: BetaCal4.20: HPD method: INTCAL20

Results are ISO/IEC-17025:2017 accredited. No sub-contracting or student labor was used in the analyses. All work was done at Beta in 4 in-house NEC accelerator mass spectrometers and 4 Thermo IRMSs. The "Conventional Radiocarbon Age" was calculated using the Libby half-life (5568 years), is corrected for total isotopic fraction and was used for calendar calibration where applicable. The Age is rounded to the nearest 10 years and is reported as radiocarbon years before present (BP), "present" = AD 1950. Results greater than the modern reference are reported as percent modern carbon (pMC). The modern reference standard was 95% the 14C signature of NIST SRM-4990C (oxalic acid). Quoted errors are 1 sigma counting statistics. Calculated sigmas less than 30 BP on the Conventional Radiocarbon Age are conservatively rounded up to 30. d13C values are on the material itself (not the AMS d13C). d13C and d15N values are relative to VPDB. References for calendar calibrations are cited at the bottom of calibration graph pages.

Beta Analytic, Inc.
4985 SW 74th Court
Miami, FL 33155 USA
Tel: 305-667-5167
Fax: 305-663-0964
info@betalabservices.com

ISO/IEC 17025:2017-Accredited Testing Laboratory

REPORT OF RADIOCARBON DATING ANALYSES

Kurt Decker

University of Vienna

Report Date: September 09, 2021

Material Received: August 19, 2021

Laboratory Number	Sample Code Number	Conventional Radiocarbon Age (BP) or Percent Modern Carbon (pMC) & Stable Isotopes
Beta - 600792	**L3B**	**13040 +/- 30 BP**

IRMS δ13C: -4.5 o/oo

IRMS δ18O: -4.7 o/oo

(95.4%) 13817 - 13536 cal BC (15766 - 15485 cal BP)

Submitter Material: Shell (Freshwater/Terrestrial)
Pretreatment: (shell) acid etch
Analyzed Material: Shell
Analysis Service: AMS-Standard delivery
Percent Modern Carbon: 19.72 +/- 0.07 pMC
Fraction Modern Carbon: 0.1972 +/- 0.0007
D14C: -802.76 +/- 0.74 o/oo
Δ14C: -804.44 +/- 0.74 o/oo (1950:2021)
Measured Radiocarbon Age: (without d13C correction): 12710 +/- 30 BP
Calibration: BetaCal4.20: HPD method: INTCAL20

Results are ISO/IEC-17025:2017 accredited. No sub-contracting or student labor was used in the analyses. All work was done at Beta in 4 in-house NEC accelerator mass spectrometers and 4 Thermo IRMSs. The "Conventional Radiocarbon Age" was calculated using the Libby half-life (5568 years), is corrected for total isotopic fraction and was used for calendar calibration where applicable. The Age is rounded to the nearest 10 years and is reported as radiocarbon years before present (BP), "present" = AD 1950. Results greater than the modern reference are reported as percent modern carbon (pMC). The modern reference standard was 95% the 14C signature of NIST SRM-4990C (oxalic acid). Quoted errors are 1 sigma counting statistics. Calculated sigmas less than 30 BP on the Conventional Radiocarbon Age are conservatively rounded up to 30. d13C values are on the material itself (not the AMS d13C). d13C and d15N values are relative to VPDB. References for calendar calibrations are cited at the bottom of calibration graph pages.

Beta Analytic, Inc.
4985 SW 74th Court
Miami, FL 33155 USA
Tel: 305-667-5167
Fax: 305-663-0964
info@betalabservices.com

ISO/IEC 17025:2017-Accredited Testing Laboratory

REPORT OF RADIOCARBON DATING ANALYSES

Kurt Decker

University of Vienna

Report Date: September 09, 2021

Material Received: August 19, 2021

Laboratory Number	Sample Code Number	Conventional Radiocarbon Age (BP) or Percent Modern Carbon (pMC) & Stable Isotopes	
Beta - 600793	**L4A**	**13370 +/- 40 BP**	IRMS δ13C: -6.6 o/oo IRMS δ18O: -3.7 o/oo
(95.4%)	**14306 - 13984 cal BC**	**(16255 - 15933 cal BP)**	

Submitter Material: Shell (Freshwater/Terrestrial)
Pretreatment: (shell) acid etch
Analyzed Material: Shell
Analysis Service: AMS-Standard delivery
Percent Modern Carbon: 18.93 +/- 0.09 pMC
Fraction Modern Carbon: 0.1893 +/- 0.0009
D14C: -810.70 +/- 0.94 o/oo
Δ14C: -812.31 +/- 0.94 o/oo (1950:2021)
Measured Radiocarbon Age: (without d13C correction): 13070 +/- 40 BP
Calibration: BetaCal4.20: HPD method: INTCAL20

Results are ISO/IEC-17025:2017 accredited. No sub-contracting or student labor was used in the analyses. All work was done at Beta in 4 in-house NEC accelerator mass spectrometers and 4 Thermo IRMSs. The "Conventional Radiocarbon Age" was calculated using the Libby half-life (5568 years), is corrected for total isotopic fraction and was used for calendar calibration where applicable. The Age is rounded to the nearest 10 years and is reported as radiocarbon years before present (BP), "present" = AD 1950. Results greater than the modern reference are reported as percent modern carbon (pMC). The modern reference standard was 95% the 14C signature of NIST SRM-4990C (oxalic acid). Quoted errors are 1 sigma counting statistics. Calculated sigmas less than 30 BP on the Conventional Radiocarbon Age are conservatively rounded up to 30. d13C values are on the material itself (not the AMS d13C). d13C and d15N values are relative to VPDB. References for calendar calibrations are cited at the bottom of calibration graph pages.

Beta Analytic, Inc.
4985 SW 74th Court
Miami, FL 33155 USA
Tel: 305-667-5167
Fax: 305-663-0964
info@betalabservices.com

ISO/IEC 17025:2017-Accredited Testing Laboratory

REPORT OF RADIOCARBON DATING ANALYSES

Kurt Decker

University of Vienna

Report Date: September 09, 2021

Material Received: August 19, 2021

Laboratory Number	Sample Code Number	Conventional Radiocarbon Age (BP) or Percent Modern Carbon (pMC) & Stable Isotopes
Beta - 600794	**L4B**	**12680 +/- 30 BP**

IRMS δ13C: -6.8 o/oo

IRMS δ18O: -3.9 o/oo

(95.4%) 13291 - 13040 cal BC (15240 - 14989 cal BP)

Submitter Material: Shell (Freshwater/Terrestrial)
Pretreatment: (shell) acid etch
Analyzed Material: Shell
Analysis Service: AMS-Standard delivery
Percent Modern Carbon: 20.63 +/- 0.08 pMC
Fraction Modern Carbon: 0.2063 +/- 0.0008
D14C: -793.72 +/- 0.77 o/oo
Δ14C: -795.48 +/- 0.77 o/oo (1950:2021)
Measured Radiocarbon Age: (without d13C correction): 12380 +/- 30 BP
Calibration: BetaCal4.20: HPD method: INTCAL20

Results are ISO/IEC-17025:2017 accredited. No sub-contracting or student labor was used in the analyses. All work was done at Beta in 4 in-house NEC accelerator mass spectrometers and 4 Thermo IRMSs. The "Conventional Radiocarbon Age" was calculated using the Libby half-life (5568 years), is corrected for total isotopic fraction and was used for calendar calibration where applicable. The Age is rounded to the nearest 10 years and is reported as radiocarbon years before present (BP), "present" = AD 1950. Results greater than the modern reference are reported as percent modern carbon (pMC). The modern reference standard was 95% the 14C signature of NIST SRM-4990C (oxalic acid). Quoted errors are 1 sigma counting statistics. Calculated sigmas less than 30 BP on the Conventional Radiocarbon Age are conservatively rounded up to 30. d13C values are on the material itself (not the AMS d13C). d13C and d15N values are relative to VPDB. References for calendar calibrations are cited at the bottom of calibration graph pages.

Beta Analytic, Inc.
4985 SW 74th Court
Miami, FL 33155 USA
Tel: 305-667-5167
Fax: 305-663-0964
info@betalabservices.com

ISO/IEC 17025:2017-Accredited Testing Laboratory

REPORT OF RADIOCARBON DATING ANALYSES

Kurt Decker

University of Vienna

Report Date: September 09, 2021

Material Received: August 19, 2021

Laboratory Number	Sample Code Number	Conventional Radiocarbon Age (BP) or Percent Modern Carbon (pMC) & Stable Isotopes	
Beta - 600795	**L6**	**12600 +/- 30 BP**	IRMS δ13C: -5.9 o/oo IRMS δ18O: -4.0 o/oo
(95.4%)	**13201 - 12936 cal BC**	**(15150 - 14885 cal BP)**	

Submitter Material: Shell (Freshwater/Terrestrial)
Pretreatment: (shell) acid etch
Analyzed Material: Shell
Analysis Service: AMS-Standard delivery
Percent Modern Carbon: 20.83 +/- 0.08 pMC
Fraction Modern Carbon: 0.2083 +/- 0.0008
D14C: -791.65 +/- 0.78 o/oo
Δ14C: -793.43 +/- 0.78 o/oo (1950:2021)
Measured Radiocarbon Age: (without d13C correction): 12290 +/- 30 BP
Calibration: BetaCal4.20: HPD method: INTCAL20

Results are ISO/IEC-17025:2017 accredited. No sub-contracting or student labor was used in the analyses. All work was done at Beta in 4 in-house NEC accelerator mass spectrometers and 4 Thermo IRMSs. The "Conventional Radiocarbon Age" was calculated using the Libby half-life (5568 years), is corrected for total isotopic fraction and was used for calendar calibration where applicable. The Age is rounded to the nearest 10 years and is reported as radiocarbon years before present (BP), "present" = AD 1950. Results greater than the modern reference are reported as percent modern carbon (pMC). The modern reference standard was 95% the 14C signature of NIST SRM-4990C (oxalic acid). Quoted errors are 1 sigma counting statistics. Calculated sigmas less than 30 BP on the Conventional Radiocarbon Age are conservatively rounded up to 30. d13C values are on the material itself (not the AMS d13C). d13C and d15N values are relative to VPDB. References for calendar calibrations are cited at the bottom of calibration graph pages.

Beta Analytic, Inc.
4985 SW 74th Court
Miami, FL 33155 USA
Tel: 305-667-5167
Fax: 305-663-0964
info@betalabservices.com

ISO/IEC 17025:2017-Accredited Testing Laboratory

REPORT OF RADIOCARBON DATING ANALYSES

Kurt Decker

University of Vienna

Report Date: September 09, 2021

Material Received: August 19, 2021

Laboratory Number	Sample Code Number	Conventional Radiocarbon Age (BP) or Percent Modern Carbon (pMC) & Stable Isotopes
Beta - 600796	**S1CR**	**40140 +/- 440 BP**

IRMS δ13C: +1.5 o/oo

IRMS δ18O: -8.2 o/oo

(95.4%) 42240 - 40802 cal BC (44189 - 42751 cal BP)

Submitter Material: Carbonate (Freshwater)
Pretreatment: (carbonate) acid etch
Analyzed Material: Carbonate
Analysis Service: AMS-Standard delivery
Percent Modern Carbon: 0.68 +/- 0.04 pMC
Fraction Modern Carbon: 0.0068 +/- 0.0004
D14C: -993.24 +/- 0.37 o/oo
Δ14C: -993.30 +/- 0.37 o/oo (1950:2021)
Measured Radiocarbon Age: (without d13C correction): 39710 +/- 440 BP
Calibration: BetaCal4.20: HPD method: INTCAL20

Results are ISO/IEC-17025:2017 accredited. No sub-contracting or student labor was used in the analyses. All work was done at Beta in 4 in-house NEC accelerator mass spectrometers and 4 Thermo IRMSs. The "Conventional Radiocarbon Age" was calculated using the Libby half-life (5568 years), is corrected for total isotopic fraction and was used for calendar calibration where applicable. The Age is rounded to the nearest 10 years and is reported as radiocarbon years before present (BP), "present" = AD 1950. Results greater than the modern reference are reported as percent modern carbon (pMC). The modern reference standard was 95% the 14C signature of NIST SRM-4990C (oxalic acid). Quoted errors are 1 sigma counting statistics. Calculated sigmas less than 30 BP on the Conventional Radiocarbon Age are conservatively rounded up to 30. d13C values are on the material itself (not the AMS d13C). d13C and d15N values are relative to VPDB. References for calendar calibrations are cited at the bottom of calibration graph pages.

Calibration of Radiocarbon Age to Calendar Years

(High Probability Density Range Method (HPD): INTCAL20)

(Variables: d13C = -7.4 o/oo)

Laboratory number **Beta-600786**

Conventional radiocarbon age **27790 ± 110 BP**

95.4% probability

(95.4%) 30012 - 29421 cal BC (31961 - 31370 cal BP)

68.2% probability

(68.2%) 29890 - 29630 cal BC (31839 - 31579 cal BP)

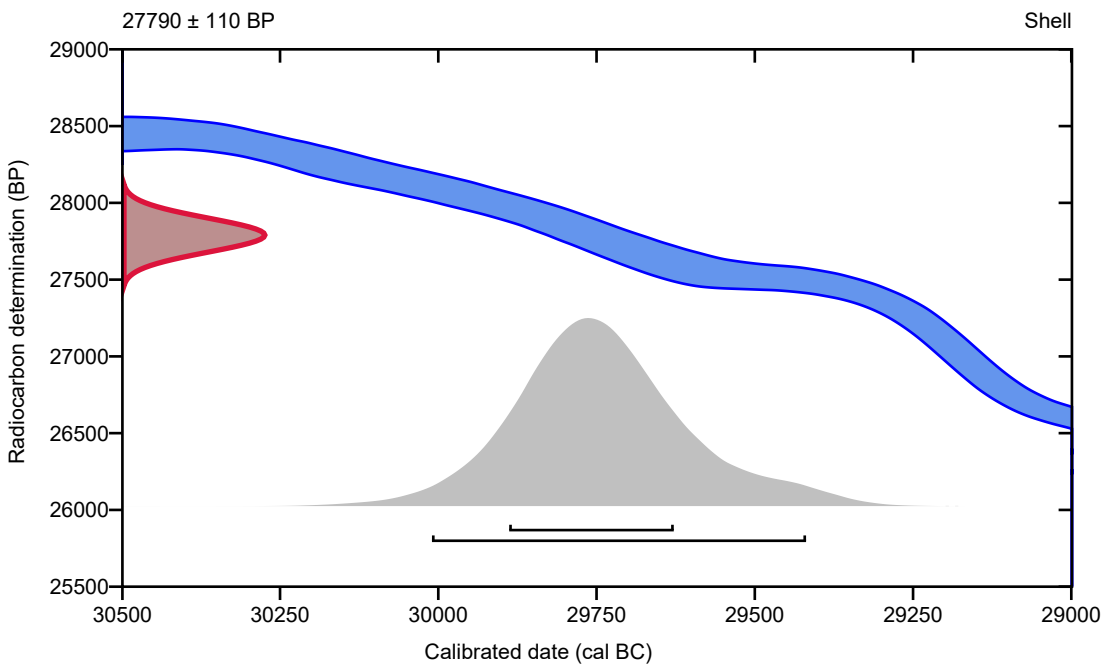

Database used

INTCAL20

References

References to Probability Method

Bronk Ramsey, C. (2009). Bayesian analysis of radiocarbon dates. Radiocarbon, 51(1), 337-360.

References to Database INTCAL20

Reimer, et al., 2020, Radiocarbon 62(4):725-757.

Calibration of Radiocarbon Age to Calendar Years

(High Probability Density Range Method (HPD): INTCAL20)

(Variables: d13C = -6.3 o/oo)

Laboratory number **Beta-600787**

Conventional radiocarbon age **26030 ± 90 BP**

95.4% probability

(94.3%)	28488 - 28076 cal BC	(30437 - 30025 cal BP)
(1.1%)	28729 - 28681 cal BC	(30678 - 30630 cal BP)

68.2% probability

(68.2%)	28361 - 28167 cal BC	(30310 - 30116 cal BP)

S1/1N

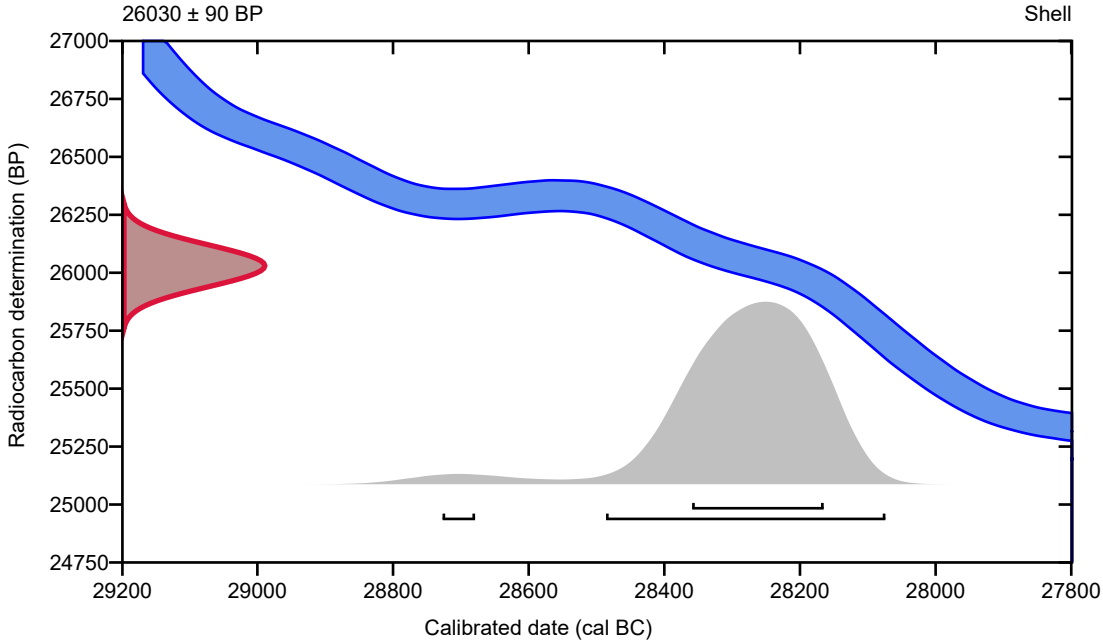

Database used

INTCAL20

References

References to Probability Method

Bronk Ramsey, C. (2009). Bayesian analysis of radiocarbon dates. Radiocarbon, 51(1), 337-360.

References to Database INTCAL20

Reimer, et al., 2020, Radiocarbon 62(4):725-757.

Calibration of Radiocarbon Age to Calendar Years

(High Probability Density Range Method (HPD): INTCAL20)

(Variables: d13C = -6.9 o/oo)

Laboratory number **Beta-600788**

Conventional radiocarbon age **26870 ± 100 BP**

95.4% probability

(95.4%) 29233 - 28997 cal BC (31182 - 30946 cal BP)

68.2% probability

(68.2%) 29185 - 29075 cal BC (31134 - 31024 cal BP)

S1/2S

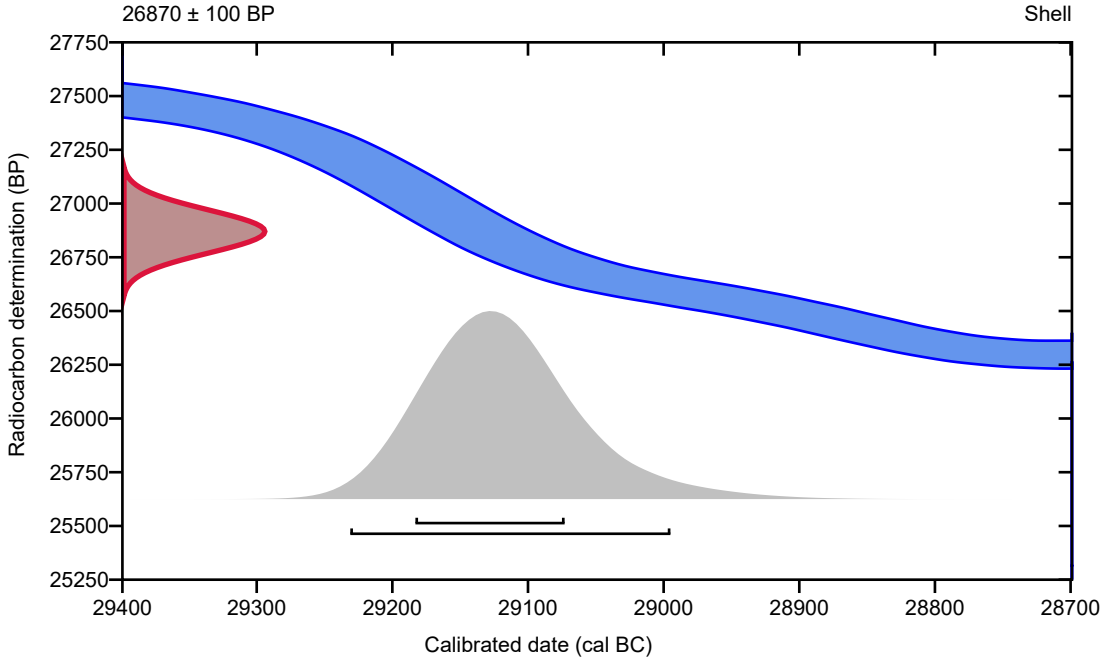

Database used

INTCAL20

References

References to Probability Method

Bronk Ramsey, C. (2009). Bayesian analysis of radiocarbon dates. Radiocarbon, 51(1), 337-360.

References to Database INTCAL20

Reimer, et al., 2020, Radiocarbon 62(4):725-757.

Beta Analytic Radiocarbon Dating Laboratory

4985 S.W. 74th Court, Miami, Florida 33155 • Tel: (305)667-5167 • Fax: (305)663-0964 • Email: beta@radiocarbon.com

Calibration of Radiocarbon Age to Calendar Years

(High Probability Density Range Method (HPD): INTCAL20)

(Variables: d13C = -7.1 o/oo)

Laboratory number **Beta-600790**

Conventional radiocarbon age **19120 ± 50 BP**

95.4% probability

(95.4%) 21183 - 20977 cal BC (23132 - 22926 cal BP)

68.2% probability

(68.2%) 21111 - 21016 cal BC (23060 - 22965 cal BP)

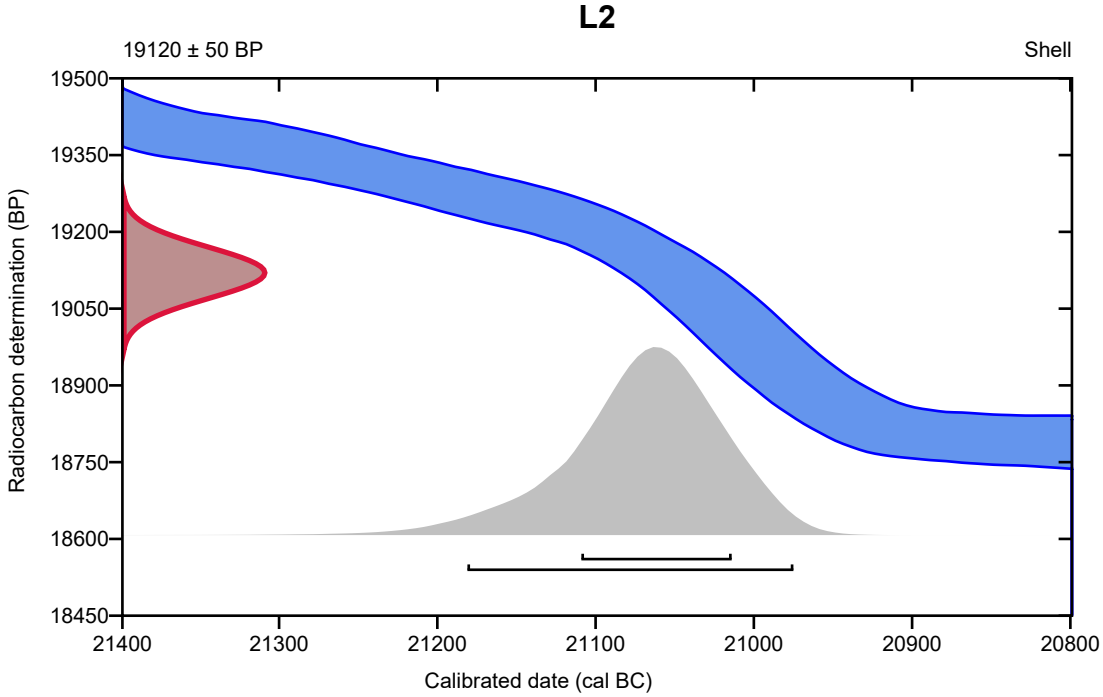

Database used

INTCAL20

References

References to Probability Method

Bronk Ramsey, C. (2009). Bayesian analysis of radiocarbon dates. Radiocarbon, 51(1), 337-360.

References to Database INTCAL20

Reimer, et al., 2020, Radiocarbon 62(4):725-757.

Calibration of Radiocarbon Age to Calendar Years

(High Probability Density Range Method (HPD): INTCAL20)

(Variables: d13C = -7.1 o/oo)

Laboratory number **Beta-600791**

Conventional radiocarbon age **12970 ± 30 BP**

95.4% probability

(95.4%) 13706 - 13388 cal BC (15655 - 15337 cal BP)

68.2% probability

(68.2%) 13666 - 13495 cal BC (15615 - 15444 cal BP)

L3A

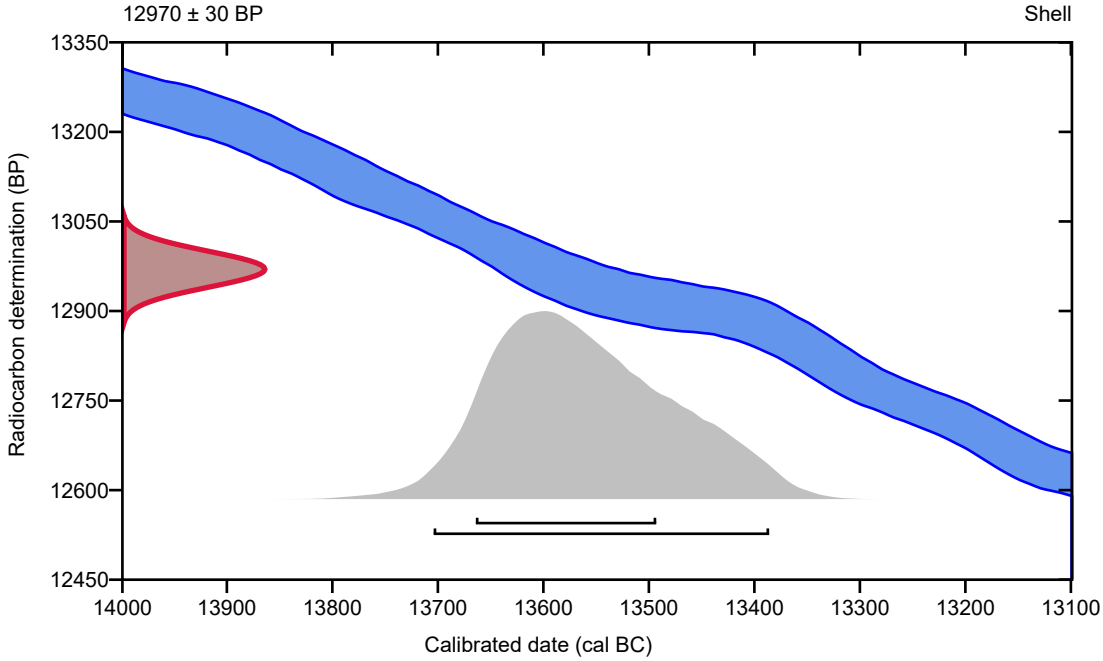

Database used

INTCAL20

References

References to Probability Method

Bronk Ramsey, C. (2009). Bayesian analysis of radiocarbon dates. Radiocarbon, 51(1), 337-360.

References to Database INTCAL20

Reimer, et al., 2020, Radiocarbon 62(4):725-757.

Beta Analytic Radiocarbon Dating Laboratory

4985 S.W. 74th Court, Miami, Florida 33155 • Tel: (305)667-5167 • Fax: (305)663-0964 • Email: beta@radiocarbon.com

Calibration of Radiocarbon Age to Calendar Years

(High Probability Density Range Method (HPD): INTCAL20)

(Variables: d13C = -4.5 o/oo)

Laboratory number **Beta-600792**

Conventional radiocarbon age **13040 ± 30 BP**

95.4% probability

(95.4%) 13817 - 13536 cal BC (15766 - 15485 cal BP)

68.2% probability

(68.2%) 13750 - 13620 cal BC (15699 - 15569 cal BP)

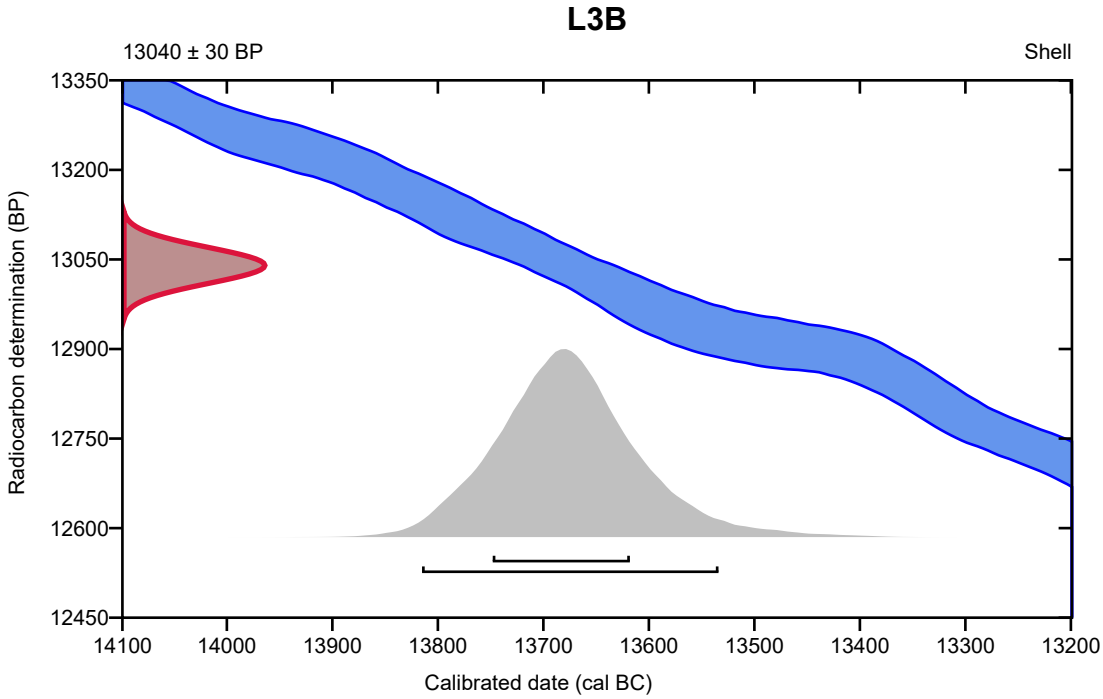

Database used

INTCAL20

References

References to Probability Method

Bronk Ramsey, C. (2009). Bayesian analysis of radiocarbon dates. Radiocarbon, 51(1), 337-360.

References to Database INTCAL20

Reimer, et al., 2020, Radiocarbon 62(4):725-757.

Calibration of Radiocarbon Age to Calendar Years

(High Probability Density Range Method (HPD): INTCAL20)

(Variables: d13C = -6.6 o/oo)

Laboratory number **Beta-600793**

Conventional radiocarbon age **13370 ± 40 BP**

95.4% probability

(95.4%) 14306 - 13984 cal BC (16255 - 15933 cal BP)

68.2% probability

(68.2%) 14225 - 14066 cal BC (16174 - 16015 cal BP)

L4A

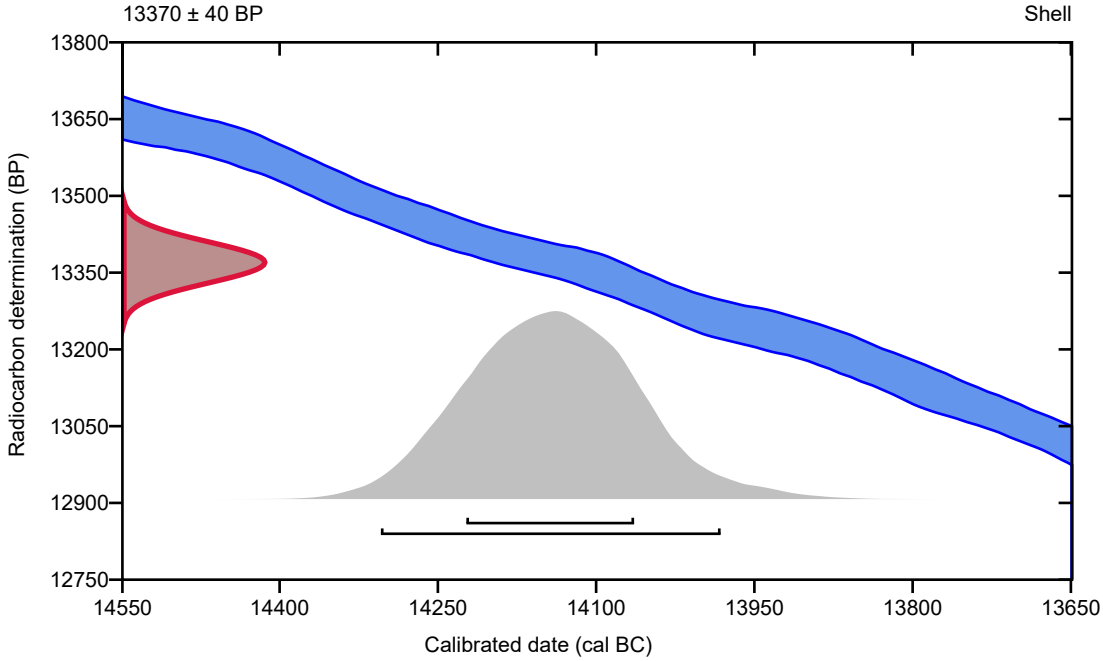

Database used

INTCAL20

References

References to Probability Method

Bronk Ramsey, C. (2009). Bayesian analysis of radiocarbon dates. Radiocarbon, 51(1), 337-360.

References to Database INTCAL20

Reimer, et al., 2020, Radiocarbon 62(4):725-757.

Calibration of Radiocarbon Age to Calendar Years

(High Probability Density Range Method (HPD): INTCAL20)

(Variables: d13C = -6.8 o/oo)

Laboratory number **Beta-600794**

Conventional radiocarbon age **12680 ± 30 BP**

95.4% probability

(95.4%) 13291 - 13040 cal BC (15240 - 14989 cal BP)

68.2% probability

(68.2%) 13235 - 13103 cal BC (15184 - 15052 cal BP)

L4B

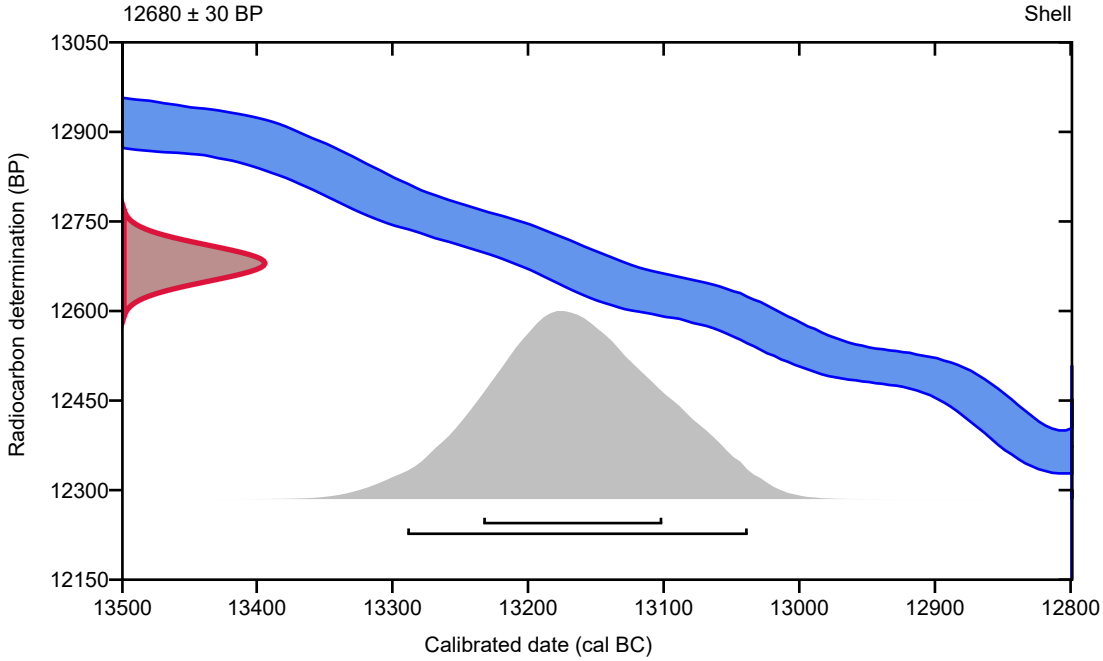

Database used

INTCAL20

References

References to Probability Method

Bronk Ramsey, C. (2009). Bayesian analysis of radiocarbon dates. Radiocarbon, 51(1), 337-360.

References to Database INTCAL20

Reimer, et al., 2020, Radiocarbon 62(4):725-757.

Calibration of Radiocarbon Age to Calendar Years

(High Probability Density Range Method (HPD): INTCAL20)

(Variables: d13C = -5.9 o/oo)

Laboratory number **Beta-600795**

Conventional radiocarbon age **12600 ± 30 BP**

95.4% probability

(95.4%) 13201 - 12936 cal BC (15150 - 14885 cal BP)

68.2% probability

(68.2%) 13137 - 13012 cal BC (15086 - 14961 cal BP)

L6

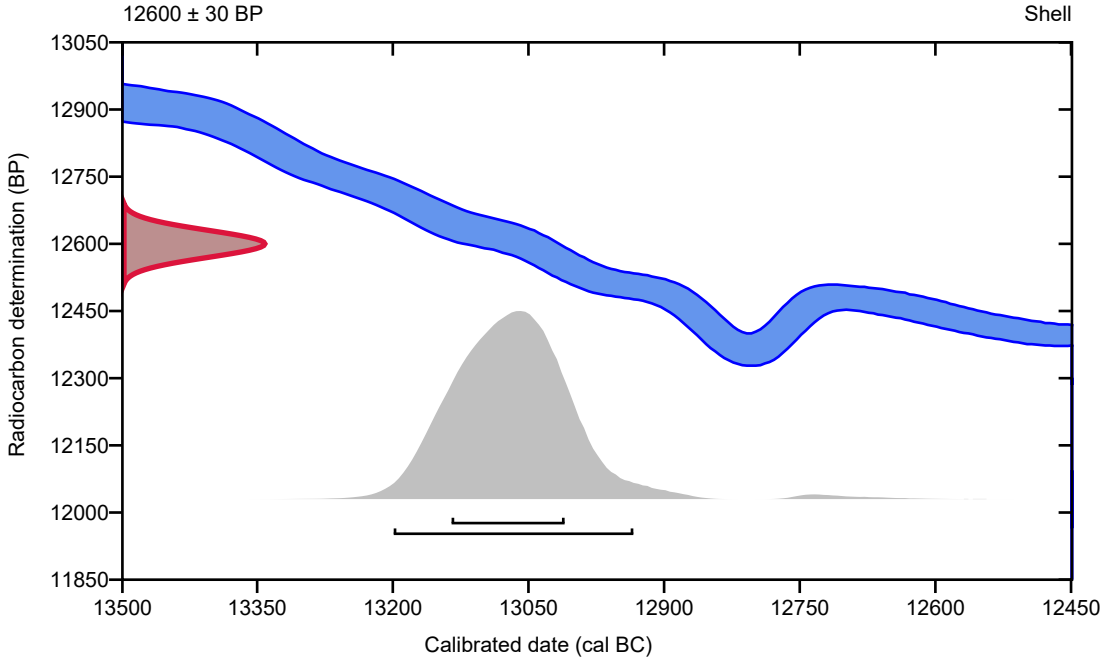

Database used

INTCAL20

References

References to Probability Method

Bronk Ramsey, C. (2009). Bayesian analysis of radiocarbon dates. Radiocarbon, 51(1), 337-360.

References to Database INTCAL20

Reimer, et al., 2020, Radiocarbon 62(4):725-757.

Calibration of Radiocarbon Age to Calendar Years

(High Probability Density Range Method (HPD): INTCAL20)

(Variables: d13C = +1.5 o/oo)

Laboratory number **Beta-600796**

Conventional radiocarbon age **40140 ± 440 BP**

95.4% probability

(95.4%) 42240 - 40802 cal BC (44189 - 42751 cal BP)

68.2% probability

(49.2%) 41521 - 40957 cal BC (43470 - 42906 cal BP)
(19%) 41898 - 41619 cal BC (43847 - 43568 cal BP)

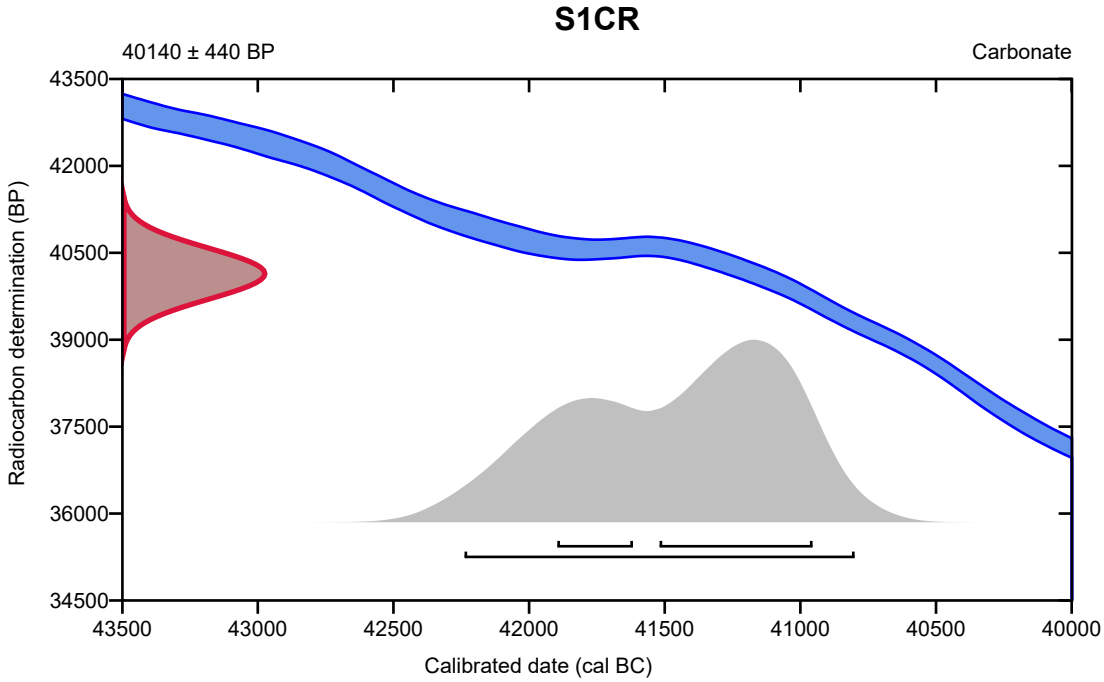

Database used

INTCAL20

References

References to Probability Method

Bronk Ramsey, C. (2009). Bayesian analysis of radiocarbon dates. Radiocarbon, 51(1), 337-360.

References to Database INTCAL20

Reimer, et al., 2020, Radiocarbon 62(4):725-757.

Beta Analytic Radiocarbon Dating Laboratory

4985 S.W. 74th Court, Miami, Florida 33155 • Tel: (305)667-5167 • Fax: (305)663-0964 • Email: beta@radiocarbon.com

Beta Analytic, Inc.
4985 SW 74th Court
Miami, FL 33155 USA
Tel: 305-667-5167
Fax: 305-663-0964
info@betalabservices.com

ISO/IEC 17025:2017-Accredited Testing Laboratory

September 08, 2022

Mr. Kurt Decker
University of Vienna
Institute of Geology
Vienna, 1090
Austria

RE: Radiocarbon Dating Results

Dear Mr. Decker,

Enclosed is the radiocarbon dating result for one sample recently sent to us. As usual, specifics of the analysis are listed on the report with the result and calibration data is provided where applicable. The Conventional Radiocarbon Age has been corrected for total fractionation effects and where applicable, calibration was performed using 2020 calibration databases (cited on the graph pages).

The web directory containing the table of results and PDF download also contains pictures, a cvs spreadsheet download option and a quality assurance report containing expected vs. measured values for 3-5 working standards analyzed simultaneously with your samples.

The reported result is accredited to ISO/IEC 17025:2017 Testing Accreditation PJLA #59423 standards and all pretreatments and chemistry were performed here in our laboratories and counted in our own accelerators here in Miami. Since Beta is not a teaching laboratory, only graduates trained to strict protocols of the ISO/IEC 17025:2017 Testing Accreditation PJLA #59423 program participated in the analysis.

As always Conventional Radiocarbon Ages and sigmas are rounded to the nearest 10 years per the conventions of the 1977 International Radiocarbon Conference. When counting statistics produce sigmas lower than +/- 30 years, a conservative +/- 30 BP is cited for the result unless otherwise requested. The reported d13C was measured separately in an IRMS (isotope ratio mass spectrometer). It is NOT the AMS d13C which would include fractionation effects from natural, chemistry and AMS induced sources.

When interpreting the result, please consider any communications you may have had with us regarding the sample. As always, your inquiries are most welcome. If you have any questions or would like further details of the analysis, please do not hesitate to contact us.

The cost of analysis was previously invoiced. As always, if you have any questions or would like to discuss the results, don't hesitate to contact us.

Sincerely,

Digital signature on file

Chris Patrick
Vice President of Laboratory Operations

Beta Analytic, Inc.
4985 SW 74th Court
Miami, FL 33155 USA
Tel: 305-667-5167
Fax: 305-663-0964
info@betalabservices.com

ISO/IEC 17025:2017-Accredited Testing Laboratory

REPORT OF RADIOCARBON DATING ANALYSES

Kurt Decker

University of Vienna

Report Date: September 08, 2022

Material Received: August 19, 2022

Laboratory Number	Sample Code Number	Conventional Radiocarbon Age (BP) or Percent Modern Carbon (pMC) & Stable Isotopes
Beta - 636868	**K2**	**26670 +/- 120 BP**

IRMS δ13C: -7.5 o/oo

IRMS δ18O: -4.9 o/oo

(94.2%) 29199 - 28784 cal BC (31148 - 30733 cal BP)
(1.2%) 28587 - 28532 cal BC (30536 - 30481 cal BP)

Submitter Material: Carbonate (Freshwater)
Pretreatment: (carbonate) acid etch
Analyzed Material: Carbonate
Analysis Service: AMS-Standard delivery
Percent Modern Carbon: 3.61 +/- 0.05 pMC
Fraction Modern Carbon: 0.0361 +/- 0.0005
D14C: -963.85 +/- 0.54 o/oo
Δ14C: -964.16 +/- 0.54 o/oo (1950:2022)
Measured Radiocarbon Age: (without d13C correction): 26380 +/- 120 BP
Calibration: BetaCal4.20: HPD method: INTCAL20

Results are ISO/IEC-17025:2017 accredited. No sub-contracting or student labor was used in the analyses. All work was done at Beta in 4 in-house NEC accelerator mass spectrometers and 4 Thermo IRMSs. The "Conventional Radiocarbon Age" was calculated using the Libby half-life (5568 years), is corrected for total isotopic fraction and was used for calendar calibration where applicable. The Age is rounded to the nearest 10 years and is reported as radiocarbon years before present (BP), "present" = AD 1950. Results greater than the modern reference are reported as percent modern carbon (pMC). The modern reference standard was 95% the 14C signature of NIST SRM-4990C (oxalic acid). Quoted errors are 1 sigma counting statistics. Calculated sigmas less than 30 BP on the Conventional Radiocarbon Age are conservatively rounded up to 30. d13C values are on the material itself (not the AMS d13C). d13C and d15N values are relative to VPDB. References for calendar calibrations are cited at the bottom of calibration graph pages.

Calibration of Radiocarbon Age to Calendar Years

(High Probability Density Range Method (HPD): INTCAL20)

(Variables: d13C = -7.5 o/oo)

Laboratory number **Beta-636868**

Conventional radiocarbon age **26670 ± 120 BP**

95.4% probability

(94.2%)	29199 - 28784 cal BC	(31148 - 30733 cal BP)
(1.2%)	28587 - 28532 cal BC	(30536 - 30481 cal BP)

68.2% probability

(68.2%)	29118 - 28933 cal BC	(31067 - 30882 cal BP)

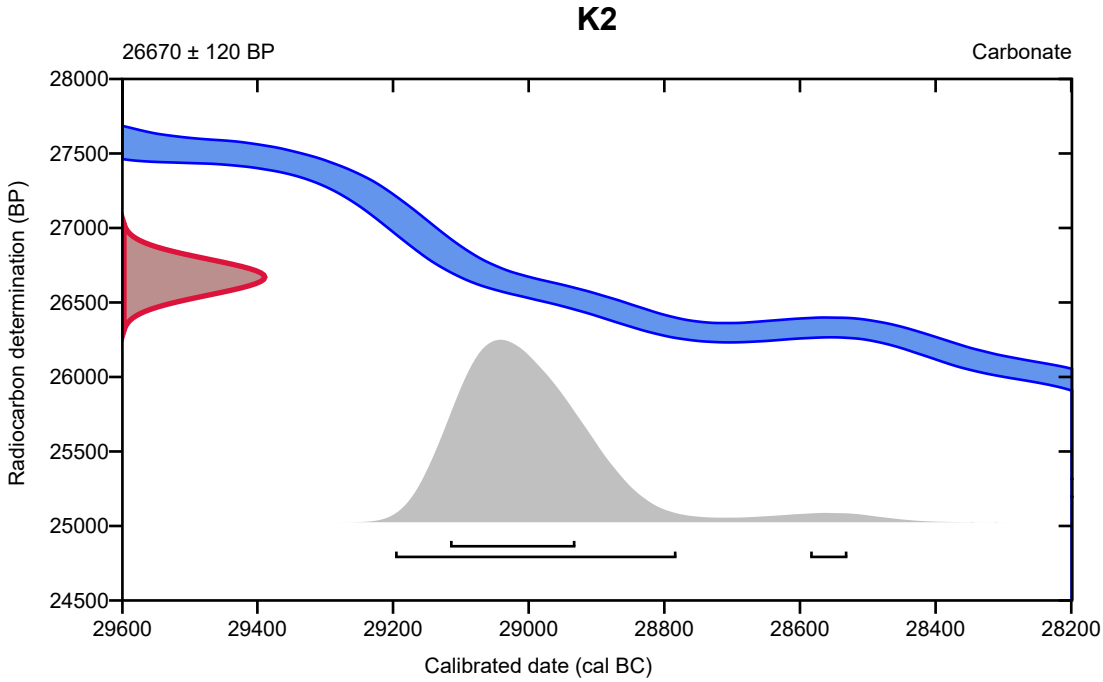

Database used

INTCAL20

References

References to Probability Method

Bronk Ramsey, C. (2009). Bayesian analysis of radiocarbon dates. Radiocarbon, 51(1), 337-360.

References to Database INTCAL20

Reimer, et al., 2020, Radiocarbon 62(4):725-757.

Beta Analytic Radiocarbon Dating Laboratory

4985 S.W. 74th Court, Miami, Florida 33155 • Tel: (305)667-5167 • Fax: (305)663-0964 • Email: beta@radiocarbon.com

Beta Analytic, Inc.
4985 SW 74th Court
Miami, FL 33155 USA
Tel: 305-667-5167
Fax: 305-663-0964
info@betalabservices.com

ISO/IEC 17025:2017-Accredited Testing Laboratory

Quality Assurance Report

This report provides the results of reference materials used to validate radiocarbon analyses prior to reporting. Known-value reference materials were analyzed quasi-simultaneously with the unknowns. Results are reported as expected values vs measured values. Reported values are calculated relative to NISTSRM-1990C and corrected for isotopic fractionation. Results are reported using the direct analytical measure percent modern carbon (pMC) with one relative standard deviation. Agreement between expected and measured values is taken as being within 2 sigma agreement (error x 2) to account for total laboratory error.

Report Date: September 08, 2022
Submitter: Mr. Kurt Decker

QA MEASUREMENTS

Reference 1	
Expected Value:	0.44 +/- 0.04
Measured Value:	0.44 +/- 0.04 pMC
Agreement:	Accepted
Reference 2	
Expected Value:	129.41 +/- 0.06 pMC
Measured Value:	129.74 +/- 0.37 pMC
Agreement:	Accepted
Reference 3	
Expected Value:	96.69 +/- 0.50 pMC
Measured Value:	96.81 +/- 0.30 pMC
Agreement:	Accepted

COMMENT: All measurements passed acceptance tests.

Validation: Chris Patrick
Digital signature on file

Date: September 08, 2022